

**Investigation on the Wheel/Rail Contact and  
Longitudinal Train/Track Interaction Forces**

BY

ALI AFSHARI

B.S., Iran University of Science and Technology, 2004  
M.S., Sharif University of Technology, 2006

THESIS

Submitted as partial fulfilment of the requirements for the degree of  
Doctor of Philosophy in Mechanical Engineering in the  
Graduate College of the  
University of Illinois at Chicago, 2011

Chicago, Illinois

Defense Committee:

Ahmed A. Shabana, Chair and Advisor  
Laxman Saggere  
Thomas J. Royston  
Michael A. Brown  
Behrooz Fallahi, Northern Illinois University

This thesis is dedicated to my parents, without whose support and encouragement it would never have been accomplished.

## **ACKNOWLEDGEMENTS**

I would like to express my gratitude and appreciation to my thesis advisor, Professor Ahmed A. Shabana for his valuable guidance and constructive suggestions during my doctorate studies and research at the Dynamic Simulation Laboratory of the University of Illinois at Chicago. Also, I would like to appreciate my thesis committee members, Dr. Saggere, Dr. Royston, Dr. Brown, and Dr. Fallahi, for their helpful advice regarding this thesis. I would also like to thank Mr. Caldwell, Dr. Zaazaa, and Mr. Marquis for their suggestions that greatly helped me in my research.

Last but not least, I would like to appreciate my parents who were very supportive of me during my studies at the University of Illinois at Chicago.

AA

## TABLE OF CONTENTS

<u>CHAPTER</u>	<u>PAGE</u>
1. INTRODUCTION .....	1
1.1. Motivation .....	1
1.2. Background and Literature Survey .....	4
1.2.1. Choice of the Contact Frame .....	4
1.2.2. Wheel/rail Contact Formulations and Algorithms.....	7
1.2.3. Air Brake Modeling .....	7
1.3. Scope, Objectives and Organization of the Thesis.....	8
2. TANGENTIAL CONTACT FORCE .....	13
2.1. Wheel and Rail Geometry .....	15
2.1.1. Surface Geometry .....	15
2.1.2. Rail Geometry .....	18
2.1.3. Wheel Geometry .....	21
2.2. Rolling Direction (RD) Frame .....	22
2.3. Contact Ellipse (CE) Frame .....	24
2.4. Longitudinal Tangent (LT) Frame .....	29
2.5. Multibody Contact Formulations .....	30
2.6. Numerical Results .....	31
2.6.1. Track with Lateral Deviation.....	32
2.6.2. Track with Variable Profile .....	40
2.6.3. Extreme Case .....	43
2.7. Concluding Remarks .....	44
3. MULTIPOINT CONTACT SEARCH ALGORITHM .....	47
3.1. Contact Formulations .....	47
3.2. Search Algorithm .....	50
3.3. Numerical Results .....	53
3.3.1. Single Truck Model Subjected to Lateral Forces .....	53
3.3.2. Suspended Wheelset Model on a Curve Track.....	60
3.4. Concluding Remarks .....	64
4. AIR BRAKE FORCE MODEL .....	66
4.1. Air Flow Equations .....	68
4.1.1. Continuity Equation.....	68
4.1.2. Momentum Equation .....	69

## TABLE OF CONTENTS (Continued)

4.1.3.	Fluid Constitutive Equation.....	70
4.1.4.	Navier-Stokes Equations.....	71
4.2.	One-dimensional Model.....	71
4.3.	Finite Element Formulation .....	73
4.3.1.	Alternate Formulation.....	75
4.3.2.	Wall Friction Forces .....	76
4.4.	Train Nonlinear Dynamic Equations.....	77
4.4.1.	Position, Velocity, and Acceleration .....	77
4.4.2.	Trajectory Coordinates .....	79
4.4.3.	Equations of Motion .....	81
4.5.	Locomotive Valve Model.....	82
4.6.	Regulating Valve Operation.....	85
4.6.1.	Brake Application and Release.....	88
4.6.2.	Pressure Rate.....	89
4.6.3.	Equilibrium of the Regulating Valve Diaphragm.....	90
4.7.	Relay Valve Operation.....	92
4.7.1.	Brake Release and Application.....	95
4.7.2.	Mathematical Model.....	96
4.7.3.	Simplified Model .....	98
4.8.	Brake Pipe Cut-off Valve Operation.....	100
4.9.	Integration of Locomotive Valve, Brake Pipe and Train Dynamic Models .....	103
4.9.1.	Brake Release .....	103
4.9.2.	Brake Application.....	106
4.10.	Concluding Remarks .....	109
5.	AIR BRAKE COMPUTER IMPLEMENTATION .....	111
5.1.	Car Control Unit (CCU).....	114
5.1.1.	Control Valve.....	115
5.1.2.	Auxiliary and Emergency Reservoirs.....	116
5.1.3.	Brake Cylinder.....	116
5.1.4.	Brake Rigging.....	117
5.1.5.	Brake Shoe.....	117
5.2.	CCU Operation.....	117
5.2.1.	Brake Application Position.....	118
5.2.2.	Release Position.....	119
5.2.3.	Lap Position .....	120

## TABLE OF CONTENTS (Continued)

5.3. CCU Mathematical Model .....	121
5.3.1. Mass Flow Rates .....	122
5.3.2. Pressure Rates .....	125
5.3.3. The Car Brake Parameters in Different Brake Modes .....	126
5.3.4. Brake Force .....	128
5.4. Integration of the Air Brake and Train Dynamics.....	131
5.4.1. Brake Release .....	134
5.4.2. Brake Application .....	136
5.5. Numerical Results .....	138
5.5.1. Brake Application in a 4-Car Model.....	141
5.5.2. Brake Application and Recharge in a 75-Car Model.....	145
5.5.3. Service and Emergency Brake in a 100-Car Model .....	148
5.6. Validation .....	152
5.6.1. Comparison with Experimental Results .....	152
5.6.2. Analytical Validation of Airbrake Dry Charge.....	156
5.7. Concluding Remarks .....	158
6. SUMMARY AND CONCLUSIONS .....	160
REFERENCES .....	163
APPENDIX.....	167
VITA.....	176

## LIST OF TABLES

<u>TABLE</u>	<u>PAGE</u>
I. The average deviation of the RD and LT models from the CE model	40
II. The average deviation of the RD and LT models from the CE model	44
III. The variation range of the parameters associated with car <i>i</i>	127
IV. Friction coefficient for different flow regimes	140
V. Brake pipe and automatic brake valve properties	140
VI. Car control unit properties	141

## LIST OF FIGURES

<u>FIGURE</u>	<u>PAGE</u>
1. The RD, CE, and LT contact frames.....	14
2 . Surface Geometry .....	16
3. The coordinate systems used to define track geometry .....	19
4. The surface parameters at the contact point of the right rail.....	19
5. Space curve and the horizontal plane.....	20
6. The wheel surface parameters.....	22
7. Lateral displacement of the wheelset.....	33
8. Angle of attack at the right wheel .....	33
9. Normal force at the right wheel .....	34
10. Longitudinal force at the right wheel.....	35
11. Lateral force at the right wheel .....	35
12. The angle between the RD and the CE frames .....	36
13. The angle between the LT and the CE frames .....	36
14. X component of the right contact force in the global coordinate system .....	37
15. Y component of the right contact force in the global coordinate system .....	37
16. Z component of the right contact force in the global coordinate system.....	38
17. Longitudinal creepage at the right wheel.....	38
18. Lateral creepage at the right wheel .....	39
19. Right rail profiles .....	41
20. Lateral force at the right wheel .....	42
21. The angle between the RD and the CE frames .....	43
22. The angle between the LT and the CE frames .....	43
23. Single truck model subjected to two lateral forces .....	54
24. The wheel profile .....	55
25. The rail profile .....	55
26. The approximate locations of contact points .....	56
27. Y-coordinate of the left front contact.....	57

## LIST OF FIGURES (Continued)

28. Y-coordinate of the left rear contact .....	57
29. Rail profile surface parameters of the left front contact .....	58
30. Rail profile surface parameters of the left rear contact .....	58
31. Normal force of the left front contact .....	59
32. Normal force of the left rear contact .....	59
33. Suspended wheelset model .....	60
34. The top view of the track used for the suspended wheelset model .....	61
35. The wheel profile .....	61
36. The rail profile .....	62
37. Rail profile surface parameters of the right contact .....	63
38. Normal force of the right contact .....	63
39. Normal force of the right contact (constraint contact method) .....	64
40. Main air brake components .....	66
41. Coordinate systems .....	78
42. Trajectory coordinates .....	80
43. 26C valve scheme .....	83
44. 26C regulating valve .....	87
45. Relay valve .....	93
46. Brake pipe cut-off valve .....	101
47. Car control unit components .....	115
48. The slide valve in the brake application position .....	118
49. The slide valve in the brake release position .....	120
50. The slide valve in the lap position .....	121
51. The parameters associated with the control unit of car $i$ .....	122
52. The mass flow rate between components $e$ and $f$ .....	123
53. The mass flow rate between the brake pipe, atmosphere, and CCU components .....	124
54. The brake force applied on a car wheel .....	130
55. Trajectory coordinates .....	131

## LIST OF FIGURES (Continued)

56. The relationship between the different models developed in this research .....	133
57. Train mass center acceleration.....	142
58. Velocity of car 1.....	142
59. The brake force of car 1 .....	143
60. Pressure difference between the two sides of the relay valve diaphragm.....	144
61. Pressure (gage) inside the equalizing reservoir and the brake pipe .....	144
62. Auxiliary reservoir and brake cylinder pressures (gage) of car 4.....	145
63. Pressure (gage) inside the equalizing reservoir and the brake pipe .....	146
64. Auxiliary reservoir and brake cylinder pressures (gage) of cars 1 and 75.....	146
65. The brake force of car 75 .....	147
66. Train mass center acceleration.....	147
67. Train mass center velocity .....	148
68. Train mass center acceleration.....	149
69. Pressure (gage) inside the equalizing reservoir and the brake pipe .....	150
70. Auxiliary reservoir and brake cylinder pressures (gage) of cars 1 and 100.....	151
71. Distance travelled by car 1.....	151
72. Equalizing reservoir pressure (gage) comparison.....	153
73. Head-end pressure (gage) comparison.....	153
74. Rear-end pressure (gage) comparison.....	154
75. Equalizing reservoir pressure (gage) comparison.....	155
76. Head-end pressure (gage) comparison.....	155
77. Rear-end pressure (gage) comparison.....	156
78. Pressure (gage) at the brake pipe ends during dry charge.....	157
79. Mass transfer rate during dry charge.....	157
80. Valve states and configurations, Appendix.....	170
81. Supply state regions, Appendix .....	172

## LIST OF ABBREVIATIONS

CE	Contact Ellipse
CCU	Car Control Unit
LT	Longitudinal Tangent
RD	Rolling Direction

## SUMMARY

Previous analytical and experimental investigations have shown that the wheel/rail contact forces have a significant effect on the nonlinear dynamics, ride comfort, and stability of railroad vehicle systems. The wheel/rail contact force can be partitioned into two main components; the normal and tangential components. While the direction of the normal contact force is well defined, different directions for the tangential contact forces have been proposed in the literature. In some of the wheel/rail creep theories used in railroad vehicle simulations, the direction of the tangential creep forces is assumed to be the wheel rolling direction (RD). When Hertz theory is used, an assumption is made that the rolling direction is the direction of one of the axes of the contact ellipse. In principle, the rolling direction depends on the wheel motion, while the direction of the axes of the contact ellipse (CE) is determined using the principal directions which depend only on the geometry of the wheel and rail surfaces and do not depend on the motion of the wheel. The RD and CE directions can also be different from the direction of the rail longitudinal tangent (LT) at the contact point. In this investigation, the differences between the contact frames that are based on the RD, LT, and CE directions, that enter into the calculation of the wheel/rail creep forces and moments, are discussed. The choice of the frame, in which the contact forces are defined, can be determined using one longitudinal vector and the normal to the rail at the contact point. While the normal vector is uniquely defined, different choices can be made for the longitudinal vector including the RD, LT, and CE directions. In the case of pure rolling or when the slipping is small, the RD direction can be defined using the cross product of the angular velocity vector and the vector that defines the location of the contact point. Therefore, this direction does not depend explicitly on the geometry of the wheel and rail

## SUMMARY (Continued)

surfaces at the contact point. The LT direction is defined as the direction of the longitudinal tangent obtained by differentiation of the rail surface equation with respect to the rail longitudinal parameter (arc length). Such a tangent does not depend explicitly on the direction of the wheel angular velocity nor does it depend on the wheel geometry. The CE direction is defined using the direction of the axes of the contact ellipse used in Hertz theory. In the Hertzian contact theory, the contact ellipse axes are determined using the principal directions associated with the principal curvatures. Therefore, the CE direction differs from the RD and LT directions in the sense that it is function of the geometry of the wheel and rail surfaces. In order to better understand the role of geometry in the formulation of the creep forces, the relationship between the principal curvatures of the rail surface and the curvatures of the rail profile and the rail space curve is discussed in this investigation. Numerical examples are presented in order to examine the differences in the results obtained using the RD, LT and CE contact frames.

The effect of the tangential forces becomes more significant in the case of multiple contact points between the wheel and the rail. It is important to predict accurately these forces in order to evaluate their effect on the dynamic behavior of the railroad vehicle systems. These contact forces can be determined using parameters such as the wheel/rail geometry, dimensions, material properties, contact area, and relative velocities, etc. However, in order to correctly determine these contact forces, including the normal forces, it is important to determine first all possible wheel/rail contact points. Nonetheless, most existing wheel/rail contact formulations can be used to predict only one or two points of contact between the wheel and rail. There are, however, important scenarios in which there are more than two wheel/rail contact points. The

## SUMMARY (Continued)

lack of accurate three-dimensional multiple point wheel/rail contact formulation represents a serious limitation when derailments and accidents are investigated. In this thesis, a new multipoint contact search algorithm that can be applied to general three-dimensional wheel/rail contact problems is developed. The algorithm is capable of finding any number of wheel/rail contact points. Furthermore, the algorithm can be used with both constraint and elastic contact approaches. The results obtained using the constraint and elastic contact approaches will be compared in the case of multipoint wheel/rail contact. The main steps used in the proposed search algorithm to find all possible contact points are summarized.

Longitudinal train forces resulting from coupler and braking forces are other types of forces that must be considered in derailment and accident investigations. These forces also have a significant effect on the wheel/rail contact forces. Nonetheless, the integration of an accurate air brake model with a nonlinear train dynamic model remains a challenging problem. One of the goals of this investigation is to integrate an air brake model with efficient train longitudinal force algorithms based on the trajectory coordinate formulations. The air brake model, developed in this investigation consists of the locomotive automatic brake valve, air brake pipe, and car control unit (CCU). The proposed air brake force model accounts for the effect of the air flow in long train pipes as well as the effect of leakage and branch pipe flows. This model can be used to study the dynamic behavior of the air flow in the train pipe and its effect on the longitudinal train forces during brake application and release. The governing equations of the air pressure flow are developed using the general fluid continuity and momentum equations, simplified using the assumptions of one dimensional isothermal flow. Using these assumptions, one obtains two

## SUMMARY (Continued)

coupled air velocity/pressure partial differential equations that depend on time and the longitudinal coordinate of the brake pipes. The partial differential equations are converted to a set of first order ordinary differential equations using the finite element method. The resulting air brake ordinary differential equations are solved simultaneously with the train second order nonlinear dynamic differential equations of motion that are based on the trajectory coordinates. The train car nonlinear dynamics is defined using a body track coordinate system that follows the car motion. The body track coordinate system translation and orientation are defined in terms of one parameter that describes the distance traveled by the car. The configuration of the car with respect to its track coordinate system is described using two translation coordinates and three Euler angles. The operation modes of the brake system considered in this investigation are the brake release mode and the brake application mode that includes service and emergency brakes. A detailed model of the locomotive automatic brake valve is presented in this investigation and used to define the inputs to the air brake pipe during the simulation. A simplified model of this valve is also proposed in order to reduce the computational time of the simulation. Then, the detailed CCU formulation is presented. Furthermore, the relationship between the main components of the air brake system and the train dynamics is discussed, and the final set of differential equations that includes the two models is presented. Different computer simulation scenarios are considered in order to investigate the effect of the air brake forces on the train longitudinal dynamics in the case of different braking modes. The numerical results, obtained in this study, are compared with experimental results published in the literature.

# 1. INTRODUCTION

This chapter discusses the motivation for the research presented in this thesis, presents a literature survey for the topics addressed in this investigation, and summarizes the thesis objectives.

## 1.1. Motivation

Railroad vehicle systems are among the most commonly used methods of transportation, both for passengers and goods. Their widespread use has sparked, over the years, continuous technological developments, with the objective of achieving higher operating speeds in order to minimize cost and transportation time. Higher operating speeds, however, require a better and more sophisticated approach for the design of the rail vehicle system in order to avoid derailments and reduce the vibration and noise levels. Therefore, the development and use of accurate computer models for simulation of railroad vehicle systems subjected to different loading conditions, operating speeds, track geometries, braking and traction scenarios are necessary. By using these accurate computer models, it is possible to build virtual prototypes for the simulation and nonlinear dynamic analysis of long trains or for the simulation of detailed single or multiple car models (American Association of Railroads, 2002a and b; American Association of Railroads, 1992; Andrews, 1986; Berzeri et al., 2000; Garg, and Dukkipati, 1984; Railway Technical Web Pages, 2010; Sanborn et al., 2007; Sanborn et al., 2007a and b; Shabana, 2008). Such studies will contribute significantly to better understanding of the causes of derailments and accidents, and to better understanding of the vibration, stability, dynamic characteristics, and longitudinal shock loads of railroad vehicle systems.

Previous analytical and experimental investigations have shown that the wheel/rail contact forces have a significant effect on the nonlinear dynamics, ride comfort, and stability of railroad vehicle systems. Investigations of railroad vehicle accidents have revealed that many of these accidents are due to derailments caused by significantly high forces at the wheel/rail contact points. Using experimental and analytical tools, these contact forces can be measured or evaluated numerically in order to develop guidelines that can be used to avoid derailments. For this reason, the wheel/rail contact analysis has been extensively investigated in the area of railroad vehicle dynamics.

The wheel/rail contact force can be partitioned into two main components; the normal and tangential components. The normal force component is in the direction of the normal to the contact surface, while the tangential component lies in the tangent plane to the rail at the contact point. The tangential force component, which is due to the wheel/rail creep phenomenon, has a significant effect on the dynamics and stability of railroad vehicle systems. In the case of saturation, where the relative velocity of the wheel with respect to the rail is predominantly sliding as in the case of braking scenarios, Coulomb friction law can be used. If the wheel/rail relative motion is dominated by rolling, the creep effect must be taken into consideration. For this reason, the wheel/rail creep forces must be used in the formulation of the nonlinear dynamic equations of railroad vehicle systems. In most of the computer algorithms used in the analysis of the wheel/rail interaction, the normal force is first calculated, and is then used with geometric and material properties of the wheel and rail surfaces to determine the tangential creep forces that enter into the formulation of the nonlinear dynamic equations of the railroad vehicle system.

While the direction of the normal contact force is well defined, different directions for the tangential contact forces have been proposed in the literature. That is, several choices can be made for the direction of the tangential contact forces depending on the formulation used. Although these forces can have a significant effect on the vehicle dynamics, the choice of the direction of these forces has not been investigated in the literature. It is, therefore, one of the main objectives of this thesis to shed light on this important and fundamental issue by examining the effect of the direction of the tangential forces on the wheel/rail dynamic interaction.

The effect of the tangential forces becomes more significant in the case of multiple contact points between the wheel and the rail. It is important to predict accurately these forces in order to evaluate their effect on the dynamic behavior of the railroad vehicle systems. These contact forces can be determined using parameters such as the wheel/rail geometry, dimensions, material properties, contact area, and relative velocities, etc. However, in order to correctly determine these contact forces, including the normal forces, it is important to determine first all possible wheel/rail contact points. Nonetheless, most existing wheel/rail contact formulations can be used to predict only one or two points of contact between the wheel and rail. There are, however, important scenarios in which there are more than two wheel/rail contact points. One important example of these scenarios is when the rail vehicles negotiate switches and turn outs. The lack of accurate three-dimensional multiple point wheel/rail contact formulation represents a serious limitation when derailments and accidents are investigated. It is, therefore, the second objective of this thesis to develop a new procedure that allows for predicting multiple points of contact between the wheel and rail.

Longitudinal train forces resulting from coupler and braking forces are other types of forces that must be considered in derailment and accident investigations. These forces also have a significant effect on the wheel/rail contact forces. Braking forces, for example, lead to significant tangential friction forces at the wheel/contact points. Nonetheless, the integration of an accurate air brake model with a nonlinear train dynamic model remains a challenging problem. It is, therefore, the third objective of this thesis to address this fundamental problem by developing a new procedure that leads to a successful integration of pneumatic air brake model with a fully nonlinear dynamic train model.

## **1.2. Background and Literature Survey**

In this section, a literature survey of the topics considered in this investigation is provided.

### **1.2.1. Choice of the Contact Frame**

The wheel/rail contact forces are defined along the axes of a coordinate system called the *contact frame* whose origin is located at the contact point. One of the axes is in the direction of the normal to the contact surface at the contact point, while the other two axes lie in the tangent plane. There are several choices for the axes that lie in the tangent plane.

In many of the wheel/rail creep force theories as the ones developed by Kalker (1990), the wheel *rolling direction* (RD) is used with the normal to define the contact frame. Many authors assume that the rolling direction is the same as the direction of one of the axes of the contact ellipse when Hertz contact theory is used (Gugliotta and Soma, 1996; Malvezzi et al., 2008; Hoffman, 2006). In general, the rolling direction depends on the motion of the wheel with respect to the rail. The axes of the contact ellipse, on the other hand, are determined using the principal directions which depend only on the wheel and rail surface geometry and are not

function of any dynamic variables. The normal vector can be defined using the cross product of two tangent vectors defined using the geometry of the rail surface (Kreyszig, 1991; Shabana et al., 2008). The rolling direction can then be defined as the direction of the vector obtained by the cross product of the angular velocity vector and the vector that defines the location of the contact point with respect to the wheel body coordinate system. This direction, therefore, does not explicitly depend on the wheel and rail geometry at the contact point; it depends on the position and angular velocity of the wheel. As a consequence, the use of the RD contact frame for the definition of the creep forces can lead to problems in the traction and braking scenarios when the magnitude of the angular velocity becomes small or in the case of velocity discontinuity due to impact between the vehicle components (Goldsmith, 1960). The switch to the direction of the relative velocity, when the motion becomes predominantly sliding, can also lead to numerical problems and direction discontinuities.

A second choice for the contact frame is to use the normal and the *longitudinal tangent* (LT) which is determined by differentiating the rail surface equation with respect to the longitudinal surface parameter. This choice does not depend on wheel motion variables, and depends only on the rail geometry at the contact point. For this reason, the LT direction is well defined regardless of the motion of the wheel with respect to the rail. Using the cross product of the normal to the surface and the LT vector; the lateral tangent, which represents the direction of the lateral creep force, and consequently, the LT contact frame can be determined in a straight forward manner.

A third choice of the contact frame is to use the surface normal with one of the axes of the *contact ellipse* (CE) used in the Hertz contact theory. The axis closer to the rolling direction

can be selected. In Hertz theory (Hertz, 1882; Johnson, 1985), the directions of the axes of the contact ellipse are determined using the principal directions associated with the principal curvatures. As shown in the literature (Johnson, 1985; Shabana et al., 2008), the directions of the axes of the contact ellipse are functions of the wheel and rail principal directions that depend, respectively, on the geometry of the wheel and rail surfaces. The coefficients of the first and second fundamental forms of surfaces are used to determine the principal curvature and principal directions (Kreyszig, 1991). Therefore, the definition of the CE frame does not also depend on wheel motion variables such as the angular velocity vector.

The RD, LT, and CE contact frames can be different, particularly, in the case of significant lateral deviations or in the case of rails with variable profiles. The RD contact frame, as previously mentioned, is the only frame of the three contact frames discussed in this section that depends on motion variables. While this is the frame which is employed in Kalker's wheel/rail creep theory, Kalker and others assume that the rolling direction is the same as one of the axes of the contact ellipse when Hertz contact theory is used. There are motion scenarios in which the rolling direction can be significantly different from the direction of the axes of the contact ellipse as demonstrated in this investigation. Nonetheless, the dependence of the rolling direction on wheel motion variables such as the angular velocity vector represents a serious limitation in scenarios such as traction and braking. Furthermore, in the case of impacts between the vehicle components the angular velocities of the bodies can be discontinuous, while geometric position variables remain continuous. For this reason, it is important to investigate the accuracy of using other alternatives of contact frames in the formulation of the wheel/rail tangential creep force equations.

### **1.2.2. Wheel/rail Contact Formulations and Algorithms**

The wheel/rail contact analysis has been studied by many researchers in the dynamic modeling of railroad vehicle systems (Kalker, 1990; Shabana et al., 2008). Most contact approaches developed in the previous studies such as the constraint and elastic contact formulations allow for only one or two contact points (Shabana, 2005). Moreover, there have been several investigations on multipoint wheel/rail contact in the literature. Pascal and Sauvage (1991) proposed a new method to reduce multi-contact wheel/rail problem to one equivalent contact patch when the contact points are close to each other. Similar studies were carried out by Piotrowski and Chollet (2005) as well as Ayasse et al. (2000). A nodal search approach was developed by Shabana et al. (2005) but that algorithm was limited to two contact patches. Also, because of geometry discretization adopted in this approach, discontinuities could be encountered in the results. Sugiyama et al. (2009) investigated the wheel/rail contact in the simulation scenarios that include railroad switches using an online contact search algorithm. A linear interpolation method was used in this study to model rail profile variations, which may not be accurate in the case of significant profile variations. Pombo and Ambrosio (2008) developed a method that can be applied for the two contact point scenarios. However, this method can be used in three-dimensional wheel/rail contact analysis.

### **1.2.3. Air Brake Modeling**

One of the most important longitudinal train forces that has a significant effect on the wheel/rail contact forces is the braking force. For this reason, the railroad vehicle brakes have been considered in many investigations (Obara et al., 1995; Balon and Aizinbud, 1989; Guilloux, 1984; Sakamoto et al., 2009). Many studies have focused on the pneumatic or air brake that is

commonly used in the trains in North America (Abdol-Hamid, 1986; Bansiter, 1979; Bharath et al., 1990; Funk and Robe, 1970; Ho, 1981; Limbert, 1991; Wei and Lin, 2009). Shute et al. (1979) investigated the effect of leakage on brake pipe gradients and flow rates. In all of these studies, different aspects of the train air brake were investigated using one-dimensional flow assumption. Gauthier (1977) and Wright (1979) studied the pneumatic control valve systems using a similar assumption. On the other hand, there have been studies that investigated the effect of the air brake on the train longitudinal dynamics. Nasr and Mohammadi (2010) studied the effect of brake delay time on the train longitudinal forces. In this research, one-dimensional motion assumption was employed for the train dynamics and a simple model was used for the air brake. Sanborn et al. (2005) used a simple brake model in which a constant propagation speed is assumed for the brake signal. Such an assumption of constant air propagation speed cannot be justified in many applications and does not allow for accurately predicting car coupler forces in severe braking scenarios.

### **1.3. Scope, Objectives and Organization of the Thesis**

The scope, objectives, and organization of this thesis are summarized as follows:

- In Chapter 2, one of the objectives of this investigation, which is to discuss the fundamental differences between and compare the simulation results obtained by using the RD, LT and CE contact frames is presented. Because of the importance of the geometry in the analysis discussed in Chapter 2 of this thesis, a brief review of the geometry is first presented. The CE frame is function of the principal directions associated with the principal curvatures of the wheel and rail. For this reason, it is important to understand the relationship between the principal

curvatures of the rail surface and the curvatures of the profile and the rail space curves. As shown in Chapter 2, the curvatures of the rail profile and the rail space curve cannot be used in general as the principal curvatures of the rail at the contact point. This is particularly true in the case of the spiral region of the rail or when the rail profile changes as a function of the arc length of the rail space curve. This fundamental geometry problem is discussed in more detail when the CE contact frame is defined in Chapter 2. In order to show the fundamental differences between the RD, LT and CE frames; the equations that define these frames are presented and compared. Numerical examples are presented in order to compare the results obtained using the three different frames. These results are obtained using two different track models; one is a track with significant lateral deviations, while the other is a track which has rails that have variable profiles.

- In Chapter 3, a new multipoint contact search algorithm that can be applied to general three-dimensional wheel/rail contact problems is developed. The algorithm is capable of finding any number of wheel/rail contact points. Furthermore, the algorithm can be used with both constraint and elastic contact approaches. These contact formulations and other assumptions used in the development of the search algorithm are reviewed in Chapter 3. The results obtained using the constraint and elastic contact approaches are compared in the case of multipoint wheel/rail contact. The main steps used in the proposed search algorithm to find all possible contact points are summarized.

- Chapters 4 and 5 develop a new air brake model and explain how this model can be integrated with efficient train longitudinal force algorithms that are based on the trajectory coordinate formulations. The air brake model developed in Chapter 4 consists of the locomotive automatic brake valve, air brake pipe, and car control unit (CCU). The proposed air brake force model accounts for the effect of the air flow in long train pipes as well as the effect of leakage and branch pipe flows. For this reason, this model can be used to study the dynamic behavior of the air flow in the train pipe and its effect on the longitudinal train forces during brake application and release. The governing equations of the air pressure flow are developed using the general fluid continuity and momentum equations, simplified using the assumptions of one dimensional isothermal flow. Using these assumptions, two coupled air velocity/pressure partial differential equations that depend on time and the longitudinal coordinate of the brake pipes are obtained. The partial differential equations, which are converted to a set of first order ordinary differential equations, are solved simultaneously with the train second order nonlinear dynamic differential equations of motion. A new method is presented in this investigation to formulate the finite element model for the brake pipe air, which leads to a constant matrix of coefficients. A detailed model of the locomotive automatic brake valve is presented in Chapter 4 and used to define the inputs to the air brake pipe during the simulation. A simplified model of this valve is also proposed in order to reduce the computational time of the simulation.

- The detailed CCU formulation is presented in Chapter 5. Chapter 5 also focuses on the integration of a train air brake model with a nonlinear train dynamic model that employs the trajectory coordinate formulations. The train air brake forces obtained in Chapter 5 depend on different air brake system components, including the locomotive automatic brake valve, the brake pipe, and the car control unit (CCU). The car brake forces, which depend on the locomotive automatic brake valve handle position and are applied to the wheels using the CCU located along the brake pipe, enter into the formulation of the nonlinear train dynamic equations in addition to other external forces. In order to develop an efficient computational procedure, simplified valve models, with more straightforward operation modes, are considered here in order to reduce the computational overhead. The CCU model used in Chapter 5 has a control valve connected to three main pneumatic components; the auxiliary reservoir, the emergency reservoir, and the brake cylinder. It is also assumed that the CCU modeled in this study has the emergency component that enables applying emergency brake, including the effect of the CCU emergency vent valve. The relationship between the main components of the air brake system and the train dynamics is discussed in Chapter 5, and the final set of differential equations that includes the two models are presented. Furthermore, three different computer simulation scenarios are considered in order to investigate the effect of the air brake forces on the train longitudinal dynamics in the case of different braking modes. The numerical results obtained in Chapter 5 are compared with experimental results published in the literature.

- The thesis is concluded with Chapter 6 that presents the summary and conclusions drawn from this investigation.

## 2. TANGENTIAL CONTACT FORCE

The wheel/rail contact forces have a significant effect on the nonlinear dynamics, and stability of railroad vehicle systems. In general, the wheel/rail contact force can be represented by a normal component and two components that lie on the plane tangent to the wheel and rail at the contact point (Kalker, 1990, 1967; Pascal and Zaazaa, 2007; Shabana et al., 2008). If the wheel/rail relative motion is dominated by rolling, the creep effect must be taken into consideration. The wheel/rail creep forces must be correctly evaluated and used in the nonlinear dynamic equations of railroad vehicle systems for an accurate analysis of the vehicle dynamics.

In some of the wheel/rail creep theories used in railroad vehicle simulations, the direction of the tangential creep forces is assumed to be the wheel *rolling direction* (RD). When Hertz theory is used, an assumption is made that the rolling direction is the direction of one of the axes of the contact ellipse. In principle, the rolling direction depends on the wheel motion, while the direction of the axes of the *contact ellipse* (CE) is determined using the principal directions which depend only on the geometry of the wheel and rail surfaces and do not depend on the motion of the wheel. The RD and CE directions can also be different from the direction of the rail *longitudinal tangent* (LT) at the contact point. In this investigation, the differences between the contact frames that are based on the RD, LT, and CE directions, that enter into the calculation of the wheel/rail creep forces and moments, are discussed. The choice of the frame, in which the contact forces are defined, can be determined using one longitudinal vector and the normal to the rail at the contact point. While the normal vector is uniquely defined, different choices can be made for the longitudinal vector including the RD, LT, and CE directions (See Fig. 1). In the case of pure rolling or when the slipping is small, the RD direction can be defined using the cross

product of the angular velocity vector and the vector that defines the location of the contact point. Therefore, this direction does not depend explicitly on the geometry of the wheel and rail surfaces at the contact point. The LT direction is defined as the direction of the longitudinal tangent obtained by differentiation of the rail surface equation with respect to the rail longitudinal parameter (arc length). Such a tangent does not depend explicitly on the direction of the wheel angular velocity nor does it depend on the wheel geometry. The CE direction is defined using the direction of the axes of the contact ellipse used in Hertz theory. In the Hertzian contact theory, the contact ellipse axes are determined using the principal directions associated with the principal curvatures. Therefore, the CE direction differs from the RD and LT directions in the sense that it is function of the geometry of the wheel and rail surfaces.

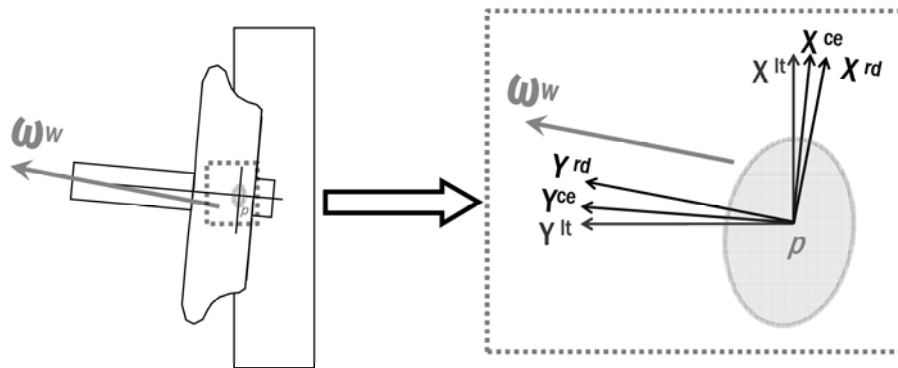


Figure 1. The RD, CE, and LT contact frames

The objective of this chapter is to develop mathematical definitions for the RD, LT and CE contact frames, discuss the fundamental differences between them, and compare the simulation results obtained by using these contact frames. Because of the importance of the geometry in the analysis presented in this study, a brief review of the geometry is first presented.

The CE frame is function of the principal directions associated with the principal curvatures of the wheel and rail. For this reason, it is important to understand the relationship between the principal curvatures of the rail surface and the curvatures of the profile and the rail space curves. As shown in this chapter, the curvatures of the rail profile and the rail space curve cannot be used in general as the principal curvatures of the rail at the contact point. This is particularly true in the case of the spiral region of the rail or when the rail profile changes as a function of the arc length of the rail space curve. This fundamental geometry problem is discussed in more detail when the CE contact frame is defined in this chapter. In order to show the fundamental differences between the RD, LT and CE frames; the equations that define these frames are presented and compared. Numerical examples are presented in order to compare the results obtained using the three different frames. These results are obtained using two different track models; one is a track with significant lateral deviations, while the other is a track which has rails that have variable profiles.

## **2.1. Wheel and Rail Geometry**

In order to accurately model the wheel/rail interaction using nonlinear computational multibody system algorithms, it is necessary to express the wheel and rail surfaces in a parametric form. Before discussing the wheel and rail surface geometry, some basic differential geometry definitions and identities that will be used in this study are reviewed (Kreyszig, 1991).

### **2.1.1. Surface Geometry**

The geometry of a surface can be completely defined using two independent surface parameters  $s_1$  and  $s_2$  as shown in Fig. 2. The position vector  $\mathbf{x}$  of an arbitrary point on the surface can be written in terms of these parameters as

$$\mathbf{x}(s_1, s_2) = [x_1(s_1, s_2) \quad x_2(s_1, s_2) \quad x_3(s_1, s_2)]^T \quad (2.1)$$

where  $x_i, i = 1, 2, 3$ , is component  $i$  of the vector  $\mathbf{x}$ . The tangent and the unit normal vectors of the surface are obtained from the following equation (Kreyszig, 1991):

$$\mathbf{x}_{,1} = \frac{\partial \mathbf{x}}{\partial s_1}, \quad \mathbf{x}_{,2} = \frac{\partial \mathbf{x}}{\partial s_2}, \quad \mathbf{n} = \frac{\mathbf{x}_{,1} \times \mathbf{x}_{,2}}{|\mathbf{x}_{,1} \times \mathbf{x}_{,2}|} \quad (2.2)$$

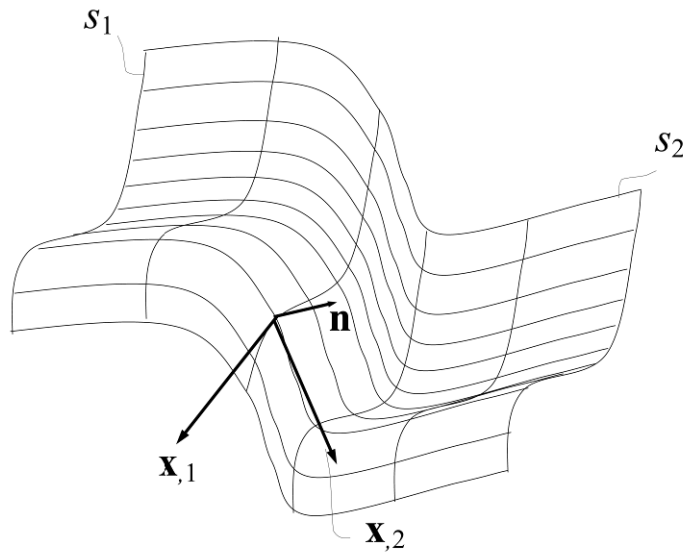


Figure 2 . Surface Geometry

The unit normal vector  $\mathbf{n}$  enters into the definition of all contact frames (RD, LT, and CE) considered in this Chapter. The unit tangent  $\mathbf{t}_1 = \mathbf{x}_{,1} / |\mathbf{x}_{,1}|$  and the normal  $\mathbf{n}$  are used to define the LT contact frame, where the third axis is defined using the cross product. The first fundamental form of the surface is defined as

$$I = d\mathbf{x}^T d\mathbf{x} = E(ds_1)^2 + 2Fds_1ds_2 + G(ds_2)^2 \quad (2.3)$$

where the coefficients in this equation can be written in terms of the tangents of Eq. 2.2 as

$$E = \mathbf{x}_{,1}^T \mathbf{x}_{,1}, \quad F = \mathbf{x}_{,1}^T \mathbf{x}_{,2}, \quad G = \mathbf{x}_{,2}^T \mathbf{x}_{,2} \quad (2.4)$$

The second fundamental form of the surface can be defined as

$$II = -d^2 \mathbf{x}^T \mathbf{n} = L(ds_1)^2 + 2Mds_1ds_2 + N(ds_2)^2 \quad (2.5)$$

where the coefficients of the second fundamental form are

$$L = \mathbf{x}_{,11}^T \mathbf{n}, \quad M = \mathbf{x}_{,12}^T \mathbf{n}, \quad N = \mathbf{x}_{,22}^T \mathbf{n} \quad (2.6)$$

The coefficients of the first and second fundamental forms are used to determine the principal curvatures and principal directions by solving the following homogeneous equation:

$$\begin{bmatrix} L - k_i E & M - k_i F \\ M - k_i F & N - k_i G \end{bmatrix} \begin{Bmatrix} d_{i1} \\ d_{i2} \end{Bmatrix} = \begin{Bmatrix} 0 \\ 0 \end{Bmatrix} \quad i = 1, 2 \quad (2.7)$$

where  $k_i, i=1,2$ , are the principal curvatures (eigenvalues), and  $\mathbf{d}_i = [d_{i1} \quad d_{i2}]^T$  is the eigen vector associated with the eigenvalue  $k_i$  (Kreyszig, 1991). The principal directions can be written in terms of the eigenvectors as

$$\mathbf{e}_i = d_{i1} \mathbf{x}_{,1} + d_{i2} \mathbf{x}_{,2}, \quad i = 1, 2 \quad (2.8)$$

The principal directions are required when Hertz contact theory is used. These directions define the directions of the axes of the contact ellipse. One of these axes is used with the unit normal  $\mathbf{n}$  of Eq. 2.2 to define the CE contact frame axis,  $\mathbf{t}_{ce}$ , which can be used in the formulation of the tangential creep forces. Let  $\psi$  be the angle between the principal axes of the rail and the principal axes of the wheel. The angle  $\alpha$  between principal axes of the rail and the

contact ellipse axis, is obtained using the formula  $\tan 2\alpha = \sin 2\psi / (\cos 2\psi + B_k)$  where  $B_k = (k_x^r - k_y^r) / (k_x^w - k_y^w)$  and  $k_j^l$  ( $l=w,r$  and  $j=x,y$ ) is the principal curvature along the indicated direction obtained using Eq. 2.7. The definition of the contact frames that define the directions of the tangential creep forces will be discussed in the following sections of this chapter.

### 2.1.2. Rail Geometry

The coordinate systems used for the rail in the multibody system algorithm employed in this study are shown in Fig. 3. The rail surface is described using the two parameters  $s_1^r$  (longitudinal) and  $s_2^r$  (profile). The frame  $XYZ$  is the global coordinate system,  $X^{rr}Y^{rr}Z^{rr}$  is the right rail coordinate system, and  $X^{rl}Y^{rl}Z^{rl}$  is the left rail coordinate system. The formulation used in this study allows the right and left rails to be treated as two separate bodies, each of which can have independent displacements; or they can be treated as one body that represents the track. Let  $X^{rp}Y^{rp}Z^{rp}$  be a profile frame, where  $X^{rp}$  is in the direction of the longitudinal tangent to the rail space curve. Without any loss of generality, one can then write the location of a point on the profile in the profile coordinate system as

$$\bar{\mathbf{u}}^{rp} = \begin{bmatrix} 0 & s_2^r & f(s_1^r, s_2^r) \end{bmatrix}^T \quad (2.9)$$

In this equation,  $f(s_1^r, s_2^r)$  is a function that defines the  $Z^{rp}$  coordinate of the point in terms of the rail surface parameters as shown in Fig. 4. The preceding equation represents a general profile that can change along the track. If the profile shape does not change as function of the longitudinal surface parameter  $s_1^r$ , the preceding equation can be written as

$$\bar{\mathbf{u}}^{rp} = [0 \quad s_2^r \quad f(s_2^r)]^T \tag{2.10}$$

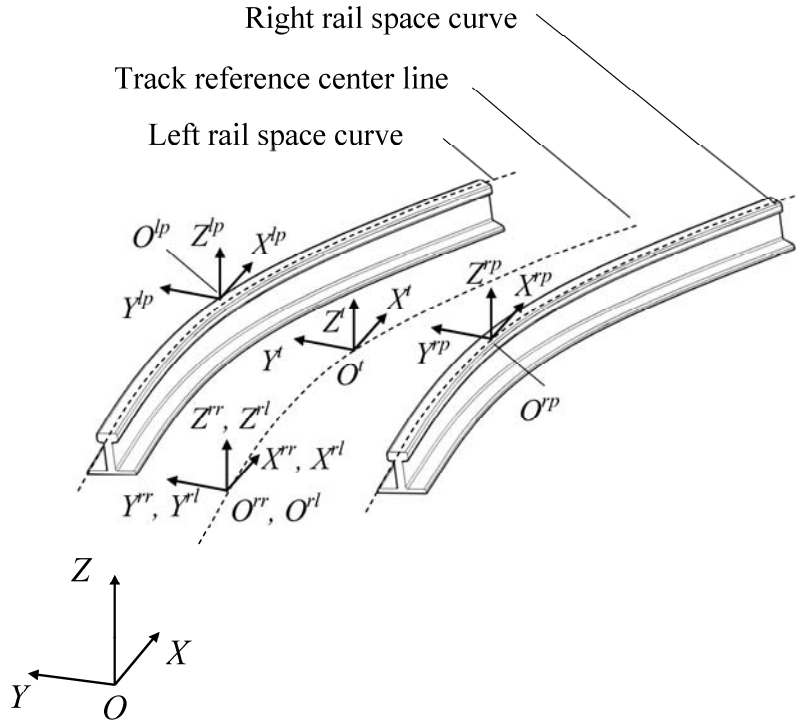


Figure 3. The coordinate systems used to define track geometry

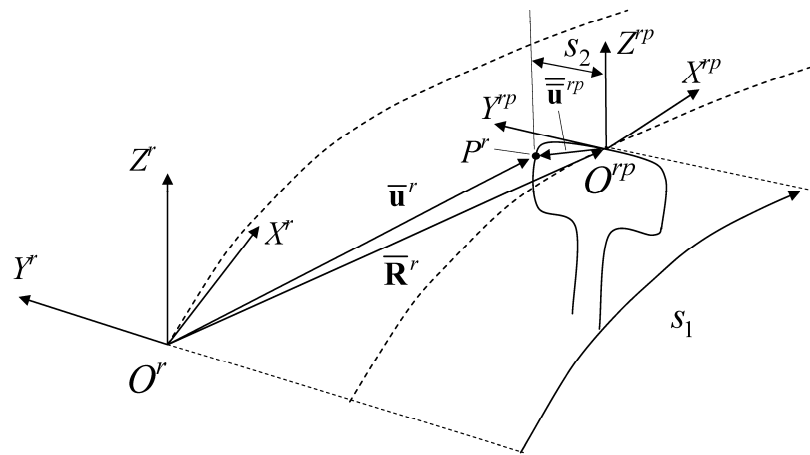


Figure 4. The surface parameters at the contact point of the right rail

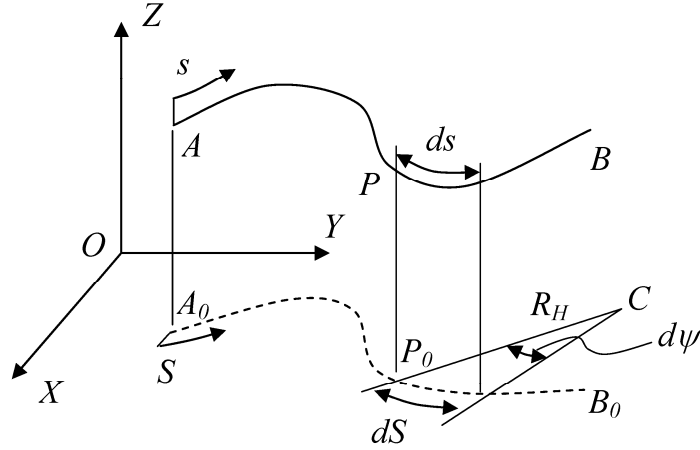


Figure 5. Space curve and the horizontal plane

The location of the contact point with respect to the track or the rail body coordinate system can be written as (Berzeri et al, 2000)

$$\bar{\mathbf{u}}^r = \bar{\mathbf{R}}^r + \bar{\mathbf{A}}^{rp} \bar{\mathbf{u}}^{rp} \quad (2.11)$$

where  $\bar{\mathbf{R}}^r$  and  $\bar{\mathbf{A}}^{rp}$  are, respectively, the location of the origin and the transformation matrix that defines the orientation of the profile frame  $X^{rp}Y^{rp}Z^{rp}$  with respect to the track or rail body coordinate system. The transformation matrix  $\bar{\mathbf{A}}^{rp}$  can be expressed in terms of Euler angles as (Shabana et al., 2008)

$$\bar{\mathbf{A}}^{rp} = \begin{bmatrix} \cos\psi \cos\theta & -\sin\psi \cos\phi + \cos\psi \sin\theta \sin\phi & -\sin\psi \sin\phi - \cos\psi \sin\theta \cos\phi \\ \sin\psi \cos\theta & \cos\psi \cos\phi + \sin\psi \sin\theta \sin\phi & \cos\psi \sin\phi - \sin\psi \sin\theta \cos\phi \\ \sin\theta & -\cos\theta \sin\phi & \cos\theta \cos\phi \end{bmatrix} \quad (2.12)$$

where the three Euler angles  $\psi, \theta$ , and  $\phi$  represent three successive rotations about  $Z, -Y$ , and  $-X$ , respectively. In the multibody system computational algorithm, the location and orientation of the profile frame  $X^{rp}Y^{rp}Z^{rp}$  at points along the track space curve can be defined using three

inputs (Berzeri et al, 2000; Dukkipati and Amyot, 1988). These inputs are the *horizontal curvature* defined by the projection of the curve on the horizontal plane (see Fig. 5), the *grade* defined by the angle  $\theta$ , and the *superelevation* that depends on the bank angle  $\phi$ . Using this input, the relationship between the angle  $\psi$  and the horizontal curvature  $C_H$  can be written as

$$d\psi = C_H dS = \frac{dS}{R_H} \quad (2.13)$$

where  $R_H$  and  $S$  are the radius of curvature and the projected arc length, respectively. Using Fig. 5, the relationship between the actual arc length  $s$  and the projected arc length  $S$  can be written as

$$ds = \frac{dS}{\cos \theta} \quad (2.14)$$

In the computer algorithm used in this chapter for the simulation of multibody railroad vehicle systems, a preprocessor computer code is used to generate track geometry data based on the inputs previously described. The preprocessor output file includes data that are used as input to the main processor computer code SAMS/Rail that is used to solve the nonlinear dynamic equations of the multibody vehicle system (Shabana et al, 2008).

### 2.1.3. Wheel Geometry

Since the wheel surface is considered as a surface of revolution, the position vector of an arbitrary point on the wheel profile with respect to the wheel body coordinate system can be defined as

$$\bar{\mathbf{u}}^w = \left[ x_0 + g(s_1^w) \sin(s_2^w) \quad y_0 + s_1^w \quad z_0 - g(s_1^w) \cos(s_2^w) \right]^T \quad (2.15)$$

where  $s_1^w$  is the lateral surface parameter that defines the geometry of the wheel profile as given by the function  $g(s_1^w)$ ,  $s_2^w$  is the angular surface parameter as shown in Fig. 6, and  $x_0, y_0$ , and  $z_0$  are the coordinates of the position vector of the origin of the profile frame with respect to the wheel or wheelset body coordinate system. As previously mentioned, the principal directions associated with the principal curvatures are used to define the directions of the axes of the contact ellipse. These axes can be used with the normal to define the CE contact frame which can be used in the formulation of the creep forces.

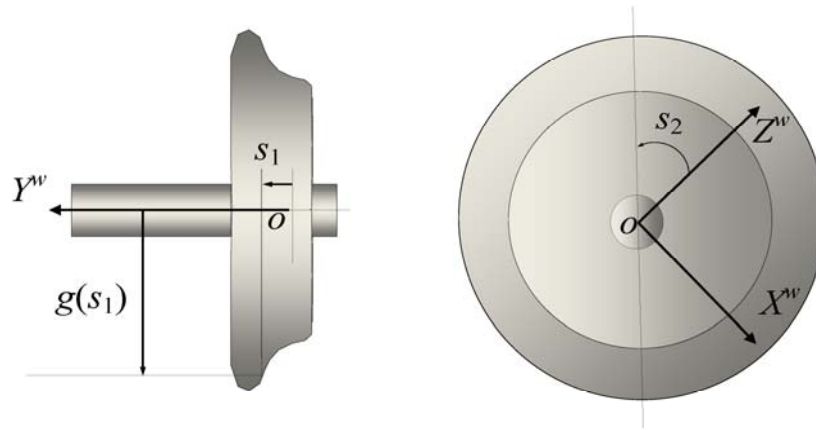


Figure 6. The wheel surface parameters

## 2.2. Rolling Direction (RD) Frame

While the wheel/rail normal contact force is always defined along the normal to the contact surfaces, the direction of the creep forces is defined by the theory used in the formulation of these forces. Different sets of two perpendicular axes can be defined in the tangent plane. In Kalker's nonlinear theory (Kalker, 1990), the RD contact frame in which the creep forces are defined is determined using the unit normal and a unit vector along the rolling direction; with the

third axis defined by the cross product of these two vectors. Kalker and several other authors assume that the rolling direction is the direction of one of the axes of the contact ellipse when Hertz theory is used. In general, the rolling direction, which depends on the motion of the wheel with respect to the rail, can be significantly different from the direction of the axes of the contact ellipse which are determined using the principal directions of the wheel and rail surfaces. The principal directions as discussed in the preceding section are not function of any wheel motion variables. In this section, the rolling direction is defined in a way that is independent of Hertz theory. The rolling direction used in this section is assumed to be the direction of the velocity component due to the rotation of the wheel which is predominantly due to the pitch rotation about the wheelset axis.

The rolling direction enters into the definitions of the creepages and creep contact forces. Let  $\mathbf{v}_c^w$  and  $\mathbf{v}_c^r$  be the absolute velocities of the wheel and the rail at the contact point, and let  $\boldsymbol{\omega}^w$  and  $\boldsymbol{\omega}^r$  be the absolute angular velocities of the two bodies. If the vector  $\mathbf{u}_c^w$  defines the location of the contact point on the wheel, the rolling direction (RD) is defined by the unit vector

$$\mathbf{t}_{rd} = \frac{\mathbf{u}_c^w \times (\boldsymbol{\omega}^w - \boldsymbol{\omega}^r)}{\left| \mathbf{u}_c^w \times (\boldsymbol{\omega}^w - \boldsymbol{\omega}^r) \right|} \quad (2.16)$$

Note that the definition of this unit vector is independent of the normal vector  $\mathbf{n}$ , and therefore, there is no guarantee that this vector lies in the tangent plane. Furthermore, this definition is not an explicit function of the wheel and rail geometry, and can lead to an ill-conditioned definition if the wheel angular velocity becomes small as in the case of traction and braking scenarios. The definition of Eq. 2.16 can also lead to numerical problems in the case of impact between the vehicle components. Impacts lead to jump discontinuities in the velocities,

and as a consequence, the use of the preceding equation in the formulation of the creepages and creep forces can be a source of problems in some railroad vehicle simulation scenarios.

Using Eq. 2.16, the orientation of the RD frame can be defined using the following transformation matrix:

$$\mathbf{A}_{rd} = \begin{bmatrix} \mathbf{t}_{rd} & (\mathbf{n} \times \mathbf{t}_{rd}) & \mathbf{n} \end{bmatrix} \quad (2.17)$$

Note that, in general, there is no guarantee that the vector  $\mathbf{t}_{rd}$  lies in the tangent plane. For this reason, this vector can be replaced by another vector obtained by the cross product  $\mathbf{t}_{rd} = (\mathbf{n} \times \mathbf{t}_{rd}) \times \mathbf{n} / |(\mathbf{n} \times \mathbf{t}_{rd}) \times \mathbf{n}|$ . Using the RD frame definition, the vector  $\mathbf{n} \times \mathbf{t}_{rd} = \mathbf{t}_{lr}$  defines the direction of the lateral creepage and lateral creep force. In this case, the creepages can be written as

$$\xi_x = \frac{(\mathbf{v}_c^w - \mathbf{v}_c^r)^T \mathbf{t}_{rd}}{V}, \quad \xi_y = \frac{(\mathbf{v}_c^w - \mathbf{v}_c^r)^T \mathbf{t}_{lr}}{V}, \quad \xi_\phi = \frac{(\boldsymbol{\omega}^w - \boldsymbol{\omega}^r)^T \mathbf{n}}{V} \quad (2.18)$$

where  $\xi_x$  and  $\xi_y$  are the longitudinal and lateral creepages, respectively;  $\xi_\phi$  is the spin creepage; and  $V$  is the forward velocity of the wheel. The creepage expressions of Eq. 2.18 can be used with the normal force, the wheel and rail material properties, and the contact ellipse semi-axes to evaluate the tangential creep forces and the spin moment which are defined along the axes of the RD frame.

### **2.3. Contact Ellipse (CE) Frame**

The CE frame is formed using the normal vector and one of the axes of the contact ellipse used in Hertz contact theory. The axis closer to the direction of the forward motion of the wheel can be selected. Let a unit vector along the axis of the contact ellipse be denoted as  $\mathbf{t}_{ce}$  which was

previously defined. Using this unit vector and the unit normal  $\mathbf{n}$ , the third axis can be defined using the unit vector

$$\mathbf{t}_{lc} = \mathbf{n} \times \mathbf{t}_{ce} \quad (2.19)$$

This vector defines the direction of the lateral creepage and the lateral creep force. Therefore, the transformation matrix that defines the orientation of the CE frame can be written as

$$\mathbf{A}_{ce} = \begin{bmatrix} \mathbf{t}_{ce} & (\mathbf{n} \times \mathbf{t}_{ce}) & \mathbf{n} \end{bmatrix} \quad (2.20)$$

The creepage expressions when the CE frame is used can be written as

$$\xi_x = \frac{(\mathbf{v}_c^w - \mathbf{v}_c^r)^T \mathbf{t}_{ce}}{V}, \quad \xi_y = \frac{(\mathbf{v}_c^w - \mathbf{v}_c^r)^T \mathbf{t}_{lc}}{V}, \quad \xi_\phi = \frac{(\boldsymbol{\omega}^w - \boldsymbol{\omega}^r)^T \mathbf{n}}{V} \quad (2.21)$$

In order to accurately define the axes of the contact ellipse used to define the CE frame introduced in this chapter it is necessary to determine online the principal directions associated with the principal curvatures of the wheel and rail at the contact point. The rail, in particular, can have complex geometry in regions such as the spirals and also due to the variation of the rail profile in the longitudinal direction due to wear or the existence of switches and turnouts. The principal curvatures of the rail, as shown in the remainder of this section, cannot be assumed in general to be equal to the curvature of the rail profile and the curvature of the rail longitudinal curve at the contact point. Therefore, it is necessary to determine the principal curvatures by solving, at every time step, the eigenvalue problem defined in the previous section of this thesis. This eigenvalue problem is formulated using the coefficients of the first and second fundamental forms of the rail surface, as discussed in the preceding section. The conditions under which the

rail principal curvatures reduce to the curvature of the profile and the curvature of the rail longitudinal curve at the contact point are also presented in this section.

The two tangents to the rail surface can be defined using Eq. 2.11 as follows:

$$\bar{\mathbf{u}}_{,1}^r = \bar{\mathbf{R}}_{,1}^r + \bar{\mathbf{A}}_{,1}^{rp} \bar{\mathbf{u}}_{,1}^{rp} + \bar{\mathbf{A}}^{rp} \bar{\mathbf{u}}_{,1}^{rp}, \quad \bar{\mathbf{u}}_{,2}^r = \bar{\mathbf{A}}^{rp} \bar{\mathbf{u}}_{,2}^{rp} \quad (2.22)$$

In general, these two tangents are not orthogonal. Their dot product is given by

$$\bar{\mathbf{u}}_{,1}^{rT} \bar{\mathbf{u}}_{,2}^r = \bar{\mathbf{R}}_{,1}^{rT} \bar{\mathbf{A}}^{rp} \bar{\mathbf{u}}_{,2}^{rp} + \bar{\mathbf{u}}_{,1}^{rpT} \bar{\mathbf{A}}_{,1}^{rpT} \bar{\mathbf{A}}^{rp} \bar{\mathbf{u}}_{,2}^{rp} + \bar{\mathbf{u}}_{,1}^{rpT} \bar{\mathbf{u}}_{,2}^{rp} \quad (2.23)$$

The first term in the right hand side of the preceding equation vanishes since the vectors  $\bar{\mathbf{R}}_{,1}^r$  and  $\bar{\mathbf{A}}^{rp} \bar{\mathbf{u}}_{,2}^{rp}$  are always perpendicular, while the second term can be simplified using the properties of the transformations matrix, leading to

$$\bar{\mathbf{u}}_{,1}^{rpT} \bar{\mathbf{A}}_{,1}^{rpT} \bar{\mathbf{A}}^{rp} \bar{\mathbf{u}}_{,2}^{rp} = -\bar{\mathbf{u}}_{,1}^{rpT} \tilde{\bar{\boldsymbol{\sigma}}} \bar{\mathbf{u}}_{,2}^{rp} \quad (2.24)$$

where  $\tilde{\bar{\boldsymbol{\sigma}}} = \bar{\mathbf{A}}^{rpT} \bar{\mathbf{A}}_{,1}^{rp}$  is a skew symmetric matrix. The vector  $\bar{\boldsymbol{\sigma}}$  associated with  $\tilde{\bar{\boldsymbol{\sigma}}}$  is defined in the rail body coordinate system. Using the preceding two equations, one has

$$\begin{aligned} \bar{\mathbf{u}}_{,1}^{rT} \bar{\mathbf{u}}_{,2}^r &= -\bar{\mathbf{u}}_{,1}^{rpT} \tilde{\bar{\boldsymbol{\sigma}}} \bar{\mathbf{u}}_{,2}^{rp} + \bar{\mathbf{u}}_{,1}^{rpT} \bar{\mathbf{u}}_{,2}^{rp} = -\bar{\mathbf{u}}_{,1}^{rp} \cdot (\bar{\boldsymbol{\sigma}} \times \bar{\mathbf{u}}_{,2}^{rp}) + \bar{\mathbf{u}}_{,1}^{rp} \cdot \bar{\mathbf{u}}_{,2}^{rp} \\ &= \bar{\sigma}_x (s_2^r f_{,2}(s_1^r, s_2^r) - f(s_1^r, s_2^r)) + f_{,1}(s_1^r, s_2^r) f_{,2}(s_1^r, s_2^r) \end{aligned} \quad (2.25)$$

The terms that appear in the right hand side of this equation are not in general equal to zero. In the special case in which the profile does not change its shape along the track, that is,  $f_{,1}(s_1^r, s_2^r) = 0$ , the preceding equation reduces to  $\bar{\mathbf{u}}_{,1}^{rT} \bar{\mathbf{u}}_{,2}^r = \bar{\sigma}_x (s_2^r f_{,2}(s_1^r, s_2^r) - f(s_1^r, s_2^r))$ , which shows that the two tangents are perpendicular in this special case if and only if  $\bar{\sigma}_x = 0$ . This condition is satisfied if

$$\bar{\sigma}_x = -\phi_{,1} + \psi_{,1} \sin \theta = 0 \quad (2.26)$$

Using this condition, one can evaluate the coefficients of the first and second fundamental forms and determine the principal curvatures and principal directions. One can show that, in this special case, the principal directions are the same as the rail unit tangents  $\mathbf{t}_1^r$  and  $\mathbf{t}_2^r$ . The principal curvatures and the associated principal directions in this special case are

$$\left. \begin{aligned} k_1 &= \frac{L}{E} , & \mathbf{e}_1^r &= \mathbf{t}_1^r \\ k_2 &= \frac{N}{G} , & \mathbf{e}_2^r &= \mathbf{t}_2^r \end{aligned} \right\} \quad (2.27)$$

Therefore, if the profile does not change its shape, one has the following results for different types of the track segments (tangent, curve or spiral):

1. In the case of a *tangent track*,  $\phi_{,1} = \psi = \theta = 0$  and the two unit tangents  $\mathbf{t}_1^r$  and  $\mathbf{t}_2^r$  are perpendicular. The principal curvatures of a tangent track segment reduce to the curvatures of the rail space curve and the profile curve. The results are

$$\left. \begin{aligned} k_1 &= 0, & \mathbf{e}_1^r &= \mathbf{t}_1^r \\ k_2 &= \frac{f_{,22}(s_2^r)}{\sqrt{(1+[f_{,2}(s_2^r)]^2)^3}}, & \mathbf{e}_2^r &= \mathbf{t}_2^r \end{aligned} \right\} \quad (2.28)$$

2. In the case of a *curve segment*, one has  $\phi_{,1} = \theta = 0$  while  $\psi_{,1}$  is constant. Again, for such a segment, the two unit tangents  $\mathbf{t}_1^r$  and  $\mathbf{t}_2^r$  are perpendicular and the second principal curvature  $k_2$  reduces to the curvature of the rail profile curve. The results in this special case, assuming  $R$  is the radius of curvature of the rail space curve segment, are

$$\left. \begin{aligned} k_1 &= -\frac{f_{,2}(s_2^r)}{(R-s_2^r)\sqrt{1+[f_{,2}(s_2^r)]^2}}, & \mathbf{e}_1^r &= \mathbf{t}_1^r \\ k_2 &= \frac{f_{,22}(s_2^r)}{\sqrt{(1+[f_{,2}(s_2^r)]^2)^3}}, & \mathbf{e}_2^r &= \mathbf{t}_2^r \end{aligned} \right\} \quad (2.29)$$

3. In the case of a *spiral segment*, the conditions used for the tangent and curve segments cannot be applied because of the more complex spiral geometry. In fact, the solution for a spiral is a *clothoid*. Within a spiral, the Euler angles change with respect to the arc length such that in general the two unit tangents  $\mathbf{t}_1^r$  and  $\mathbf{t}_2^r$  do not remain perpendicular. In this case, the principal directions are a linear combination of the two surface tangents  $\mathbf{t}_1^r$  and  $\mathbf{t}_2^r$ .

One can also develop similar conditions for the wheel. The wheel tangents are defined as follows:

$$\bar{\mathbf{u}}_{,1}^w = [g_{,1} \sin(s_2^w) \quad 1 \quad g_{,1} \cos(s_2^w)]^T, \quad \bar{\mathbf{u}}_{,2}^w = [g \cos(s_2^w) \quad 0 \quad -g \sin(s_2^w)]^T \quad (2.30)$$

Using these definitions, one can show that the dot product of the two unit tangents  $\mathbf{t}_1^w = \bar{\mathbf{u}}_{,1}^w / |\bar{\mathbf{u}}_{,1}^w|$  and  $\mathbf{t}_2^w = \bar{\mathbf{u}}_{,2}^w / |\bar{\mathbf{u}}_{,2}^w|$  is equal to zero regardless of the wheel profile  $g(s_1^w)$ . It can be shown that for the wheel surface, the coefficient  $M$  of the second fundamental form is also equal to zero. Therefore, the principal directions are the same as the directions the unit tangents  $\mathbf{t}_1^w$  and  $\mathbf{t}_2^w$ , and one has the following results (Shabana et al., 2001):

$$\left. \begin{aligned} k_1 &= \frac{g_{,11}(s_1^w)}{\sqrt{(1+[g_{,1}(s_1^w)]^2)^3}}, & \mathbf{e}_1^w &= \mathbf{t}_1^w \\ k_2 &= \frac{-1}{g(s_1^w)\sqrt{1+[g_{,1}(s_1^w)]^2}}, & \mathbf{e}_2^w &= \mathbf{t}_2^w \end{aligned} \right\} \quad (2.31)$$

These results apply only to unworn wheels.

## 2.4. Longitudinal Tangent (LT) Frame

Another choice for the contact frame is to use the unit normal  $\mathbf{n}$  and the longitudinal tangent  $\mathbf{t}'_1$  as defined in the preceding section to form the LT contact frame. In this case, the orientation of the contact frame is defined by the transformation matrix

$$\mathbf{A}_{lt} = [\mathbf{t}'_1 \quad (\mathbf{n} \times \mathbf{t}'_1) \quad \mathbf{n}] \quad (2.32)$$

The vector  $\mathbf{n} \times \mathbf{t}'_1 = \mathbf{t}_{l1}$  defines the lateral tangent along which the lateral creepage and lateral creep force are defined. The creepage expressions when the LT frame is used can be written as

$$\xi_x = \frac{(\mathbf{v}_c^w - \mathbf{v}_c^r)^T \mathbf{t}'_1}{V}, \quad \xi_y = \frac{(\mathbf{v}_c^w - \mathbf{v}_c^r)^T \mathbf{t}_{l1}}{V}, \quad \xi_\phi = \frac{(\boldsymbol{\omega}^w - \boldsymbol{\omega}^r)^T \mathbf{n}}{V} \quad (2.33)$$

The definition of the LT frame does not involve the angular velocity vector, and if Hertz contact theory is not used, the evaluation of the principal curvatures and principal directions is not required. Furthermore, the LT contact frame differs from the other two frames previously discussed in the sense that it does not depend on the wheel motion or geometry. It depends only on the rail geometry at the contact point.

As previously pointed out, the two tangents  $\mathbf{t}'_1$  and  $\mathbf{t}'_2$  are not in general perpendicular. Therefore, one can define another contact frame using the unit normal vector  $\mathbf{n}$  and the lateral tangent  $\mathbf{t}'_2$ . The longitudinal axis that completes the frame can be determined using the cross product. Numerical experimentation conducted in this study have shown that the results obtained using the contact frame formed by  $\mathbf{n}$  and  $\mathbf{t}'_2$  are in a good agreement with the results obtained using the LT contact frame. Therefore, the contact frame based on the  $\mathbf{n} - \mathbf{t}'_2$  combination will not be discussed further in this chapter.

## 2.5. Multibody Contact Formulations

In order to study the wheel/rail dynamic interaction, the normal force at the contact point must be calculated and used with other material and geometric parameters to determine the tangential creep forces and spin moment. There are two general approaches that can be used to study the wheel/rail interaction; these are the *constraint* and *elastic* approaches (Shabana et al, 2008). In the constraint approach, it is assumed that there is no penetration or separation between the wheel and the rail at the contact point. Since four geometric parameters are introduced to describe the wheel and rail surface geometry, the following five constraint equations can be imposed:

$$\begin{bmatrix} \mathbf{t}_1^r \cdot (\mathbf{r}_p^w - \mathbf{r}_p^r) \\ \mathbf{t}_2^r \cdot (\mathbf{r}_p^w - \mathbf{r}_p^r) \\ \mathbf{n}^r \cdot (\mathbf{r}_p^w - \mathbf{r}_p^r) \\ \mathbf{t}_1^w \cdot \mathbf{n}^r \\ \mathbf{t}_2^w \cdot \mathbf{n}^r \end{bmatrix} = \mathbf{0} \quad (2.34)$$

where  $\mathbf{r}_p^l$  is the absolute position vector that defines the location of the contact point  $P$  on the body  $l$  ( $l=w, r$ ). When the constraint formulation is used, the normal force at the contact point is considered as a reaction force which can be determined using the technique of Lagrange multipliers. In the case of the constraint contact approach, the constraints defined in the preceding equation must be satisfied at the position, velocity, and acceleration levels.

On the other hand, in the elastic approach that will be used in this study, the wheel has six degrees of freedom with respect to the rail, and therefore, wheel/rail penetration and separation are allowed. In this approach, the third constraint in the preceding equation, which specifies the relative motion of the two surfaces along their common normal, is not imposed while the other

four nonlinear algebraic equations are used to solve for the four geometric surface parameters. In the elastic approach, the normal force is defined as a function of the penetration using the Hertzian contact formulation. The penetration can be calculated as

$$\delta = (\mathbf{r}_p^w - \mathbf{r}_p^r) \mathbf{n}^r = \mathbf{r}_p^{wrT} \mathbf{n}^r \quad (2.35)$$

Using this definition for the penetration, the normal contact force can be determined. A damping coefficient can also be introduced to the force-penetration relationship to take into account the effect of the energy dissipation. Therefore, the normal force can be written as follows (Shabana et al 2005):

$$F_n = F_h + F_d = -K_h \delta^{\frac{3}{2}} - C \dot{\delta} |\delta| \quad (2.36)$$

where  $K_h$  is the Hertzian constant (Johnson, 1985) ,  $C$  is the damping constant,  $\dot{\delta}$  is the indentation velocity obtained from the dot product of the wheel/rail relative velocity at the contact point and the normal vector to the surface at this point.

The expressions of the wheel/rail normal and tangential creep forces can be introduced to the nonlinear dynamic equations of motion of the railroad vehicle system as generalized forces. These equations can be solved for the system accelerations and joint forces. The accelerations can be integrated forward in time in order to determine the coordinates and velocities as described in detail in the literature (Shabana et al., 2008).

## **2.6. Numerical Results**

In this section, simulation results of suspended wheelset examples using the RD, LT, and CE contact frames are presented and compared. These simulations include rails with constant profile shape as well as profiles that change their shape along the rail arc length. While in both cases a

tangent track is used; in the first case, a track with significant lateral deviation is used in order to compare the results obtained using different contact frames. Ultimately, in order to show the difference between the three frames in extreme cases, the track deviation in the first simulation, is increased to a large deviation and the results are also presented in this section.

### **2.6.1. Track with Lateral Deviation**

In this example, a wheelset attached to a frame that is constrained to move along a tangent track is considered. It is assumed that there is a lateral deviation starting at distance 15.24 m (50 ft) with amplitude of 0.0152 m (0.6 in) and width of 1.524 m (5 ft). This deviation causes the principal directions of the rail to change. Since the wheelset motion is affected by the deviation, the angle between the principal directions of the wheel and the rail in this portion of the track is expected to be much higher as compared to the remaining sections of the track. The wheelset is assumed to have a constant forward velocity of 10 m/s (22.4 mph) along the track. The results are obtained for three models that correspond to the three different contact frames discussed in this study. Figures 7 and 8 show, respectively, the lateral displacement and the angle of attack (right wheel) of the wheelset when the three frames are used.

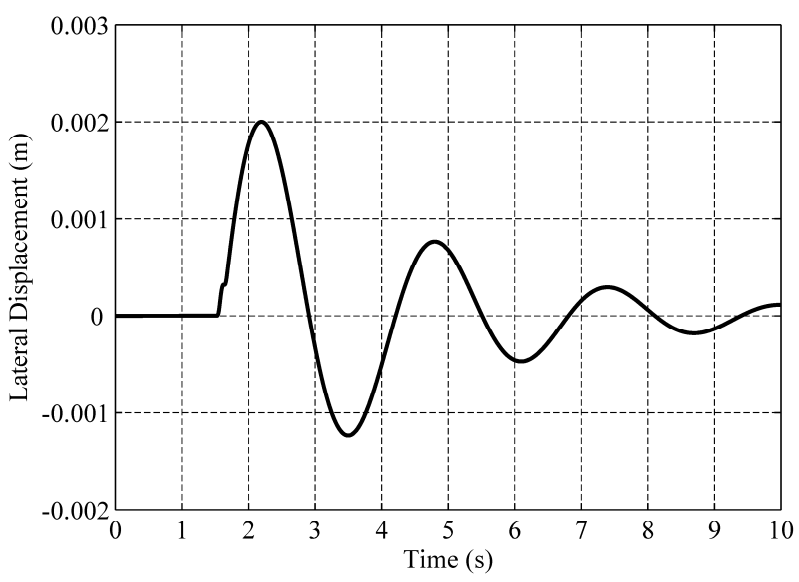


Figure 7. Lateral displacement of the wheelset  
(CE frame: ———, LT frame: - - - -, RD frame:.....)

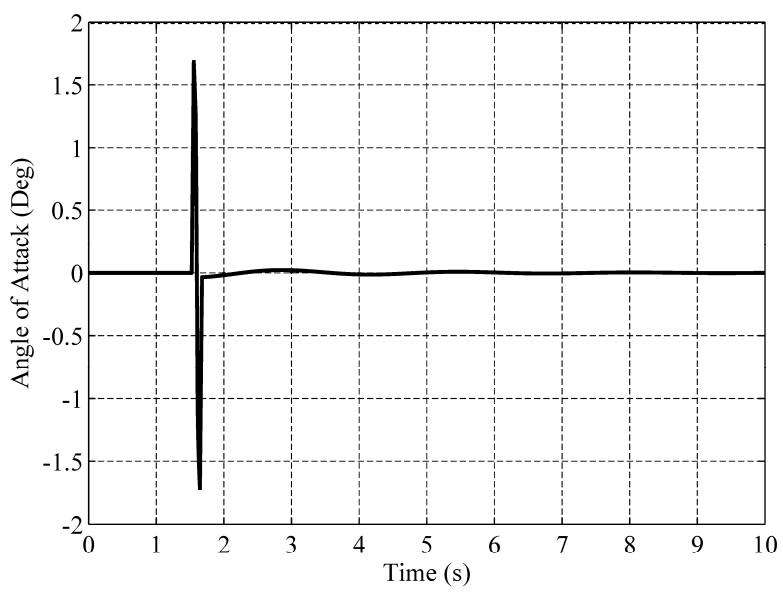


Figure 8. Angle of attack at the right wheel  
(CE frame: ———, LT frame: - - - -, RD frame:.....)

Figures 9-11 show the normal and tangential creep forces. Figure 12 shows the angle between the rolling direction of the RD frame and the principal direction used to define one of the axes of the contact ellipse, while Fig. 13 shows the angle between the principal direction and the longitudinal tangent at the contact point.

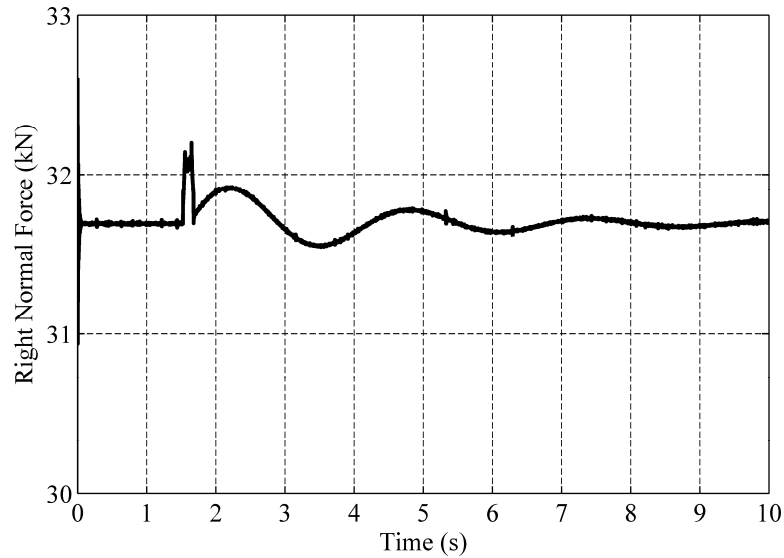


Figure 9. Normal force at the right wheel  
(CE frame: ———, LT frame: \_ \_ \_ \_ , RD frame:.....)

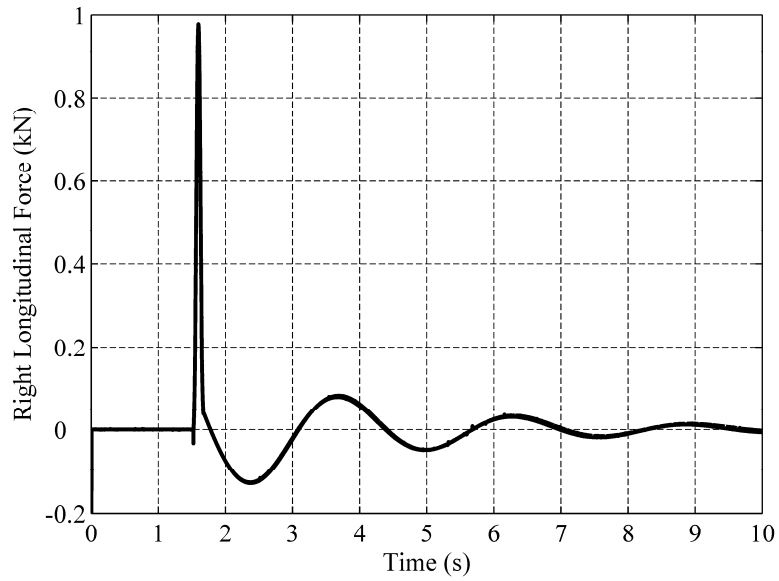


Figure 10. Longitudinal force at the right wheel  
(CE frame: ———, LT frame: - - - -, RD frame:.....)

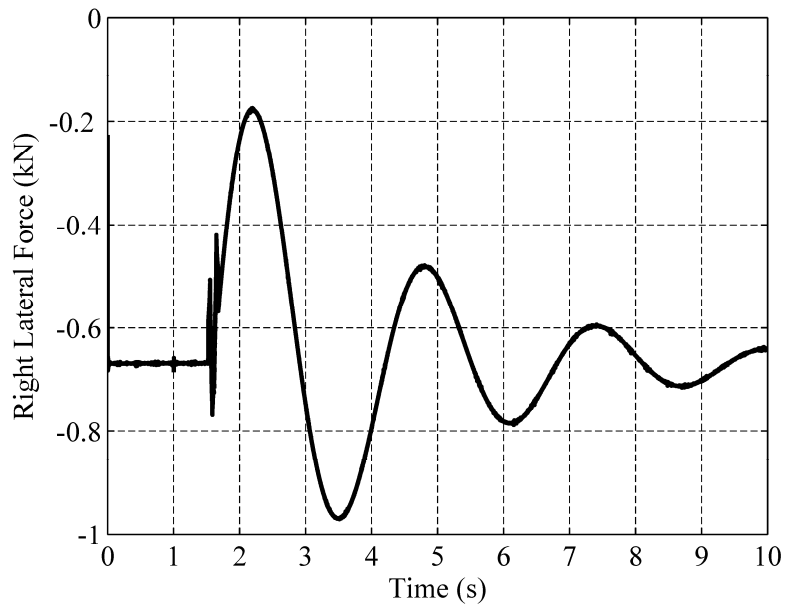


Figure 11. Lateral force at the right wheel  
(CE frame: ———, LT frame: - - - -, RD frame:.....)

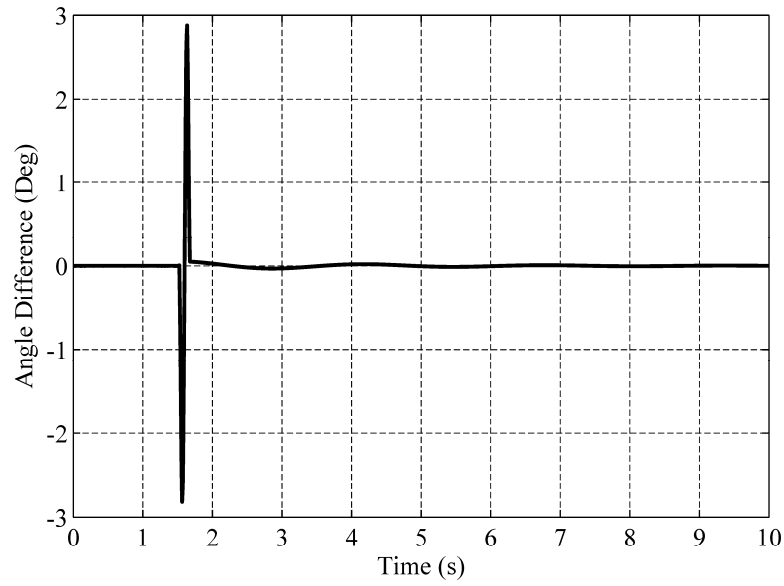


Figure 12. The angle between the RD and the CE frames

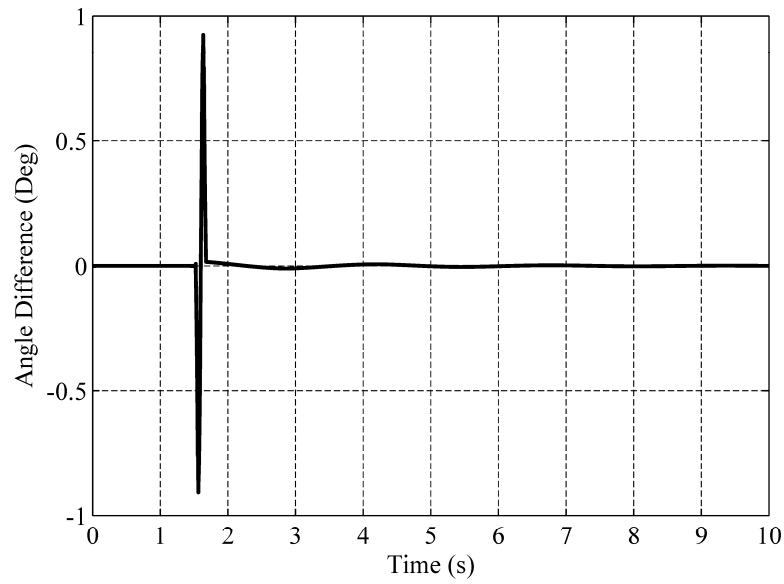


Figure 13. The angle between the LT and the CE frames

Figures 14-16 show the global components of the contact forces. Figures 17 and 18 show the longitudinal and lateral creepages defined in the contact frame.

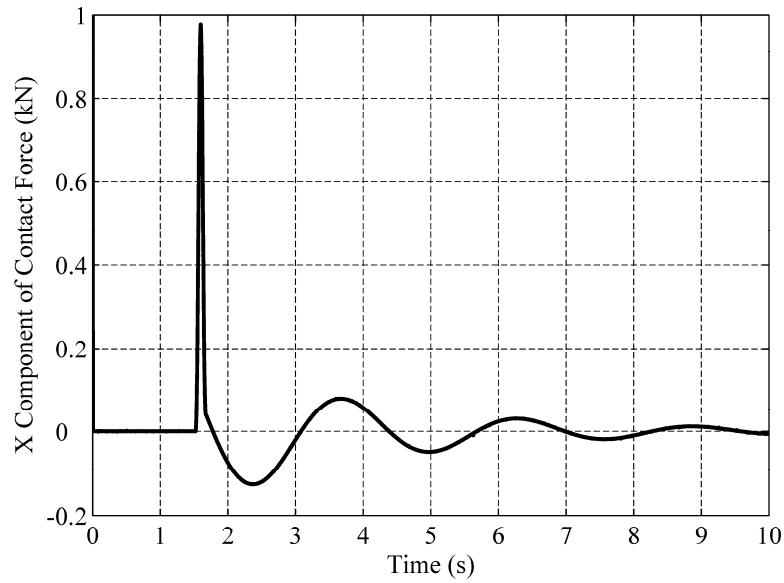


Figure 14. X component of the right contact force in the global coordinate system (CE frame: ———, LT frame: - - - -, RD frame:.....)

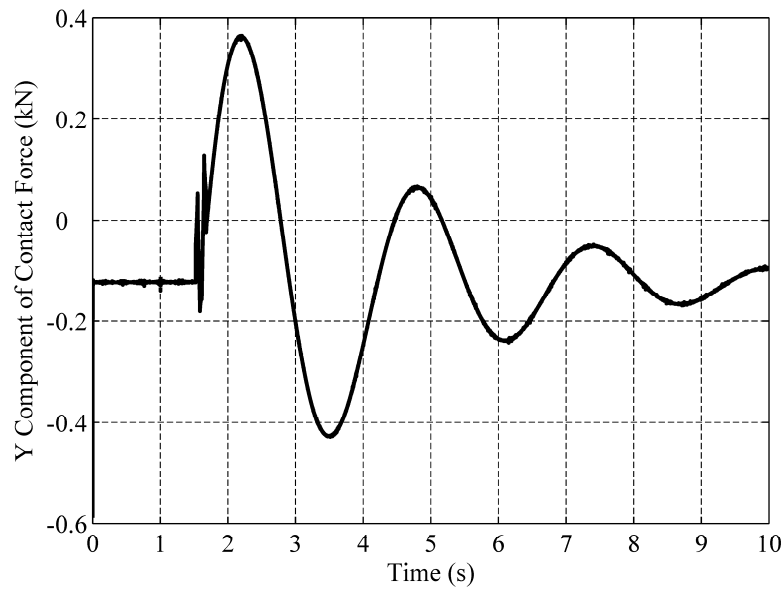


Figure 15. Y component of the right contact force in the global coordinate system (CE frame: ———, LT frame: - - - -, RD frame:.....)

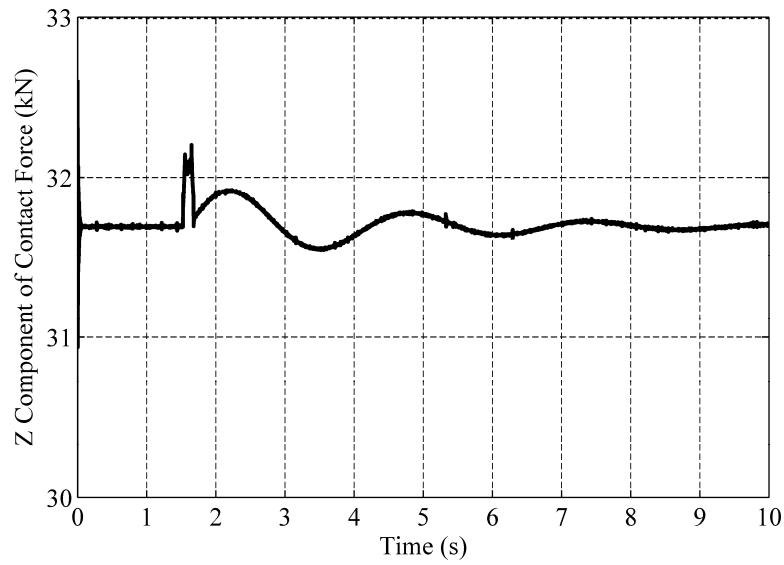


Figure 16. Z component of the right contact force in the global coordinate system  
(CE frame: ———, LT frame: - - - -, RD frame:.....)

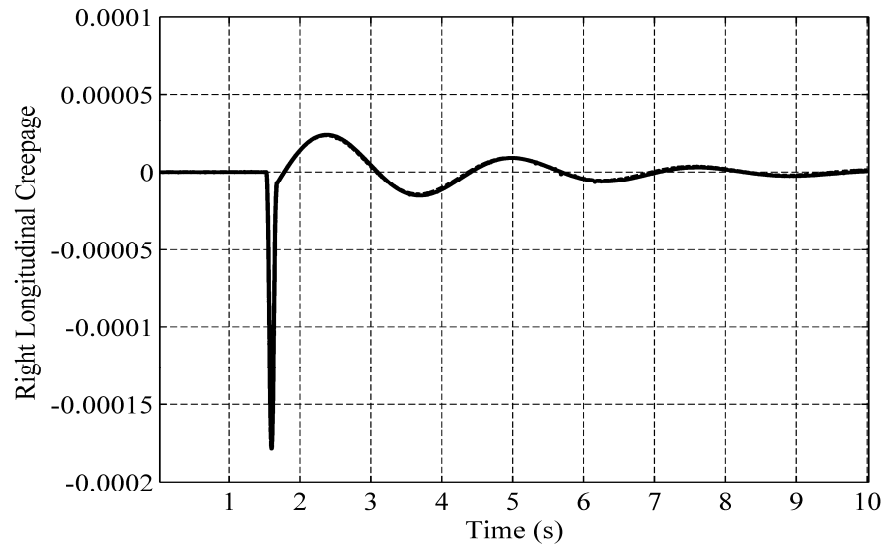


Figure 17. Longitudinal creepage at the right wheel  
(CE frame: ———, LT frame: - - - -, RD frame:.....)

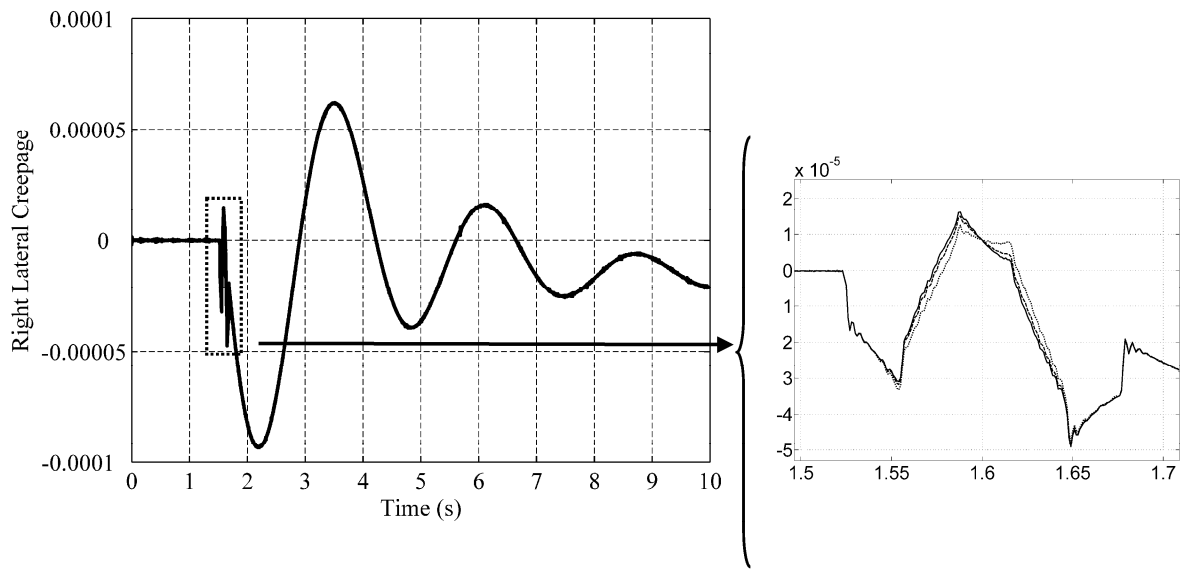


Figure 18. Lateral creepage at the right wheel  
(CE frame: ———, LT frame: - - - -, RD frame:.....)

The percentage of the average deviation of the RD and LT models from the CE model, when the wheelset passes over the deviation, is shown in Table I.

Table I. The average deviation of the RD and LT models from the CE model

Parameter	LT model	RD model
Right longitudinal creepage	1.5%	5%
Lateral axis of the left contact ellipse	0.002%	0.003%
Right longitudinal force	1.5%	5%
Right lateral force	0.7%	2.2%
Left spin creepage	0.02%	0.05%
Right spin moment	0.6%	2%
Right contact area	0.005%	0.005%
Right lateral creepage	3%	11%
X component of the right creepage in the global coordinate system	3%	5%
Y component of the right creepage in the global coordinate system	1%	1%
Left normal force	0.007%	0.008%
X component of the right contact force in the global coordinate system	0.3%	1.3%
Y component of the right contact force in the global coordinate system	0.4%	0.7%
Z component of the right contact force in the global coordinate system	0.007%	0.008%

The results obtained show that the contact force results of different models are in a good agreement, while discrepancies in the creepage results can be observed. Simulation results have shown that the discrepancy in the lateral creepage does not have a significant effect on the creep force due to the dominant effect of the spin creepage in the lateral force calculation.

### **2.6.2. Track with Variable Profile**

In this example, the suspended wheelset is constrained to move along the tangent track with a forward velocity of 10 m/s (22.4 mph). The track profile is assumed to vary along the track. The profiles used to define the right rail are shown in Fig. 19. The order of these profiles are as

follows: the cross-sections of the right rail at the distances 0, 20 m (65.6 ft), 120 m (393.7 ft) and 220 m (721.8 ft) are assumed to have the shapes described by the profiles with numbers 1, 1, 2, and 3, respectively.

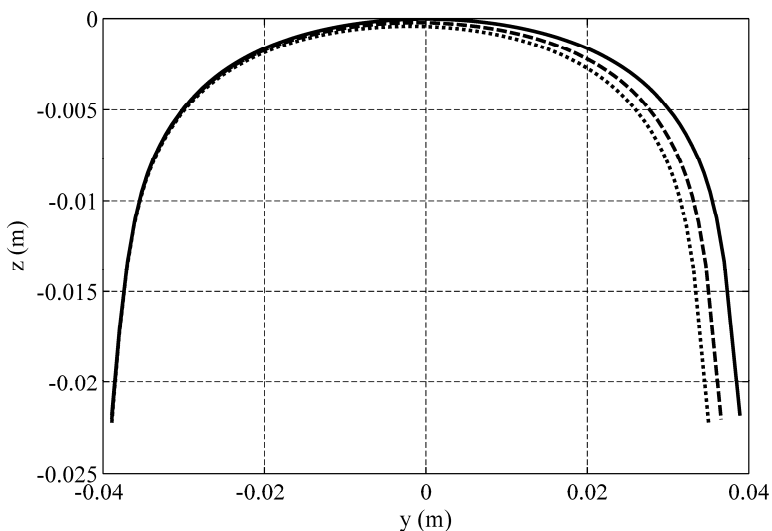


Figure 19. Right rail profiles  
(Profile #1: ———, Profile #2: - - - -, Profile #3: .....)

These profiles are also mirrored and used at the same locations for the left rail. Linear interpolation is used to define the profile shape at a distance between the locations of the profiles shown in Fig. 19. Figure 20 shows the lateral tangential creep forces as defined in the contact frames of the three different models. Numerical results obtained in this chapter showed that the normal force and longitudinal tangential creep force obtained using the models based on the three frames are in a good agreement. Furthermore, the solutions for the wheel kinematics, such as the wheel displacements and yaw angles, as well the dimensions of the contact ellipse are in a good agreement. Figures 21 and 22 show the angles between the axes of the contact frames. The results obtained for this track model show that the profile variation does not have a significant

effect on the creepages and contact forces of the RD, CE, and LT models. The deviations of the RD and LT model results from the CE model results is less than 0.1% for the track model used in this study.

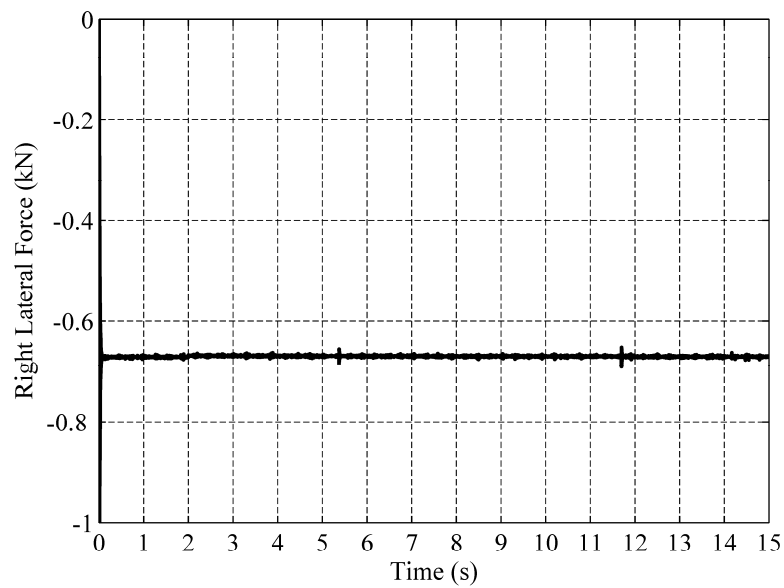


Figure 20. Lateral force at the right wheel  
(CE frame: ———, LT frame: - - - -, RD frame:.....)

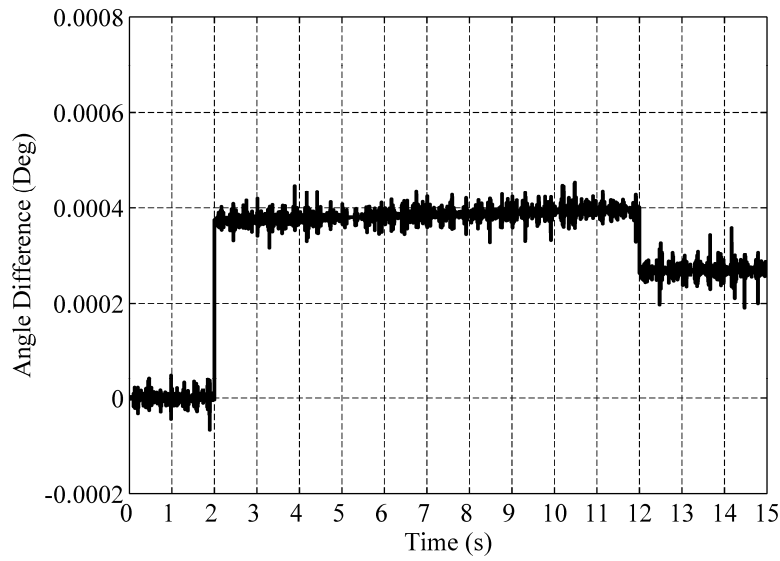


Figure 21. The angle between the RD and the CE frames

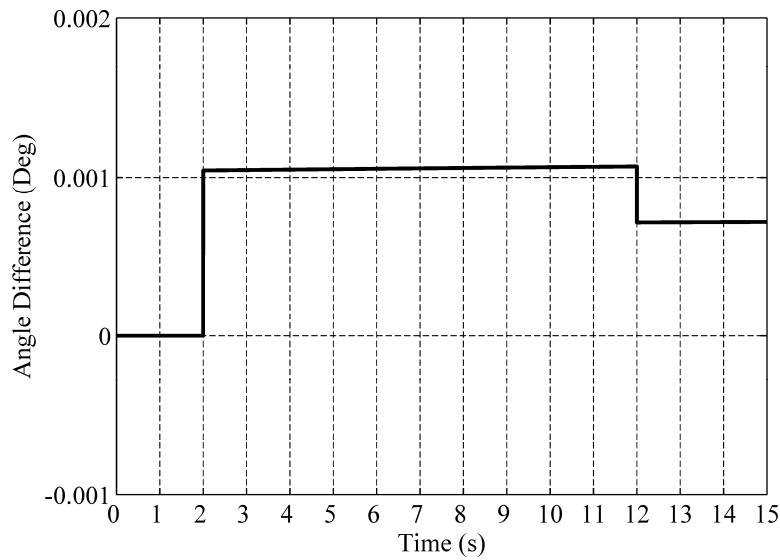


Figure 22. The angle between the LT and the CE frames

### 2.6.3. Extreme Case

The simulations used to obtain the results previously discussed in this section, represent realistic scenarios. As observed, in such simulation scenarios, the results obtained using all contact

frames are in a good agreement. However, in order to show the differences in the results obtained using the three frames in extreme cases, an uncommon track model, is used. In the new track model, the width and amplitude of the deviation are changed to 0.6096 m (2 ft) and 0.0254 m (1 in), respectively.

Table II. The average deviation of the RD and LT models from the CE model

Parameter	LT model	RD model
Right longitudinal creepage	7%	21%
Right lateral force	10%	22%
Left spin moment	9%	18%
Right longitudinal force	7%	21%
Right spin creepage	0.5%	2%
Right contact area	1.4%	3.3%
Right lateral creepage	9%	23%

The results obtained using this model show that maximum angle between the RD and the CE frames is as large as  $10.35^\circ$  while this maximum angle between the LT and the CE frames is  $4.26^\circ$ . Table II shows the average deviation of the RD and LT models from the CE model for different contact parameters. It is observed that the results obtained using the LT frame are in better agreement with those of the CE frame as compared to the ones obtained using the RD frame. This is mainly because both the CE and the LT frames, according to their definition, directly take into account the effect of the track deviation while rail geometry is not used in the definition of the RD frame.

## **2.7. Concluding Remarks**

In wheel/rail creep force formulations, the rolling direction is used with the normal to the contact surfaces to construct the contact frame in which the tangential creep forces are defined. When

Hertz theory is used, an assumption is made that the rolling direction is the same as the direction of one of the axes of the contact ellipse. The rolling direction, however, depends on the motion of the wheel with respect to the rail; while the directions of the axes of the contact ellipse depend only on the geometry of the wheel and rail surfaces and they are determined using the principal directions. Therefore, the rolling direction can be significantly different from the direction of the axes of the contact ellipse in some simulation scenarios. This chapter aimed at studying this fundamental problem and comparing the results obtained using three different contact frames. These frames are the rolling direction (RD) frame, the contact ellipse (CE) frame and the longitudinal tangent (LT) frame. The RD frame is defined by the normal and the axis along the rolling direction, which is defined in this study using the cross product of the angular velocity vector and the position vector of the contact point with respect to the wheel or wheelset body coordinate system. In defining the rolling direction, it is assumed that the rotation of the wheelset or wheel is predominantly pitch rotation. The RD frame is rarely used in the railroad vehicle simulations and can lead to problems in traction and braking scenarios and also in the case of velocity discontinuities due to impact between the vehicle components. The CE frame is defined by the normal vector and one of the axes of the contact ellipse. While none of the axes of the contact ellipse define in general the rolling direction, the CE frame is the one used in many investigations on railroad vehicle systems. Some authors have also employed the LT frame which is independent of Hertz theory and does not involve any motion variables such as the angular velocities. The results obtained using the three contact frames are compared and it was shown that the results obtained using the CE and LT contact frames are in a very good agreement. However, there are simulation scenarios in which the rolling direction as defined by

the angular velocity vector can significantly differ from the axes of the contact ellipse. The numerical results obtained in this study show that while there can be differences in the creepage results of different contact frame models, the contact forces obtained using all these models, in the case of realistic scenarios, are in a good agreement despite the significant orientation difference between different frames. Such a good agreement for the force results can be attributed to the dominant effect of the spin creepage in the lateral force calculations. However, in some extreme cases, there can be differences between the results obtained using different contact frames, in particular the results of the RD model can significantly differ from the results of the CE and LT models. This is can be attributed to the fact that the RD model is different from the two other models in the sense that it does not use rail geometry to define its contact frame.

### 3. MULTIPOINT CONTACT SEARCH ALGORITHM

In railroad vehicle wheel/rail contact analysis, it is crucial to determine the contact forces accurately in order to be able to correctly predict the dynamic response of the vehicles. A first step to achieve this goal is to detect all possible wheel/rail contact points. Using the contact formulations, the contact forces can then be evaluated based on the position of the contact points, the creepages, the wheel and rail geometries and their material properties (Shabana et al., 2008).

Most railroad simulation formulations allow for only one or two wheel/rail contact points. As discussed in Chapter 2, methods such as the constraint contact method or the elastic contact method can be used to find the first point of contact. There are, however, scenarios in which there are multi points of contact between the wheel and the rail. A general contact algorithm capable of finding all possible wheel/rail contact points needs to be developed.

It is, therefore, the objective of this chapter to develop a *multipoint contact search algorithm* that can be applied to general wheel/rail contact problems without any restriction on the number of contact points. This algorithm can be used with either the constraint or elastic contact methods which can be used to determine the first point of contact. For the other contact points, an elastic approach will be used. This is due to the fact that the constraint contact method imposes kinematic constraints that can lead to indeterminate system if such an approach is applied at multiple contact points.

#### 3.1. Contact Formulations

The contact formulations used in this investigation are general formulations that can be applied to multipoint contact problems. The main assumptions used here are as follows:

- All the contacts are non-conformal.

- The first contact point can be determined either by the constraint contact method or the elastic contact method. However, the other points are only determined by the elastic method.
- The location and surface parameters associated with the first point of contact are determined before searching for the other contact points.
- The contact areas are elliptical.
- There is no overlap of contact ellipses associated with different contact points.
- There is no limitation on the number of contact points that can be determined.

Since in the formulations used in this investigation, the wheel and rail geometries are described using surface parameters, the goal of the multipoint contact search algorithm is to find the surface parameters associated with these points. The surface parameters of contact point  $k$  can be written as elements of the vector  $\mathbf{s}^k$  as follows:

$$\mathbf{s}^k = [s_1^{wk} \quad s_2^{wk} \quad s_1^{rk} \quad s_2^{rk}]^T \quad k = 2, \dots, m \quad (3.1)$$

where  $m$  is total number of contact points, and  $s_1^{wk}$  and  $s_2^{wk}$  are the wheel surface parameters while  $s_1^{rk}$  and  $s_2^{rk}$  are the rail surface parameters as described in Chapter 2. Note that in the developed algorithm it is assumed that the surface parameters of the first contact point ( $k = 1$ ) are known.

Using the assumptions of non-conformal contact, five nonlinear algebraic equations must be satisfied at any of the contact points when the constraint contact formulation is used. These equations result from the facts that the global positions of the contact point on the wheel and the rail are the same and the wheel and rail have a common normal at the contact point. When the elastic method is used for the multipoint contact search algorithm, only four nonlinear algebraic

equations need to be used as discussed in Chapter 2. These four algebraic equations are as follows:

$$\begin{bmatrix} \mathbf{t}_1^{rk} \cdot (\mathbf{r}_P^{wk} - \mathbf{r}_P^{rk}) \\ \mathbf{t}_2^{rk} \cdot (\mathbf{r}_P^{wk} - \mathbf{r}_P^{rk}) \\ \mathbf{t}_1^{wk} \cdot \mathbf{n}^{rk} \\ \mathbf{t}_2^{wk} \cdot \mathbf{n}^{rk} \end{bmatrix} = \mathbf{0} \quad k = 2, \dots, m \quad (3.2)$$

The four surface parameters at the contact points can be determined by solving the nonlinear algebraic equations of Eq. 3.2 using a Newton-Raphson scheme. To this end, the following system of algebraic equations is iteratively solved:

$$\begin{bmatrix} \mathbf{t}_1^r \cdot \mathbf{t}_1^w & \mathbf{t}_1^r \cdot \mathbf{t}_2^w & \mathbf{t}_{1,s_1^r}^r \cdot \mathbf{r}^{wr} - \mathbf{t}_1^r \cdot \mathbf{t}_1^r & \mathbf{t}_{1,s_2^r}^r \cdot \mathbf{r}^{wr} - \mathbf{t}_1^r \cdot \mathbf{t}_2^r \\ \mathbf{t}_2^r \cdot \mathbf{t}_1^w & \mathbf{t}_2^r \cdot \mathbf{t}_2^w & \mathbf{t}_{2,s_1^r}^r \cdot \mathbf{r}^{wr} - \mathbf{t}_2^r \cdot \mathbf{t}_1^r & \mathbf{t}_{2,s_2^r}^r \cdot \mathbf{r}^{wr} - \mathbf{t}_2^r \cdot \mathbf{t}_2^r \\ \mathbf{t}_{1,s_1^w}^w \cdot \mathbf{n}^r & \mathbf{t}_{1,s_2^w}^w \cdot \mathbf{n}^r & \mathbf{t}_{1,s_1^r}^w \cdot \mathbf{n}^r & \mathbf{t}_{1,s_2^r}^w \cdot \mathbf{n}^r \\ \mathbf{t}_{2,s_1^w}^w \cdot \mathbf{n}^r & \mathbf{t}_{2,s_2^w}^w \cdot \mathbf{n}^r & \mathbf{t}_{2,s_1^r}^w \cdot \mathbf{n}^r & \mathbf{t}_{2,s_2^r}^w \cdot \mathbf{n}^r \end{bmatrix} \begin{bmatrix} \Delta s_1^w \\ \Delta s_2^w \\ \Delta s_1^r \\ \Delta s_2^r \end{bmatrix} = - \begin{bmatrix} \mathbf{t}_1^r \cdot \mathbf{r}^{wr} \\ \mathbf{t}_2^r \cdot \mathbf{r}^{wr} \\ \mathbf{t}_1^w \cdot \mathbf{n}^r \\ \mathbf{t}_2^w \cdot \mathbf{n}^r \end{bmatrix} \quad (3.3)$$

The wheel/rail penetration at the contact point  $k$  is

$$\delta^k = \mathbf{n}^{rk} \cdot (\mathbf{r}_P^{wk} - \mathbf{r}_P^{rk}) \quad k = 2, \dots, m \quad (3.4)$$

and the associated compliant normal force at this contact point can be written as follows (Shabana et al 2005):

$$F_n^k = F_h^k + F_d^k = -K_h^k (\delta^k)^{\frac{3}{2}} - C^k \dot{\delta}^k |\delta^k| \quad k = 2, \dots, m \quad (3.5)$$

where  $K_h^k$  is the Hertzian constant,  $C^k$  is the damping coefficient, and  $\dot{\delta}^k$  is the time rate of the penetration.

It should be noted again that the algorithm is developed such that the first contact point can be determined either by the elastic method or the constraint method. However, one of the conclusions made in this chapter is that the constraint contact approach can be used only for the

first contact point. The main differences between the constraint and elastic methods when multipoint contact point scenarios are considered are as follows:

- In the constraint method, the first contact point is determined using a formulation different from the one used for other contact points which are determined using the elastic method as previously mentioned.
- The constraint method, unlike the elastic method, allows no penetration or separation at the first contact point. Due to this fact, if the contact constraints are imposed at one location, unrealistic results can be obtained if the algorithm does not allow for switching the constraint contact location in the case of multipoint contact search.
- In multipoint contact problems, in general, the penetration at one point can significantly affect the kinematics and forces at other contact points. In the constraint method, the zero penetration at the first contact point can influence the penetration at other contact points as will be demonstrated in the second example of this chapter.

### **3.2. Search Algorithm**

The multipoint contact search algorithm developed in this chapter employs the following steps:

1. At the beginning of the simulation, the wheel and rail profiles are discretized to a selected number of segments; the profile surface parameters ( $s_1^w$  and  $s_2^r$ ) of at the nodes that define these segments are stored. These nodal points are used to determine *potential points of contact* during the simulation. It is assumed that before the search

starts at any instant of time during the simulation, the first contact point is already determined for that specific time.

2. During the simulation and after the location of the first contact point is determined at a given time point, the search algorithm uses the saved profile surface parameters (Step 1) to calculate the positions of the nodal points.
3. The position of these points are calculated using the saved profile surface parameters and the other two surface parameters  $s_2^w$  and  $s_1^r$ . These two latter parameters change during the simulation while the profile surface parameters at the nodal points do not change. Since the surface parameters of the first contact point is known, its angular surface parameter  $s_2^{w1}$  can be used for other potential contact points. Similarly, the rail longitudinal surface parameter can be calculated using that of the first contact point  $s_1^{r1}$  by making the adjustment of  $\Delta s_1^r = (s_2^r - s_2^{r1}) \tan \phi$ , where  $\phi$  is the yaw rotation of the wheel with respect to the track frame. Knowing the four surface parameters, the global position vector of the nodal points can be calculated. The points close to the first contact point (based on a given tolerance) are eliminated in order to improve the computational efficiency.
4. The distances between the points of the wheel and those of the rail are calculated and the pair of points that are close to within a specific tolerance are selected as potential points of contact between the wheel and the rail.
5. Once all the potential points of contact are determined at given time point, the surface parameters associated with each point are used as the initial guess for an iterative Newton-Raphson method that employs Eq. 3.3. The converged Newton-Raphson

solutions are checked using the penetration condition in order to determine the pairs of contact points. Converged solutions that do not satisfy the penetration condition are not considered.

6. The distances between all the contact points, including the first contact point, are calculated. If the distance between two contact points is larger than a specified tolerance, the two contact points are considered as new contact points. Otherwise, the contact point with the larger penetration is only considered, and the second point is ignored.
7. If the algorithm does not find a second point of contact, another search begins to find possible lead and lag contacts, which can be encountered in the case of large yaw rotations. To this end, one can use  $\Delta s_1^r = R^w \phi \alpha$  and  $\Delta s_2^w = \arctan(\phi \tan \alpha)$  where  $R^w$  is wheel radius and  $\alpha$  is the contact angle for the flange contact (Escalona et al., 2003), to determine a point on the flange. If there is a wheel/rail penetration at this point, a search is performed in the neighborhood of this point by using positive and negative small increments based the above mentioned equations to find a point that leads to penetration. The surface parameters of this potential contact point are used in the Newton-Raphson iterative algorithm as an initial guess. The resulting contact point defined by the converged solution is checked to make sure that it is not in the vicinity of one of the previously determined contact points. Once all the contact points are identified and the associated penetrations are calculated using Eq. 3.4, the normal contact force can be determined using Eq. 3.5. The creepages at each of the contact points are also calculated. The creepages, the normal contact forces, the wheel and

rail material properties, and contact ellipse dimensions are used to calculate the tangential creep forces and spin moment. The normal and creep contact forces are used to determine generalized contact forces associated with the generalized coordinates of the wheel and rail.

Because of the generality of this search algorithm, there is no limitation on the number of contact points that can be found.

### **3.3. Numerical Results**

In this section, the numerical results obtained using the proposed algorithm are presented for two simulation scenarios. The simulation scenarios are designed to have multiple wheel/rail contacts. A comparison between the results obtained using the elastic and constraint contact methods in the case of multi contact point scenarios is also presented in this section.

#### **3.3.1. Single Truck Model Subjected to Lateral Forces**

In this example, a single truck model negotiating a tangent track is considered. The model, as shown in Fig. 23, consists of a frame, two wheelsets, two equalizers, and the rails. The bodies are connected by bushings and bearings. For this simulation, the elastic method is used for the first point of contact.

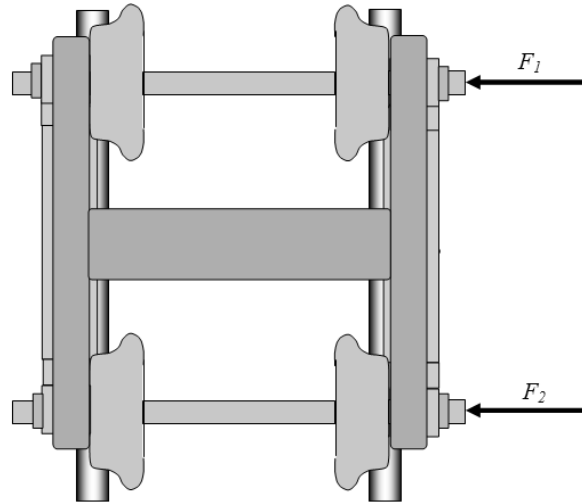


Figure 23. Single truck model subjected to two lateral forces

As shown in Fig. 23, two lateral forces  $F_1$  and  $F_2$  are, respectively, applied on the front and rear wheelsets. The magnitudes of the forces are the same and they are assumed to be functions of time according to the following equation:

$$F_1 = F_2 = \begin{cases} 0 & t < 8 \text{ or } t > 11 \\ 6000(t-8) & 8 \leq t \leq 11 \end{cases} \quad (3.6)$$

The application of these forces causes the truck to move to the left, which ultimately, results in multiple contact points for the left wheels of the truck and the left rail due to the shape of their profiles that are shown in Figs. 24 and 25.

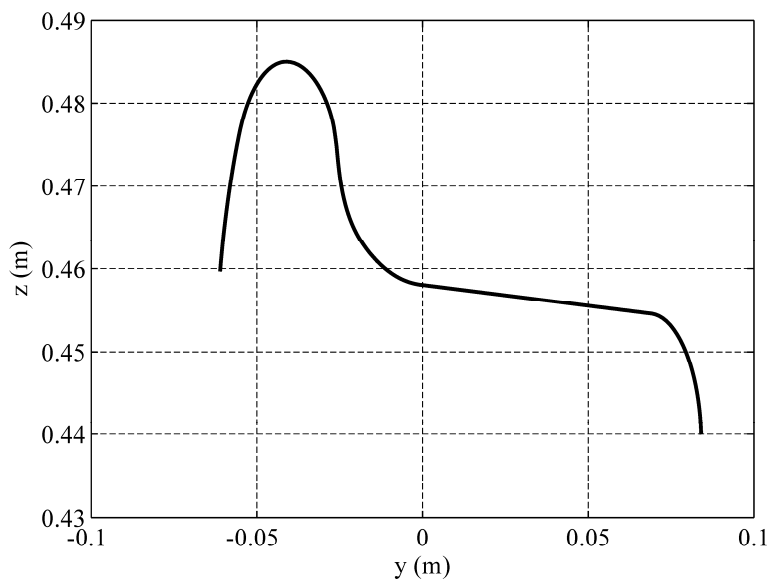


Figure 24. The wheel profile

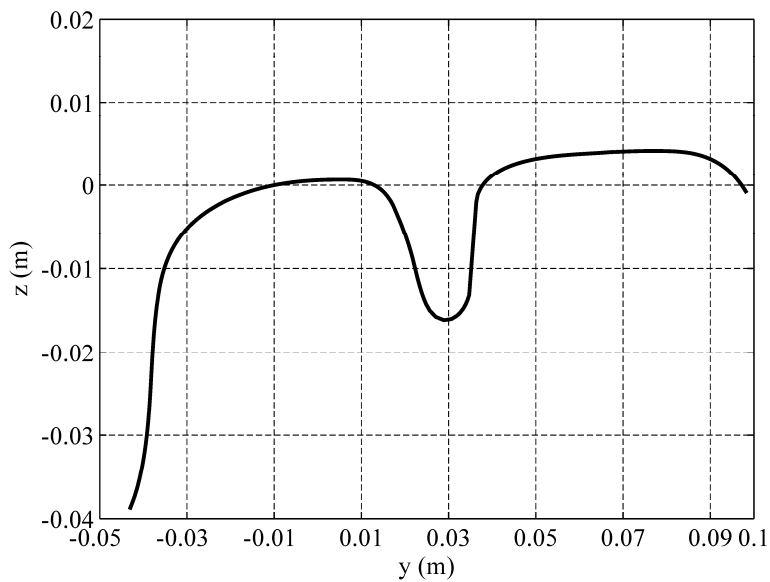


Figure 25. The rail profile

The shapes of the profiles allow for three wheel/rail contact points. The algorithm should be able to capture the one, two, and three contact point scenarios. The approximate locations of the contact points are depicted in Fig. 26.

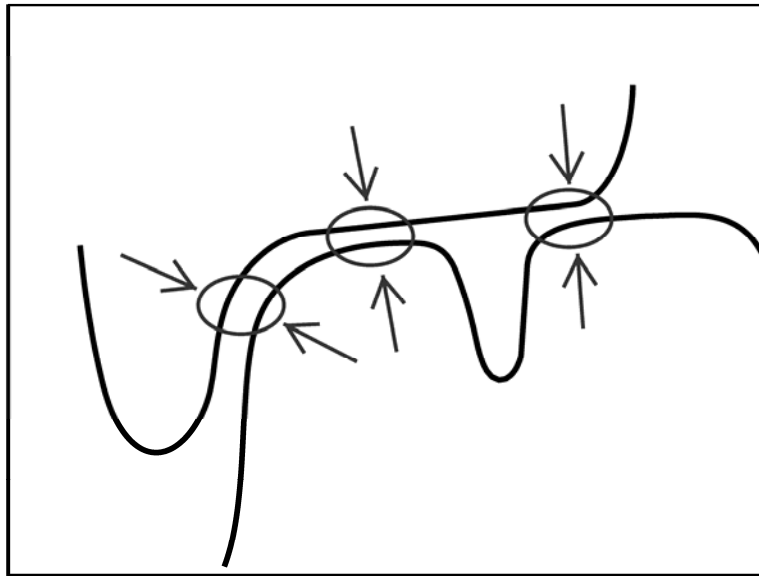


Figure 26. The approximate locations of contact points

The results of this simulation are shown in Figs. 27-32. Figures 27 and 28 show the Y-coordinate of the contact points for the front and rear contacts, respectively. Also, in Figs. 29 and 30, the rail profile surface parameters of these contact points are shown. By examining the wheel and rail profile shapes shown in Figs. 24 and 25, it is clear that the proposed algorithm successfully found the points at the expected locations. The corresponding normal forces for these contact points are shown in Figs. 31 and 32.

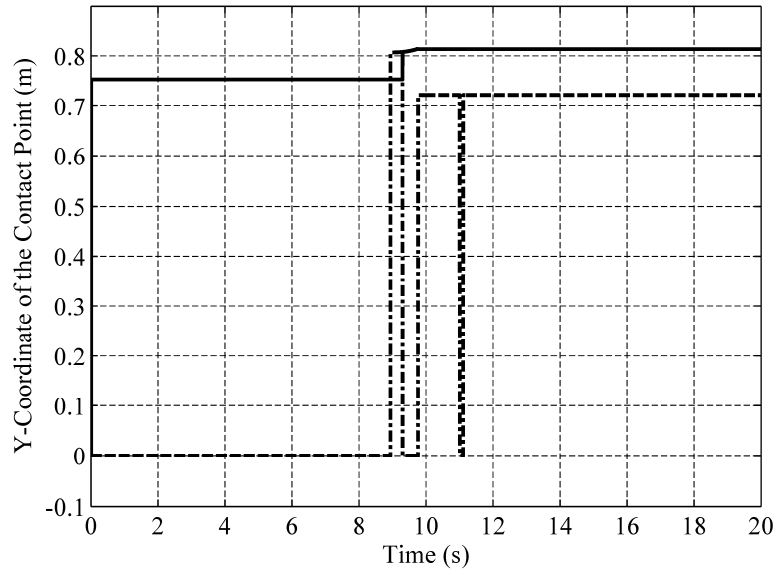


Figure 27. Y-coordinate of the left front contact  
 (—— First contact point, - . . . - Second contact point)

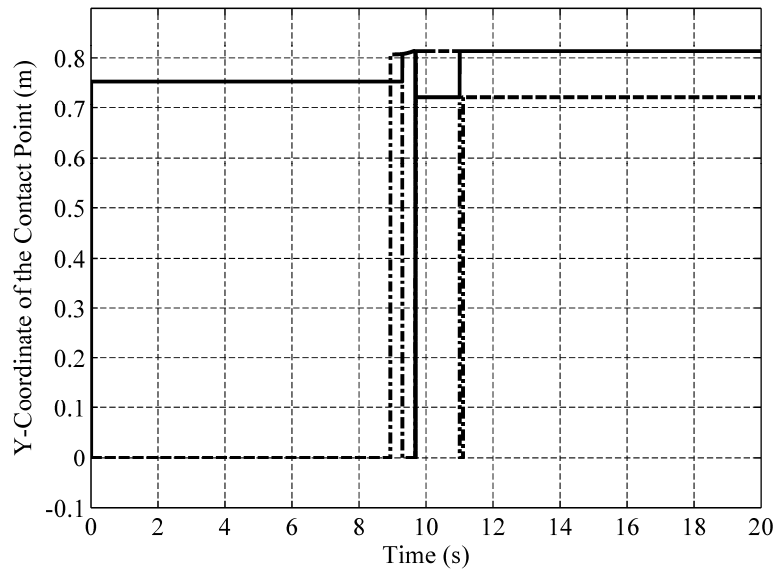


Figure 28. Y-coordinate of the left rear contact  
 (—— First contact point, - . . . - Second contact point)

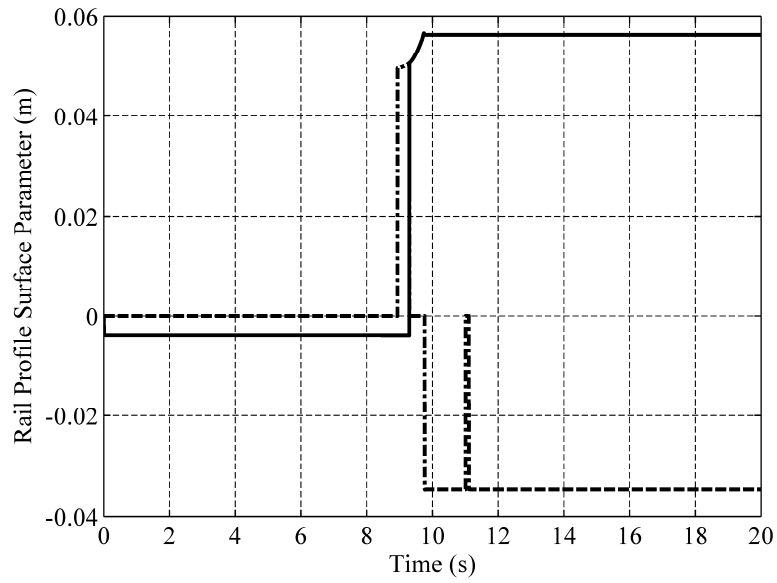


Figure 29. Rail profile surface parameters of the left front contact  
 (—— First contact point, - - - Second contact point)

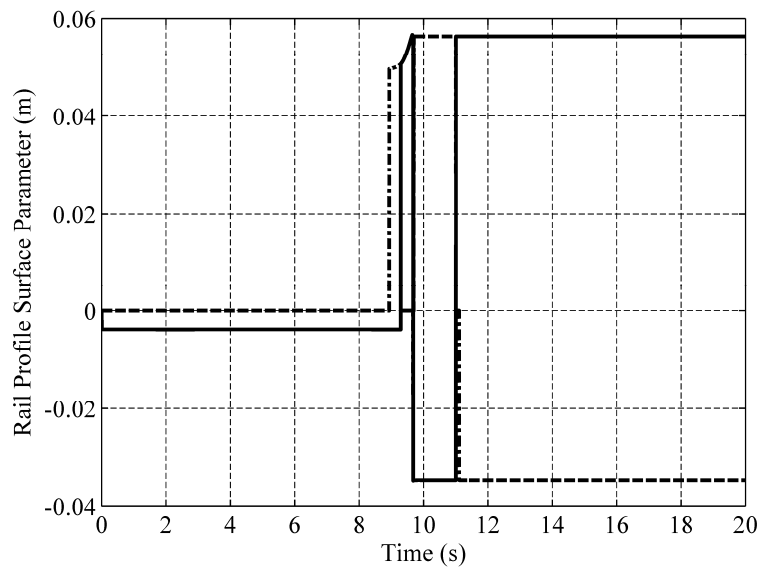


Figure 30. Rail profile surface parameters of the left rear contact  
 (—— First contact point, - - - Second contact point)

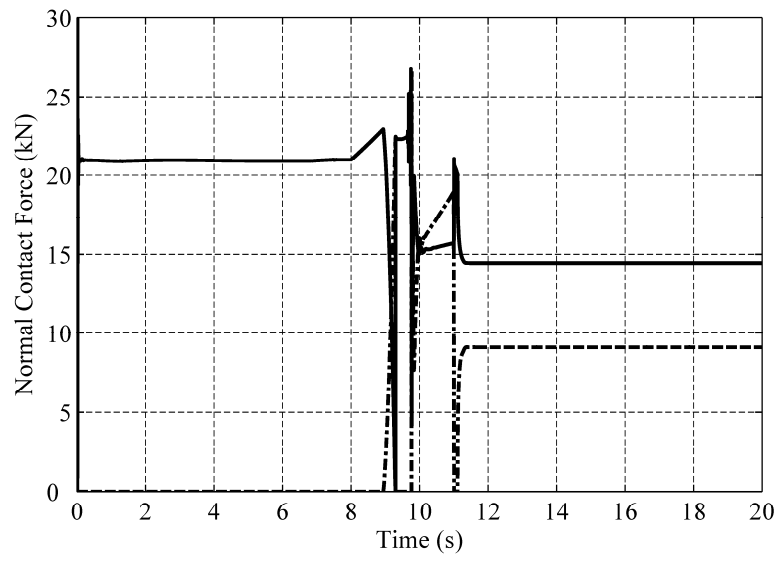


Figure 31. Normal force of the left front contact  
(—— First contact point, - - - Second contact point)

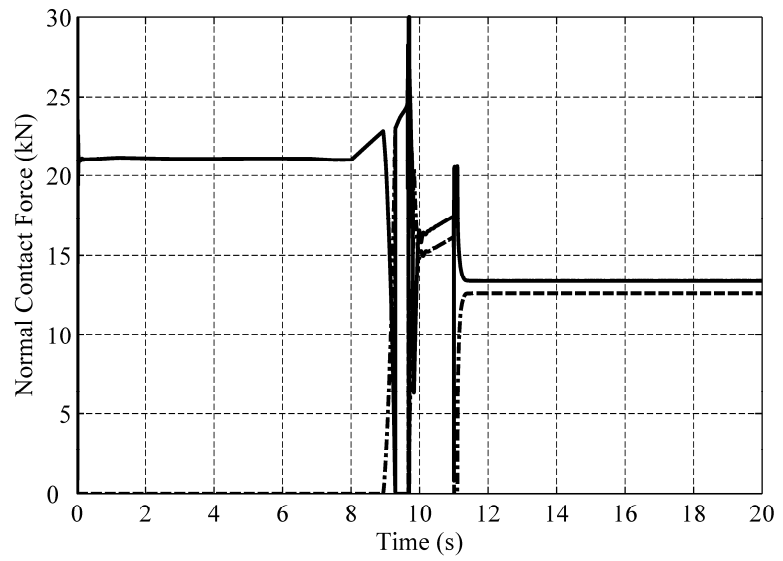


Figure 32. Normal force of the left rear contact  
(—— First contact point, - - - Second contact point)

### 3.3.2. Suspended Wheelset Model on a Curve Track

In this example, the multipoint contact search algorithm is used in the simulation of a suspended wheelset on a curved track. The model, as shown in Fig. 33, consists of three bodies including a frame, a wheelset, and rails. The frame and wheelset are connected by linear springs and dampers while the frame is constrained to move along the track with a forward velocity of 17.88 m/s (40 mph).

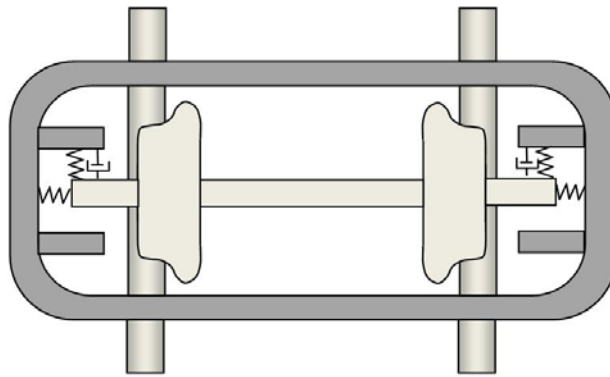


Figure 33 Suspended wheelset model

In the previous example, the external lateral forces caused wheel/rail contact at multiple points. In this example, however, it is the track geometry, which leads to three contact points. The curved track used for this simulation is shown in Fig. 34. The right wheel and right rail, which are, respectively, shown in Figs. 35 and 36, have specific shapes that can result in three contact points when the vehicle moves on the track.

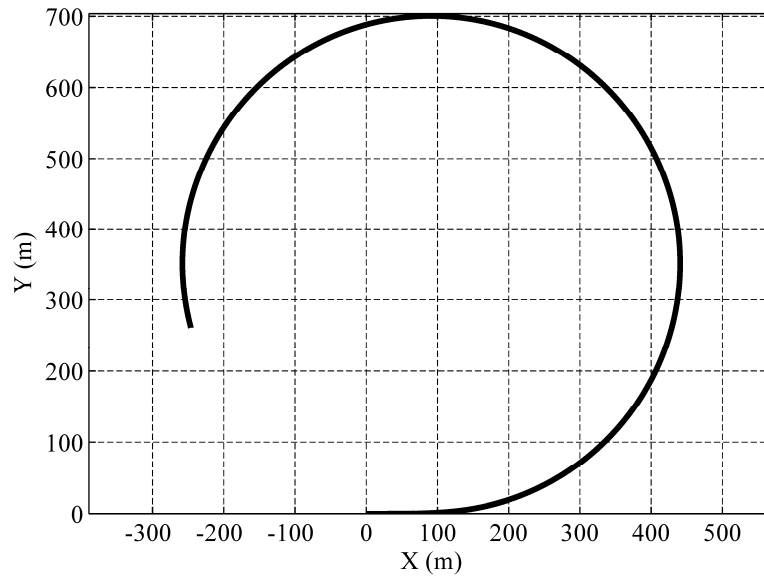


Figure 34. The top view of the track used for the suspended wheelset model

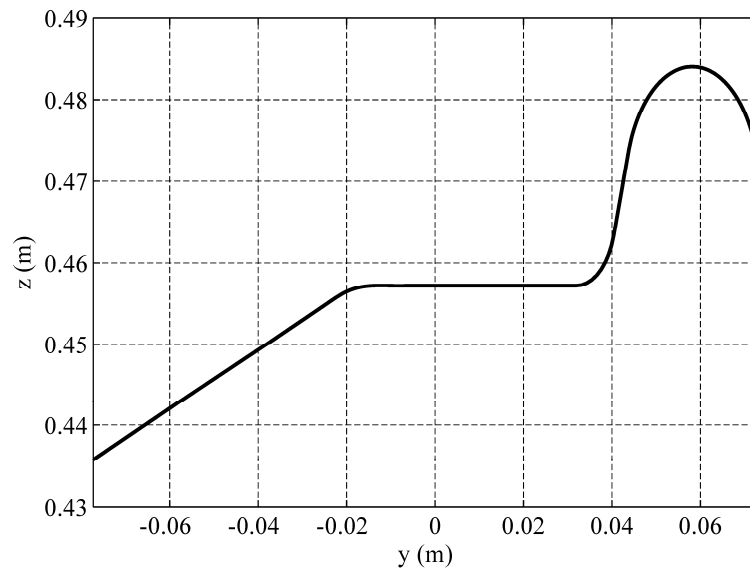


Figure 35. The wheel profile

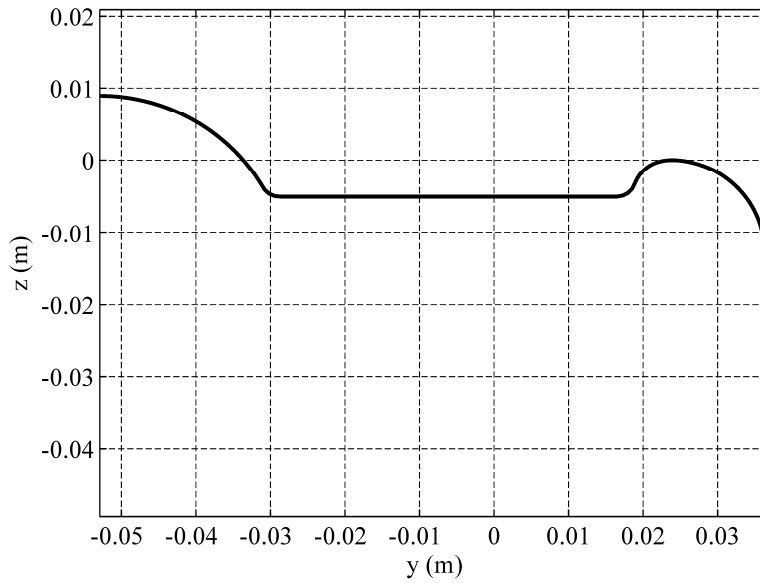


Figure 36. The rail profile

Similar to the previous example, the elastic method is used for the first point of contact. However, after presenting the results of this simulation, the simulation will be carried out again using the constraint method in order to compare the results obtained using these two methods.

The results show that the search algorithm successfully finds all the expected contact points. Figure 37 shows the profile surface parameters of the right rail while the normal contact forces associated with these points are shown in Fig. 38.

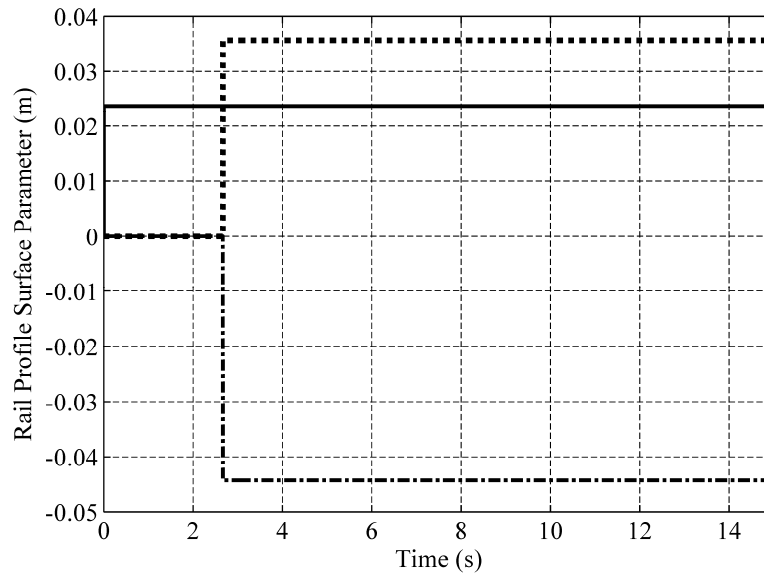


Figure 37. Rail profile surface parameters of the right contact  
 (—— First contact point, - - - Second contact point, ..... Third contact point)

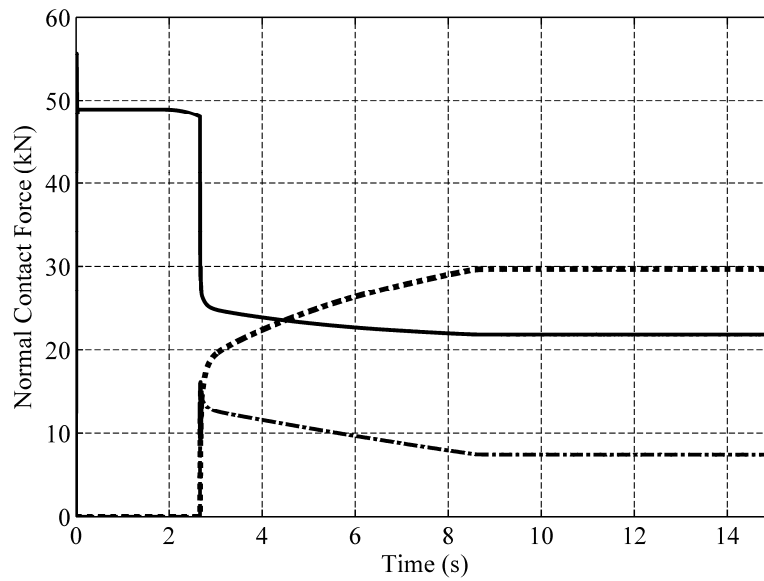


Figure 38. Normal force of the right contact  
 (—— First contact point, - - - Second contact point, ..... Third contact point)

If the constraint contact method is used for this simulation, the search algorithm again determines the same three contact points. The normal contact forces, however, are much different from those of the elastic contact method as shown in Fig. 39. The results demonstrate that the change of the contact formulations used for the first contact point can considerably affect the force distribution among the other contact points.

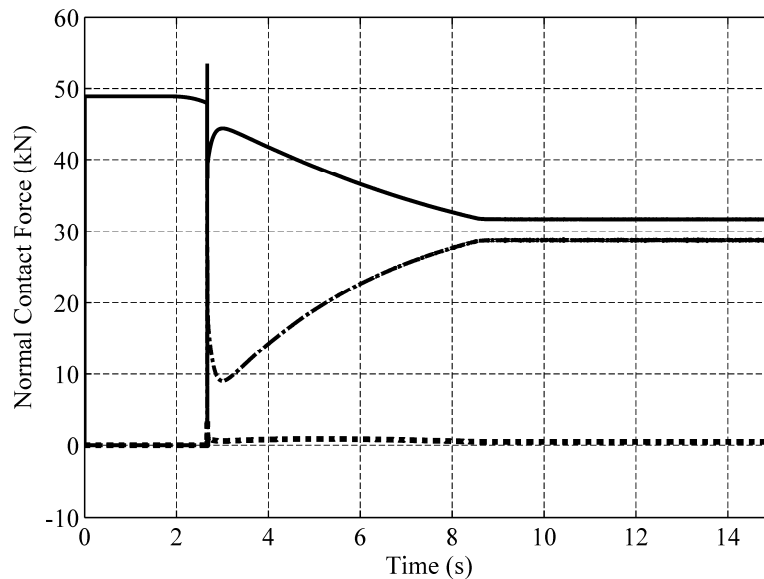


Figure 39. Normal force of the right contact (constraint contact method)  
 (—— First contact point, - - - Second contact point, ..... Third contact point)

### 3.4. Concluding Remarks

A multipoint contact search algorithm was developed in this chapter. The developed algorithm imposes no limitation on the method used to find the first point of contact or on the number of contact points. The algorithm is capable of finding the contact points with a good precision because of the use of an iterative Newton-Raphson algorithm. The developed algorithm successfully finds multiple wheel/rail contact points. This was demonstrated by two examples in

this chapter. A comparison between the results obtained using the constraint and elastic contact methods in the case of multipoint contact scenario was made and the differences between these methods in predicting the contact force distributions were discussed. It was demonstrated by an example that the change of the contact method used for predicting the first contact point in the case of multipoint contact scenarios can considerably affect the normal force distribution among the contact points.

#### 4. AIR BRAKE FORCE MODEL

Most trains in North America use pneumatic brakes or air brakes. For the most part, the automatic air brake system of a freight train consists of a *locomotive control unit*, a *car control unit* located in each car, and a *pipe* connecting all these elements as shown in Fig. 40.

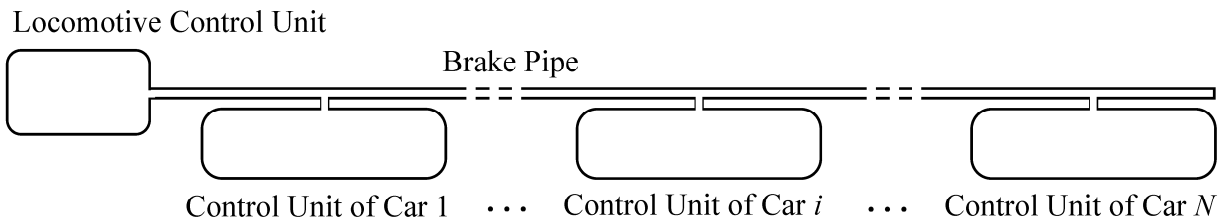


Figure 40. Main air brake components

This pipe that both transfers airflow and brake signals will be referred to as *brake pipe*, while the locomotive automatic brake valve will be called *automatic brake valve* in this chapter. The function of the locomotive automatic brake valve is to control the air pressure in the brake pipe for *on car* compressed air storage as well as brake application and release of all cars. Such a control action provides the pressure control signal that propagates along the brake pipe serially reaching one car after another. In addition to the brake pipe pressure, the controlling locomotive equalizing and emergency reservoir pressures are also controlled. By varying the position of the automatic brake valve handle, different scenarios and states of the brake system can be achieved. These states include the *brake release mode* in which the pressure in the brake pipe is increased in order to release the brakes and recharge the CCU compressed air storage reservoirs, the *service mode* in which the pressure must be reduced in order to apply the brakes with a pressure reduction (at a service rate) that is determined by the handle position with respect to the full

service position, and the *emergency mode* that allows the brake pipe pressure to be quickly reduced by venting the brake pipe air to the atmosphere (The latter two, service and emergency modes, are referred to as the *brake application mode*). Therefore, an accurate air brake model must be able to predict the response of the air flow in the brake pipe to the changes made in the locomotive automatic brake valve handle position. The 26C valve also has the independent brake valve function that is not modeled in this study.

The objective of this chapter is to integrate a dynamic air brake model with efficient nonlinear train longitudinal force algorithms based on trajectory coordinate formulations. The proposed air brake force model used in this chapter employs the continuity and momentum equations and accounts for the effect of the air flow in long train pipes as well as the effect of leakage and branch pipe flows. This model can be effectively used to study the dynamic behavior of the air flow in the train pipe and its effect on the longitudinal train forces during brake application and release. The continuity and momentum equations are simplified by using the assumptions of one dimensional isothermal flow, leading to two coupled air velocity/pressure partial differential equations that depend on time and the longitudinal coordinate of the brake pipe. The resulting partial differential equations are converted to a set of air brake first order ordinary differential equations using the finite element discretization. These first order ordinary differential equations are solved simultaneously with the train second order nonlinear dynamic differential equations of motion that are based on the trajectory coordinates. In this chapter, the train car dynamics is defined using a body track coordinate system that follows the car motion. The translation and orientation of this coordinate system are defined in terms of one geometric trajectory parameter that describes the distance travelled by the car. The configuration of the car

with respect to its track coordinate system is described using two translation coordinates and three Euler angles (Shabana et al., 2008). The nonlinear trajectory coordinate formulation used in this study allows for the use of arbitrary track geometry. The operation of the brake system, including brake application and release, is controlled by the locomotive automatic brake valve that defines the input to the air brake system during the dynamic simulation. A simplified valve model is also proposed in order to reduce the simulation computational time. The procedure for coupling the brake pipe air flow, locomotive automatic brake valve, CCU, and train equations is established and used in the simulation of the nonlinear dynamics of long trains.

#### **4.1. Air Flow Equations**

In this section, the basic continuum mechanics equations used in this chapter to study the air flow dynamics in train brake pipes are presented. These equations include the momentum, continuity, and constitutive equations. In the following section, the general three-dimensional equations presented in this section are simplified to the case of one dimensional isothermal flow. It should be noted that if the process takes place rapidly, the adiabatic process assumption is more realistic than the isothermal process. Nonetheless, the actual process is neither of these processes. In fact, the actual process is polytropic. However, in this investigation, similar to some previous studies, the isothermal flow assumption is used (Abdol-Hamid, 1986).

##### **4.1.1. Continuity Equation**

The general continuity equation for a fluid can be written as (John and Keith, 2006; Shabana, 2008; White, 2008)

$$\int_V \frac{\partial \rho}{\partial t} dV + \int_S \rho \mathbf{v} \cdot \mathbf{n} dS = 0 \quad (4.1)$$

In this equation,  $V$  is the volume which is assumed to remain constant for the brake pipe, and therefore, no distinction is made between the volumes in the reference and current configurations;  $S$  is the surface area,  $\rho$  is the mass density,  $\mathbf{v}$  is the velocity vector, and  $\mathbf{n}$  is the normal to the surface. Using the divergence theorem, the continuity equation can be written as

$$\frac{\partial \rho}{\partial t} + \nabla \cdot (\rho \mathbf{v}) = 0 \quad (4.2)$$

In this equation,  $\nabla$  is the divergence operator. Since air flow is considered in this study, the density  $\rho$  cannot be treated as a constant, and therefore, the assumption of incompressibility is not used in this study.

#### 4.1.2. Momentum Equation

The momentum equation or the partial differential equation of equilibrium can be written in the following form (Shabana, 2008):

$$\int_V \rho \mathbf{a} dv = \int_S \boldsymbol{\sigma} \mathbf{n} ds + \int_V \mathbf{f}_b dv \quad (4.3)$$

In this equation,  $\mathbf{a}$  is the acceleration vector,  $\boldsymbol{\sigma}$  is the symmetric Cauchy stress tensor,  $s$  and  $v$  are, respectively, the area and volume in the current configuration, and  $\mathbf{f}_b$  is the vector of body forces per unit volume. Applying the divergence theorem, and assuming that  $v = V$  for the brake pipe, the preceding equation leads to

$$\int_V \rho \mathbf{a} dV = \int_V (\nabla \cdot \boldsymbol{\sigma})^T dV + \int_V \mathbf{f}_b dV \quad (4.4)$$

This equation can also be written in the following differential form:

$$\rho \mathbf{a} = (\nabla \boldsymbol{\sigma})^T + \mathbf{f}_b \quad (4.5)$$

The first term of this equation, which represents the inertia force, can be rewritten in a different form, which is more convenient to use when dealing with compressible fluids. Multiplying the continuity equation of Eq. 4.2 by the velocity vector  $\mathbf{v}$ , one obtains

$$\frac{\partial \rho}{\partial t} \mathbf{v} + \nabla(\rho \mathbf{v}) \mathbf{v} = \mathbf{0} \quad (4.6)$$

Using the expression for the total derivative of the velocity vector  $\mathbf{v}$ , the inertia term  $\rho \mathbf{a}$  can be written as

$$\rho \mathbf{a} = \rho \frac{d\mathbf{v}}{dt} = \rho \frac{\partial \mathbf{v}}{\partial t} + \rho(\nabla \mathbf{v}) \mathbf{v} \quad (4.7)$$

Substituting Eq. 4.7 into Eq. 4.5 and adding Eq. 4.6, one obtains

$$\rho \frac{\partial \mathbf{v}}{\partial t} + \rho(\nabla \mathbf{v}) \mathbf{v} + \frac{\partial \rho}{\partial t} \mathbf{v} + \nabla(\rho \mathbf{v}) \mathbf{v} = (\nabla \boldsymbol{\sigma})^T + \mathbf{f}_b \quad (4.8)$$

This equation can be written as

$$\frac{\partial(\rho \mathbf{v})}{\partial t} + (\rho(\nabla \mathbf{v}) + \nabla(\rho \mathbf{v})) \mathbf{v} = (\nabla \boldsymbol{\sigma})^T + \mathbf{f}_b \quad (4.9)$$

This equation is an alternate form of the momentum equation of Eq. 4.5.

### 4.1.3. Fluid Constitutive Equation

In the case of isotropic fluids, the constitutive equations that differentiate one fluid from another and define the fluid characteristics can be written as

$$\boldsymbol{\sigma} = \{-p(\rho, T) + \lambda(\rho, T)\text{tr}(\mathbf{D})\}\mathbf{I} + 2\mu(\rho, T)\mathbf{D} \quad (4.10)$$

where  $p$  is the hydrostatic pressure,  $\rho$  is the mass density,  $T$  is the temperature,  $\mathbf{D}$  is the rate of deformation tensor, and  $\lambda$  and  $\mu$  are viscosity coefficients that depend on the fluid density and temperature.

#### 4.1.4. Navier-Stokes Equations

In order to obtain the fluid equations of motion, the constitutive equations of Eq. 4.10 are substituted into the partial differential equations of equilibrium of Eq. 4.9. This leads to

$$\frac{\partial(\rho\mathbf{v})}{\partial t} + (\rho(\nabla\mathbf{v}) + \nabla(\rho\mathbf{v}))\mathbf{v} = \{-\nabla(p\mathbf{I}) + \nabla(\lambda\text{tr}(\mathbf{D})\mathbf{I}) + \nabla(2\mu\mathbf{D})\}^T + \mathbf{f}_b \quad (4.11)$$

This equation represents the general three-dimensional partial differential equations of motion for isotropic fluids. If the fluid is assumed to be Newtonian, that is the shear stress is proportional to the rate of the shear strain, the preceding equation reduces to

$$\frac{\partial(\rho\mathbf{v})}{\partial t} + (\rho(\nabla\mathbf{v}) + \nabla(\rho\mathbf{v}))\mathbf{v} = \{-\nabla(p\mathbf{I}) + \lambda\nabla(\text{tr}(\mathbf{D})\mathbf{I}) + 2\mu\nabla(\mathbf{D})\}^T + \mathbf{f}_b \quad (4.12)$$

Equation 4.11 governs the motion of general isotropic fluid, while Eq. 4.12 governs the motion in the special case of Newtonian fluid.

## 4.2. One-dimensional Model

The assumption of one-dimensional air flow used in this study implies that the flow, at any cross section, has only one direction along the longitudinal axis of the pipe, that is, the velocity components in the other directions are not considered. Furthermore, the magnitude of the flow velocity is assumed to be uniform at any cross section. Consequently, shear stresses are

neglected, and as a result, the off-diagonal elements of the Cauchy stress tensor are assumed to be zero.

In the case of one dimensional air flow, the continuity equation of Eq. 4.2 reduces to

$$\frac{\partial \rho}{\partial t} + \frac{\partial(\rho u)}{\partial x} + L = 0 \quad (4.13)$$

In this equation,  $x$  is the longitudinal spatial pipe coordinate,  $L$  is the air leakage, and  $u$  is the velocity component along the longitudinal  $x$  coordinate of the brake pipe. Note that the preceding equation is a partial differential equation that depends on both time  $t$  and the spatial coordinate  $x$ . The effect of air flow through the pipe branches can also be introduced systematically to the continuity equation in order to account for the mass flow rate. In the case of multiple branches connected to the main air pipe, a term can be added to the continuity equation as discussed in the previous chapter where the car control unit model is developed.

In the case of one dimensional flow, the Navier-Stokes equation of Eq. 4.12 becomes

$$\frac{\partial(\rho u)}{\partial t} + \frac{\partial(\rho u^2)}{\partial x} = -\frac{\partial p}{\partial x} + (\lambda + 2\mu) \frac{\partial^2 u}{\partial x^2} + f_b \quad (4.14)$$

If the fluid is assumed to be *inviscid*, that is, the effect of shear is neglected, the second term on the right hand side of the preceding equation can be neglected, leading to

$$\frac{\partial(\rho u)}{\partial t} + \frac{\partial(\rho u^2)}{\partial x} = -\frac{\partial p}{\partial x} + f_b \quad (4.15)$$

Using the assumption of isothermal flow, one has the following relationship (White, 2008):

$$\frac{p}{\rho} = R_g \Theta \quad (4.16)$$

In this equation,  $R_g$  is the gas constant which has units  $J/(Kg^\circ K)$ , and  $\Theta$  is the local temperature ( $^\circ K$ ). The relationship of Eq. 4.16 can be used to eliminate the air density  $\rho$  from the continuity and momentum equations leading to the following system of pressure/velocity coupled equations:

$$\left. \begin{aligned} \frac{\partial p}{\partial t} + \frac{\partial(pu)}{\partial x} + \gamma_t L &= 0 \\ \frac{\partial(pu)}{\partial t} + \frac{\partial(pu^2)}{\partial x} + \gamma_t \frac{\partial p}{\partial x} &= \gamma_t f_b \end{aligned} \right\} \quad (4.17)$$

In this equation,  $\gamma_t = R_g \Theta$ . Given the boundary and initial conditions, the preceding system of coupled partial differential equations can be solved for the pressure and velocity distributions using numerical methods as discussed in the following section.

### **4.3. Finite Element Formulation**

In this study, a finite element procedure is used to transform the partial differential equations of Eq. 4.17 to a set of coupled first order ordinary differential equations. These ordinary differential equations can be solved using the method of numerical integration to determine the pressure and velocity for different braking scenarios. Let  $q = pu$  be a new variable. Using this definition, Eq. 4.17 can be rewritten as

$$\left. \begin{aligned} \frac{\partial p}{\partial t} + \frac{\partial q}{\partial x} &= -\gamma_t L \\ \frac{\partial q}{\partial t} + \frac{\partial(qu)}{\partial x} + \gamma_t \frac{\partial p}{\partial x} &= \gamma_t f_b \end{aligned} \right\} \quad (4.18)$$

In the finite element analysis, the brake pipe is assumed to consist of  $m$  finite elements. The domain of the element is defined by the spatial coordinate  $x = x^e, 0 < x^e < l^e$ , where  $l^e$  is the length of the finite element. Over the domain of the finite element, the variables  $p$  and  $q$  are interpolated using the following field:

$$p^e(x, t) = \mathbf{S}_p^e \mathbf{p}^e, \quad q^e(x, t) = \mathbf{S}_q^e \mathbf{q}^e, \quad e = 1, 2, \dots, m \quad (4.19)$$

where  $\mathbf{S}_p^e$  and  $\mathbf{S}_q^e$  are appropriate shape functions, and  $\mathbf{p}^e$  and  $\mathbf{q}^e$  are the vectors of nodal coordinates. Multiplying the first equation in Eq. 4.18 by the virtual change  $\delta p^e$  and the second equation by the virtual change  $\delta q^e$ , integrating over the volume, using the relationship  $dV^e = A^e dx^e$ , where  $A^e$  is the cross section area; and using Eq. 4.19; one obtains the following system of first order ordinary differential equations for the finite element  $e$ :

$$\mathbf{M}^e \dot{\mathbf{e}}^e = \mathbf{Q}^e, \quad e = 1, 2, \dots, m \quad (4.20)$$

In this equation,

$$\mathbf{e}^e = \begin{bmatrix} \mathbf{p}^e \\ \mathbf{q}^e \end{bmatrix}, \quad \mathbf{Q}^e = \begin{bmatrix} \mathbf{Q}_p^e \\ \mathbf{Q}_q^e \end{bmatrix}, \quad \mathbf{M}^e = \begin{bmatrix} \mathbf{M}_{pp}^e & \mathbf{M}_{pq}^e \\ \mathbf{M}_{qp}^e & \mathbf{M}_{qq}^e \end{bmatrix} \quad (4.21)$$

where

$$\left. \begin{aligned} \mathbf{M}_{pp}^e &= \int_0^{l^e} A^e \mathbf{S}_p^{eT} \mathbf{S}_p^e dx, & \mathbf{M}_{pq}^e &= \mathbf{M}_{qp}^e = \mathbf{0}, & \mathbf{M}_{qq}^e &= \int_0^{l^e} A^e \mathbf{S}_q^{eT} \mathbf{S}_q^e dx, \\ \mathbf{Q}_p^e &= - \left( \left( \int_0^{l^e} A^e \mathbf{S}_p^{eT} \frac{\partial \mathbf{S}_q^e}{\partial x} dx \right) \mathbf{q}^e + \int_0^{l^e} A^e \mathbf{S}_p^{eT} dx \gamma_t^e L^e \right), \\ \mathbf{Q}_q^e &= - \left( \int_0^{l^e} A^e \mathbf{S}_q^{eT} \frac{\partial \mathbf{S}_q^e}{\partial x} u^e dx \right) \mathbf{q}^e - \left( \int_0^{l^e} A^e \mathbf{S}_q^{eT} \mathbf{S}_q^e \frac{\partial u^e}{\partial x} dx \right) \mathbf{q}^e \\ &\quad - \gamma_t \left( \int_0^{l^e} A^e \mathbf{S}_q^{eT} \frac{\partial \mathbf{S}_p^e}{\partial x} dx \right) \mathbf{p}^e + \int_0^{l^e} A^e \mathbf{S}_q^{eT} dx \gamma_t f_b \end{aligned} \right\} \quad (4.22)$$

The finite element equations of Eq. 4.20 can be assembled using a standard finite element assembly procedure. This leads to the first order ordinary differential equations of the brake pipe system which can be written in the following matrix form:

$$\mathbf{M}\dot{\mathbf{e}} = \mathbf{Q} \quad (4.23)$$

In this equation,  $\mathbf{e}$  is the vector of nodal coordinates,  $\mathbf{M}$  is the brake pipe global coefficient matrix that results from assembling the  $\mathbf{M}^e$  element matrices, and  $\mathbf{Q}$  is the right hand side vector that results from the assembly of the  $\mathbf{Q}^e$  element vectors. Using the position of the locomotive automatic brake valve handle, the initial conditions and inputs for Eq. 4.23 can be defined and used with numerical integration methods to solve for the pressure and the velocity distribution. Using the approach described in this section in which the new variable  $q = pu$  is introduced, one obtains constant symmetric  $\mathbf{M}^e$  and  $\mathbf{M}$  matrices. Therefore, one needs to define the LU factors of  $\mathbf{M}$  only once at the start of the simulation. The effect of the air leakage in the finite element formulation presented in this section can be considered by introducing this effect at the nodal points using the *isotropic approach* or the *average density approach* (Abdol-Hamid, 1986). The latter is the approach adopted in this investigation.

#### 4.3.1. Alternate Formulation

Another alternate approach is to use the same assumptions and combine the continuity equation of Eq. 4.13 with the one dimensional form of the momentum equation of Eq. 4.5 to obtain the following coupled system of first order partial differential equations:

$$\left. \begin{aligned} \frac{\partial \rho}{\partial t} + \frac{\partial(\rho u)}{\partial x} + L &= 0 \\ \rho \frac{\partial u}{\partial t} + \rho u \frac{\partial u}{\partial x} + \frac{\partial p}{\partial x} &= f_b \end{aligned} \right\} \quad (4.24)$$

Using Eq. 4.16 ( $\rho = p/\gamma_t$ ), one obtains

$$\left. \begin{aligned} \frac{\partial p}{\partial t} + \frac{\partial(pu)}{\partial x} + \gamma_t L &= 0 \\ p \frac{\partial u}{\partial t} + pu \frac{\partial u}{\partial x} + \gamma_t \frac{\partial p}{\partial x} &= \gamma_t f_b \end{aligned} \right\} \quad (4.25)$$

As an alternative to introducing the variable  $q = pu$ , one can use  $p$  and  $u$  instead of using  $p$  and  $q$ . One can, however, show that the use of Eq. 4.25 instead of Eq. 4.18 will not lead to a constant coefficient matrix. In general, a constant coefficient matrix can always be obtained if the number of variables is not reduced using the gas law of Eq. 4.16. Nonetheless, the advantage of the form of Eq. 4.25 is that the pressure and velocities can be interpolated independently.

### 4.3.2. Wall Friction Forces

A simple expression for the pipe wall friction force  $F_s$  is used in this study. In the case of duct flow, one may assume that the force  $F_s$  is only related to the wall shear stress as (Abdol-Hamid, 1986)

$$F_s = \tau \pi d \quad (4.26)$$

where  $d$  is the hydraulic diameter, and  $\tau$  is the one dimensional flow shear stress. They are defined as (Abdol-Hamid, 1986)

$$d = \sqrt{\frac{4}{\pi}} A_{avg} = \sqrt{\frac{4}{\pi \Delta x} \int_x^{x+\Delta x} A dx}, \quad \tau = f_w \frac{\rho u^2}{8} \left( \frac{u}{|u|} \right) \quad (4.27)$$

where  $A_{avg}$  is the average area, and the wall friction factor  $f_w$  is a function of the local Reynolds number  $Re$ . The following relation between  $f_w$  and  $Re$  is often used:

$$f_w = a(Re)^b \quad (4.28)$$

where  $a$  and  $b$  are selected to give a good fit to data for different flow regimes; laminar, transition and turbulent. The expression for the friction force  $F_s$  can be introduced to the momentum equation. If the area of the pipe is constant, then  $A_{avg} = A = \text{constant}$ .

#### **4.4. Train Nonlinear Dynamic Equations**

The mathematical models of the air flow in the brake pipe and the commands of the locomotive automatic brake valve can be used to define the braking scenarios that affect the train longitudinal dynamics. In this section, the nonlinear dynamic equations of the train cars are developed using the trajectory coordinates. It is assumed that rail vehicle dynamics has no effect on the air flow in the brake pipe, while the braking forces can have a significant effect on the train longitudinal forces.

##### **4.4.1. Position, Velocity, and Acceleration**

In order to develop the nonlinear dynamic equations of motion of the train, the global position vector of an arbitrary point on a car body is first defined. The position vector  $\mathbf{r}^i$  of an arbitrary point on body  $i$  with respect to the global coordinate system can be defined as shown in Fig. 41 as (Shabana, 2010)

$$\mathbf{r}^i = \mathbf{R}^i + \mathbf{A}^i \bar{\mathbf{u}}^i \quad (4.29)$$

where  $\mathbf{R}^i$  is the global position vector of the origin of the body coordinate system,  $\bar{\mathbf{u}}^i$  is the position vector of the arbitrary point on the body with respect to the local coordinate system, and  $\mathbf{A}^i$  is the rotation matrix that defines the orientation of the local coordinate system with respect to the global system. In rigid body dynamics,  $\bar{\mathbf{u}}^i$  is constant and does not depend on time.

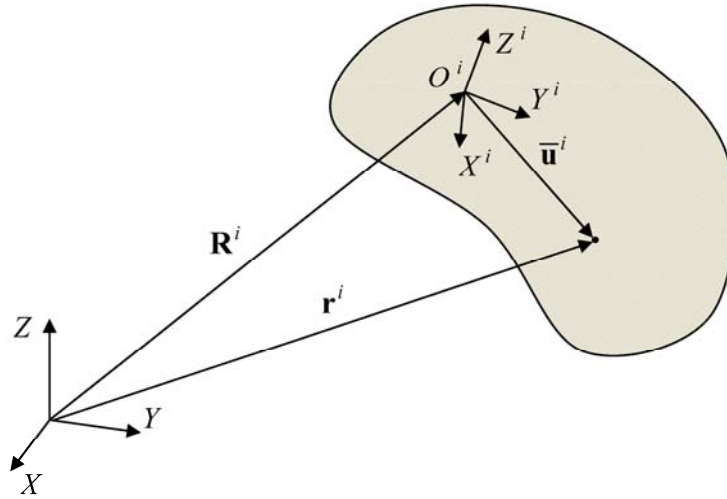


Figure 41. Coordinate systems

Differentiating Eq. 4.29 with respect to time, one obtains the absolute velocity vector defined as

$$\dot{\mathbf{r}}^i = \dot{\mathbf{R}}^i + \boldsymbol{\omega}^i \times \mathbf{u}^i \quad (4.30)$$

where  $\boldsymbol{\omega}^i$  is the absolute angular velocity vector defined in the global coordinate system, and  $\mathbf{u}^i = \mathbf{A}^i \bar{\mathbf{u}}^i$ . The absolute acceleration vector is obtained by differentiating the preceding equation with respect to time, leading to

$$\ddot{\mathbf{r}}^i = \ddot{\mathbf{R}}^i + \boldsymbol{\alpha}^i \times \mathbf{u}^i + \boldsymbol{\omega}^i \times (\boldsymbol{\omega}^i \times \mathbf{u}^i) \quad (4.31)$$

where  $\boldsymbol{\alpha}^i$  is the angular acceleration vector of body  $i$ . The preceding equation can also be written in the following alternate form:

$$\ddot{\mathbf{r}}^i = \ddot{\mathbf{R}}^i + \mathbf{A}^i \left( \bar{\boldsymbol{\alpha}}^i \times \bar{\mathbf{u}}^i + \bar{\boldsymbol{\omega}}^i \times (\bar{\boldsymbol{\omega}}^i \times \bar{\mathbf{u}}^i) \right) \quad (4.32)$$

where  $\boldsymbol{\alpha}^i = \mathbf{A}^i \bar{\boldsymbol{\alpha}}^i$  and  $\boldsymbol{\omega}^i = \mathbf{A}^i \bar{\boldsymbol{\omega}}^i$ . The angular velocity vectors defined, respectively, in the global and body coordinate systems can be written in terms of the time derivatives of the orientation coordinates  $\boldsymbol{\theta}^i$  as follows:

$$\boldsymbol{\omega}^i = \mathbf{G}^i \dot{\boldsymbol{\theta}}^i, \quad \bar{\boldsymbol{\omega}}^i = \bar{\mathbf{G}}^i \dot{\boldsymbol{\theta}}^i \quad (4.33)$$

where  $\mathbf{G}^i$  and  $\bar{\mathbf{G}}^i$  can be expressed in terms of the orientation parameters  $\boldsymbol{\theta}^i$  (Shabana et al., 2008).

#### 4.4.2. Trajectory Coordinates

The trajectory coordinate formulation is suited for the study of the train longitudinal force dynamics since the car body degrees of freedom can be systematically reduced to a set that can be related to the track geometry. A centroidal body coordinate system is introduced for each of the railroad vehicle components. In addition to the centroidal body coordinate system, a *body/track coordinate system* that follows the motion of the body is introduced. The location of the origin and the orientation of the body/track coordinate system are defined using one geometric parameter  $s^i$  that defines the distance travelled by the body along the track. The body coordinate system is selected such that it has no displacement in the longitudinal direction of motion with respect to the body/track coordinate system. Two translational coordinates,  $y^{ir}$  and  $z^{ir}$ ; and three angles,  $\psi^{ir}$ ,  $\phi^{ir}$ , and  $\theta^{ir}$ , are used to define the position and orientation of the body coordinate system with respect to the body/track coordinate system  $X^{ti}Y^{ti}Z^{ti}$ , as shown in Fig. 42.

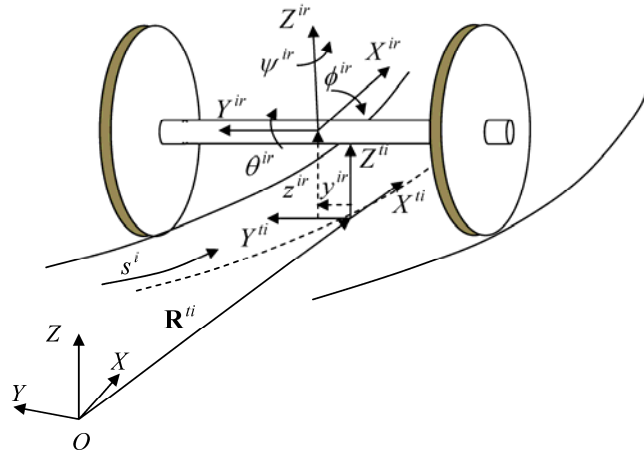


Figure 42. Trajectory coordinates

Therefore, for each body  $i$  in the system, the following six trajectory coordinates can be used:

$$\mathbf{p}^i = [s^i \quad y^{ir} \quad z^{ir} \quad \psi^{ir} \quad \phi^{ir} \quad \theta^{ir}]^T \quad (4.34)$$

In terms of these coordinates, the global position vector of the center of mass of body  $i$  can be written as

$$\mathbf{R}^i = \mathbf{R}^{ti} + \mathbf{A}^{ti} \bar{\mathbf{u}}^{ir} \quad (4.35)$$

where  $\bar{\mathbf{u}}^{ir}$  is the position vector of the center of mass with respect to the body/track coordinate system,  $\mathbf{R}^{ti}$  is the global position vector of the origin of the trajectory coordinate system, and  $\mathbf{A}^{ti}$  is the matrix that defines the orientation of the body/track coordinate system and is a function of three predefined Euler angles  $\psi^{ti}$ ,  $\phi^{ti}$ , and  $\theta^{ti}$  which are used to define the track geometry. The vector  $\mathbf{R}^{ti}$  and the matrix  $\mathbf{A}^{ti}$  are functions of only one time dependent arc length parameter  $s^i$ . For a given  $s^i$ , one can also determine the three Euler angles

$\boldsymbol{\theta}^{ii}(s^i) = [\psi^{ii}(s^i) \quad \theta^{ii}(s^i) \quad \phi^{ii}(s^i)]^T$  that enter into the formulation of the rotation matrix  $\mathbf{A}^{ii}$

(Shabana et al., 2008). The vector  $\bar{\mathbf{u}}^{ir}$  can be written as

$$\bar{\mathbf{u}}^{ir} = [0 \quad y^{ir} \quad z^{ir}]^T \quad (4.36)$$

The matrix  $\mathbf{A}^{ir}$  that defines the orientation of the body coordinate system with respect to the body/track coordinate system can be expressed in terms of the three time dependent Euler angles  $\boldsymbol{\theta}^{ir} = [\psi^{ir} \quad \theta^{ir} \quad \phi^{ir}]^T$  previously defined.

#### 4.4.3. Equations of Motion

A velocity transformation matrix that relates the absolute Cartesian accelerations to the trajectory coordinate accelerations can be systematically developed. Using the velocity transformation and the Newton-Euler equations that govern the spatial motion of the rigid bodies, the equations of motion of the car bodies expressed in terms of the trajectory coordinates can be developed. The following form of the Newton-Euler equations is used in this chapter (Shabana, 2010):

$$\begin{bmatrix} m^i \mathbf{I} & \mathbf{0} \\ \mathbf{0} & \bar{\mathbf{I}}_{\theta\theta}^i \end{bmatrix} \begin{bmatrix} \ddot{\mathbf{R}}^i \\ \ddot{\boldsymbol{\alpha}}^i \end{bmatrix} = \begin{bmatrix} \mathbf{F}_e^i \\ \bar{\mathbf{M}}_e^i - \bar{\boldsymbol{\omega}}^i \times (\bar{\mathbf{I}}_{\theta\theta}^i \bar{\boldsymbol{\omega}}^i) \end{bmatrix} \quad (4.37)$$

where  $m^i$  is the mass of the rigid body;  $\mathbf{I}$  is a  $3 \times 3$  identity matrix;  $\bar{\mathbf{I}}_{\theta\theta}^i$  is the inertial tensor defined with respect to the body coordinate system;  $\mathbf{F}_e^i$  is the resultant of the external forces applied on the body defined in the global coordinate system; and  $\bar{\mathbf{M}}_e^i$  is the resultant of the external moments acting on the body defined in the body coordinate system. The forces and moments acting on the body include the effect of the gravity, braking forces, coupler forces, and tractive effort and motion resisting forces. If  $\mathbf{a}^i$  is the vector of absolute Cartesian accelerations

of the body, one can use the kinematic description given in this section to write the Cartesian accelerations in terms of the trajectory accelerations as

$$\mathbf{a}^i = \mathbf{B}^i \ddot{\mathbf{p}}^i + \boldsymbol{\gamma}^i \quad (4.38)$$

In this equation,  $\mathbf{a}^i = [\ddot{\mathbf{R}}^{iT} \quad \ddot{\boldsymbol{\alpha}}^{iT}]^T$ ,  $\mathbf{B}^i$  is a velocity transformation matrix, and  $\boldsymbol{\gamma}^i$  is a quadratic velocity vector (Shabana et al., 2008). Substituting Eq. 4.38 into Eq. 4.37 and pre-multiplying by the transpose of the velocity transformation matrix  $\mathbf{B}^i$ , one obtains the dynamic equations expressed in terms of the trajectory coordinates, as described in detail in (Shabana et al., 2008).

#### **4.5. Locomotive Valve Model**

The air pressure in the brake pipe system is controlled by the brake locomotive automatic brake valve. The mathematical model of the 26C locomotive valve developed by Abdol-Hamid (1986) is used in this chapter. The valve and its main components are shown in Fig. 43.

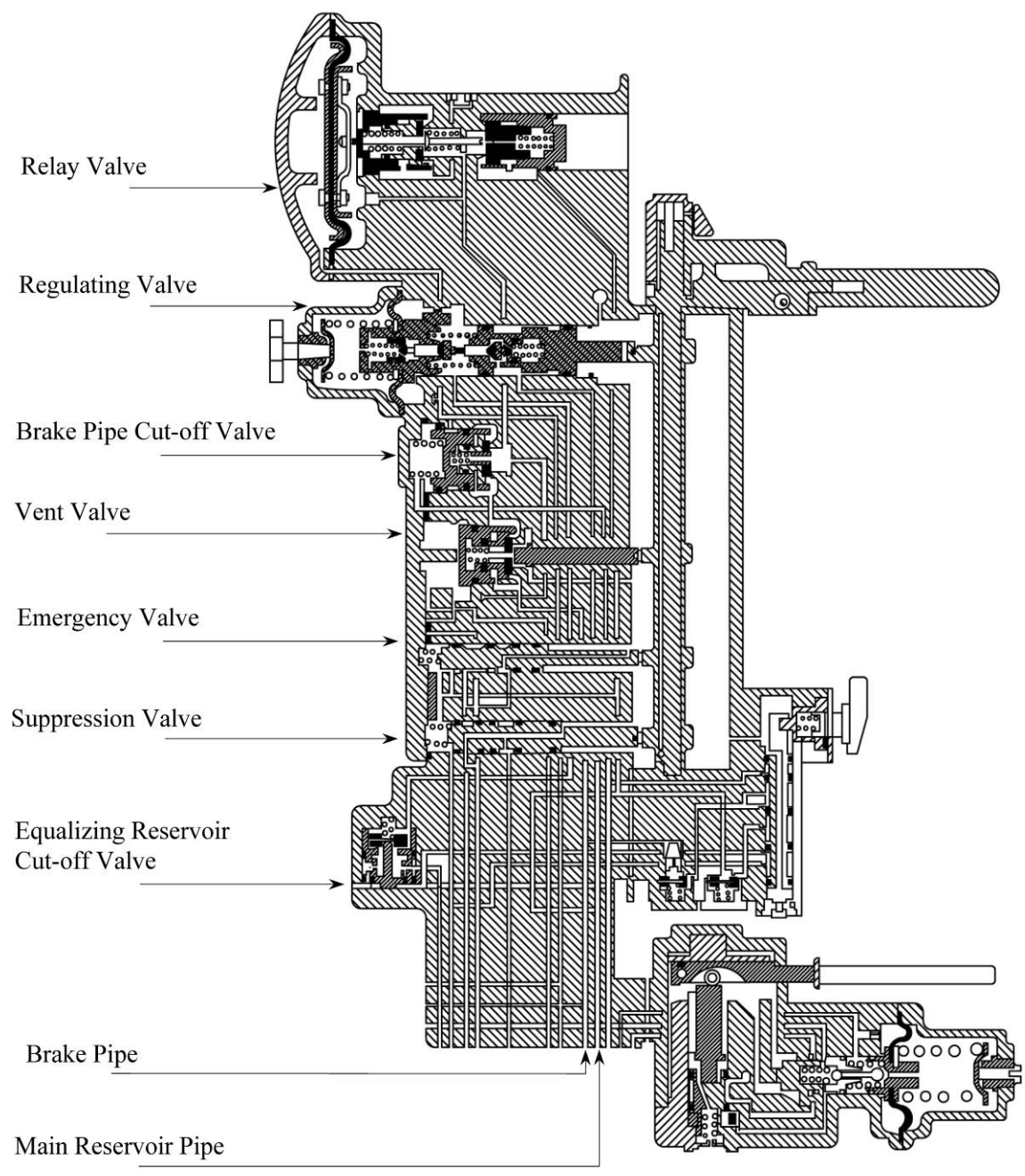


Figure 43. 26C valve scheme

The primary function of the automatic brake valve is to control air pressure in the brake pipe allowing for the application or release of the train and locomotive brakes. By changing the

position of the handle of this valve, the air pressure can be reduced (venting air to the atmosphere) or increased (recharging) at a controlled rate to *apply* or *release* the brakes, respectively. The main components of the 26C automatic brake valve are the *regulating valve*, *relay valve*, *brake pipe cut-off valve*, *vent* and *emergency valves*, and *suppression valve*. The main function of the *regulating valve* is to control the *equalizing reservoir* pressure which has a value that depends on the position assumed by the automatic brake valve handle. This pressure controls the *relay valve* which controls the air pressure along the brake pipe for the purpose of brake application or release. The *brake pipe cut-off valve* is located between the relay valve and the brake pipe, and its function is to allow communication with the pipe only when a threshold pressure value is reached. The *vent* and *emergency valves* are activated only in case of emergency and their function is to vent the air in both the brake pipe and the equalizing reservoir to the atmosphere. The resulting sudden drop in the air pressure leads to a faster brake application. The *suppression valve* is used to control the communication between the equalizing and the main reservoir. In this chapter, only the mathematical models of the first three valves; relay valve, regulating valve, and brake pipe cut-off valve, are developed. As in (Abdol-Hamid, 1986), a variable or a component  $y_{i,j}$  of the locomotive automatic brake valve denotes variable or component number  $j$  associated with valve  $i$ ; for the relay valve,  $i = 1$ ; for the regulating valve,  $i = 2$ ; and for the brake pipe cut-off valve,  $i = 3$ .

In order to be able to develop the valve equations, several basic thermodynamics relationships must be used (John and Keith, 2006; White, 2008). The first is the universal law of gases for a volume  $V_f$  of a component  $f$  given by

$$P_f V_f = m_f R_g \Theta_f \quad (4.39)$$

where  $P_f$  is the absolute pressure inside the volume ( $\text{N/m}^2$ ),  $V_f$  is the volume ( $\text{m}^3$ ),  $m_f$  is the mass ( $\text{Kg}$ ),  $R_g$  is the gas constant ( $\text{J}/(\text{Kg } ^\circ\text{K})$ ) and  $\Theta_f$  is the temperature ( $^\circ\text{K}$ ). Differentiating the preceding equation with respect to time and assuming isothermal process ( $\Theta_f = \Theta$  is constant), one obtains

$$\frac{dP_f}{dt} = \frac{1}{V_f} \left( R_g \Theta \frac{dm_f}{dt} - P_f \frac{dV_f}{dt} \right) \quad (4.40)$$

There are different formulas for calculating the rate of mass flow through orifices (Abdol-Hamid, 1986; John and Keith, 2006; White, 2008). In this chapter, the following equation is used for air:

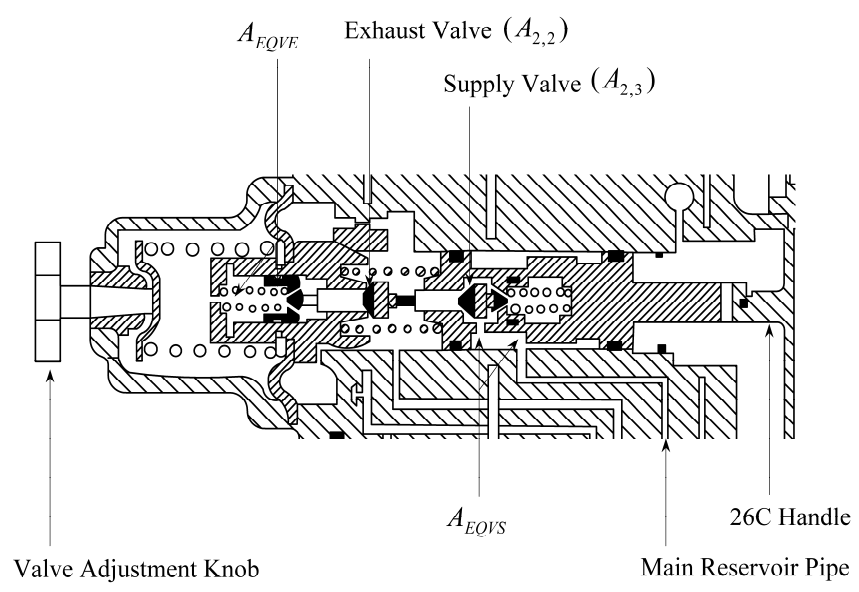
$$\dot{m}_{air} = 0.6AP_d \sqrt{\frac{|r^2 - 1|}{R_g \Theta} \frac{|r - 1|}{r - 1}} \quad (4.41)$$

In this equation,  $A$  is the area,  $r = P_u/P_d$ , and  $P_u$  and  $P_d$  are, respectively, the pressure upstream and downstream of the orifice. As reported in the literature (Abdol-Hamid, 1986), the difference between different formulas is always less than 10%, which can be less than the error in calculating the geometric area of the orifice. The preceding equation, however, is simpler to use because it is valid for any value of the pressure ratio  $r$  (sonic or subsonic), while using other formulas requires a check of the value of  $r$  against the critical pressure ratio  $r_c = 1.893$  that defines whether the flow is sonic or subsonic.

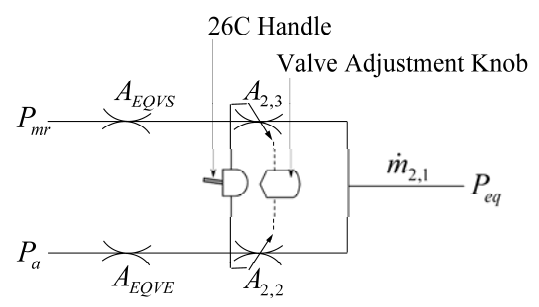
#### **4.6. Regulating Valve Operation**

The main function of the regulating valve, shown in Fig. 44a, is to control the equalizing reservoir pressure which controls the operation of the relay valve that regulates the air pressure

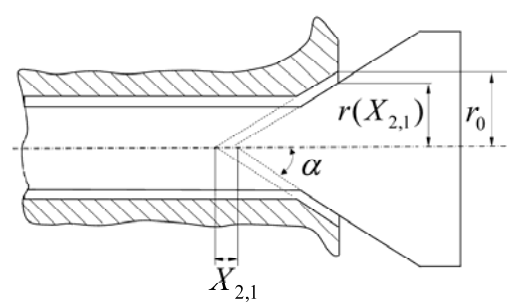
in the brake pipes. The regulating valve is controlled by one cam mounted on the shaft of the automatic brake valve handle. The valve has a self lapping feature that provides an automatic control of the equalizing reservoir pressure  $P_{eq}$  against leakage or overcharge (Abdol-Hamid, 1986).



(a) Regulating valve scheme



(b) Fluid network



(c) Valve areas

Figure 44. 26C regulating valve

#### 4.6.1. Brake Application and Release

When the automatic brake valve handle is in the *Release/Recharge position*, the air pressure of the brake pipe  $P_{bp}$  must increase and the equalizing reservoir must be recharged. In this scenario, the cam rotates to a higher position allowing the supply valve seat  $A_{2,3}$  to move left away from the handle, and causing the exhaust valve  $A_{2,2}$  to be sealed. As a result, the air from the main reservoir with pressure  $P_{mr}$  flows through the supply valve  $A_{2,3}$  and supply orifice  $A_{EQVS}$  reaching the inner diaphragm chamber  $V_{2,1}$ , through the equalizing reservoir cut-off valve to, finally, the equalizing reservoir  $V_{eq}$ . The equalizing reservoir pressure  $P_{eq}$  increases causing the supply valve to start closing.

When the handle is within the *service mode sector*, the air pressure of the brake pipe  $P_{bp}$  has to decrease in order to apply the car brakes. The regulating valve has to reduce the equalizing reservoir pressure  $P_{eq}$  which controls the relay valve that regulates the air flow to and from the brake pipe. The pressure reduction depends on the automatic brake valve handle position from the full service position. In the case of brake application, the cam rotates to a lower position allowing the regulating valve spool to move towards the handle (right), while the supply valve  $A_{2,3}$  is sealed and the exhaust valve  $A_{2,2}$  is opened. At the same time, the air pressure  $P_{mr}$  from the main reservoir is removed, causing the equalizing reservoir cut-off valve to close. This allows the air to flow only from the equalizing reservoir to the regulating valve, preventing any possible increase of the equalizing reservoir pressure  $P_{eq}$  during the entire application. Thus the air flows from the equalizing reservoir  $V_{eq}$  through the cut-off valve, the inner diaphragm

chamber  $V_{2,1}$ , the exhaust valve  $A_{2,2}$  and its orifice  $A_{EQVE}$  to reach finally the atmosphere. As the equalizing reservoir pressure  $P_{eq}$  decreases, the exhaust valve seat moves right, causing the exhaust valve to start closing. The fluid network diagram of the regulating valve is shown in Fig. 44b. From this figure, one can see the two orifice areas ( $A_{EQVS}$  and  $A_{EQVE}$ ), which are fixed, and the  $A_{2,2}$  and  $A_{2,3}$  areas of the exhaust and supply valve respectively, which are variable and controlled by the handle position and air flow. The equalizing reservoir is connected to the outer chamber of the relay valve, and therefore, the pressure  $P_{1,1}$  inside the relay valve outer chamber can be controlled by the equalizing reservoir pressure  $P_{eq}$ . The pressure  $P_{1,1}$  is used to control the operations of the relay valve which controls the pressure in the brake pipe. The relay valve operations are discussed in more detail in the following section.

#### 4.6.2. Pressure Rate

In order to evaluate the time rate of change of the pressure in the outer chamber of the relay valve  $P_{1,1}$ , the mass flow rate  $\dot{m}_{1,1}$  through the feedback orifice  $A_{1,1}$  must be calculated. The time rate of change of equalizing reservoir pressure  $P_{eq}$  depends on the rate of the mass flow  $\dot{m}_{1,1}$  to the relay valve through  $A_{1,1}$ , plus the mass flow rate  $\dot{m}_{2,1}$  through either the regulating supply valve or the exhaust valve depending on the braking scenario. Let  $P_{REG}$  denote the pressure inside the regulating valve, and  $A_{REG}$  denote the equivalent areas for both the supply and the exhaust valve connections. The equivalent area for the supply valve used in the case of brake release can be obtained assuming series connection as

$$A_{REG} = \frac{1}{\sqrt{\frac{1}{A_{EQVS}^2} + \frac{1}{A_{2,3}^2}}} = \frac{A_{EQVS} A_{2,3}}{\sqrt{A_{EQVS}^2 + A_{2,3}^2}} \quad (4.42)$$

where  $A_{2,3}$  is variable depending on the handle position, while  $A_{EQVS}$  is constant (see appendix).

In the case of brake application, the exhaust valve is used. In this case, the equivalent area for this valve connection is given, assuming again a series connection, as

$$A_{REG} = \frac{1}{\sqrt{\frac{1}{A_{EQVE}^2} + \frac{1}{A_{2,2}^2}}} = \frac{A_{EQVE} A_{2,2}}{\sqrt{A_{EQVE}^2 + A_{2,2}^2}} \quad (4.43)$$

In this equation,  $A_{2,2}$  can vary depending on the handle position; while  $A_{EQVE}$  is constant.

Applying Eq. 4.40 to the time rate change of  $P_{eq}$  and assuming the volume  $V_{eq}$  to be constant, one obtains

$$\frac{dP_{eq}}{dt} = \frac{R_g \Theta}{V_{eq}} \left( \frac{dm_{2,1}}{dt} - \frac{dm_{1,1}}{dt} \right) \quad (4.44)$$

Using Eq. 4.41, the mass flow rate  $\dot{m}_{2,1}$  can be written as

$$\dot{m}_{2,1} = 0.6 A_{REG} P_{eq} \sqrt{\frac{|r^2 - 1|}{R_g \Theta} \frac{|r - 1|}{r - 1}} \quad (4.45)$$

where  $r = P_{REG}/P_{eq}$  and  $P_{REG} = P_{mr}$  in the case of brake release and  $P_{REG} = P_a$  in the case of brake application, where  $P_a$  is the atmospheric pressure.

### 4.6.3. Equilibrium of the Regulating Valve Diaphragm

Because the areas  $A_{2,2}$  and  $A_{2,3}$  are functions of the valve displacement  $X_{REG}$ , it is important to evaluate this displacement. This displacement can be determined by studying the equilibrium of

the regulating valve diaphragm which is subjected to two forces; one on each of its side. The first force is due to the equalizing pressure  $P_{eq}$  and is equal to  $F_1 = -P_{eq}A_{2,1}$ . The second force is due to the spring force and is defined as  $F_2 = S_{2,1} = K_{2,1}X_{REG} + L_{2,1}$ , where  $K_{2,1}$  is the spring stiffness and  $L_{2,1}$  is the spring preload force. Neglecting the effect of the diaphragm inertia, the equilibrium condition of the diaphragm is  $F_1 + F_2 = 0$ , which defines  $X_{REG}$  as

$$X_{REG} = \frac{P_{eq}A_{2,1} - L_{2,1}}{K_{2,1}} \quad (4.46)$$

The displacement  $X_{REG}$  and the geometry of the supply and exhaust valves can be used to evaluate the areas  $A_{2,2} = A_{2,2}(X_{REG})$  and  $A_{2,3} = A_{2,3}(X_{REG})$  as described in the appendix (Abdol-Hamid, 1986). The areas  $A_{2,2}$  and  $A_{2,3}$  can then be substituted into Eq. 4.45, which in turn is substituted into Eq. 4.44, demonstrating that the right hand side of Eq. 4.45 depends nonlinearly on the equalizing reservoir pressure  $P_{eq}$ .

The valve starts to close when  $X_{REG}$  is less than a certain value  $X_C$ , which is the maximum effective opening made by the valves obtained when the equalizing reservoir pressure  $P_{eq}$  reaches a cut-off value of  $P_C$  which is the final steady state value of  $P_{eq}$ . Therefore, as an alternative to using Eq. 4.46, one can use the following equation:

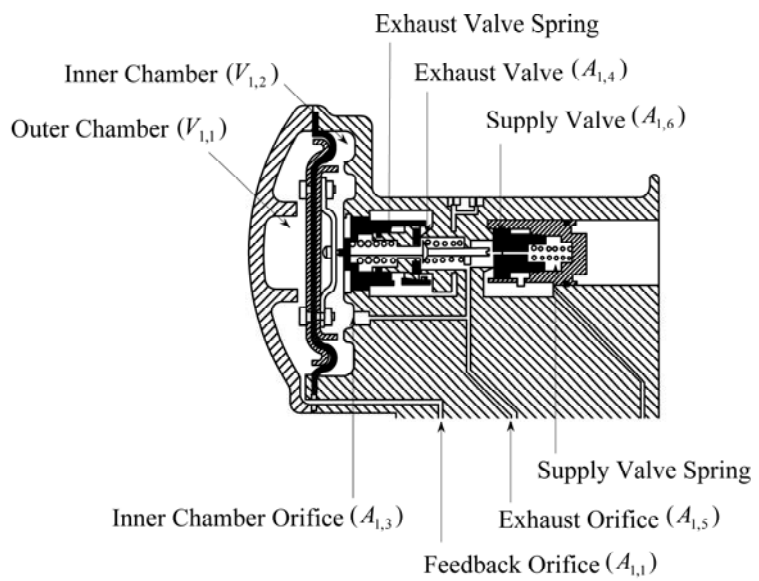
$$X_{2,1} = \frac{|P_{eq} - P_C|A_{2,1}}{K_{2,1}} \quad (4.47)$$

with the assumption that  $|P_{eq} - P_C| \leq K_{2,1}X_C/A_{2,1}$ . In the preceding equation,  $X_{REG}$  is renamed  $X_{2,1}$ . Comparing Eqs. 4.46 and 4.47, one can show that  $P_C A_{2,1} = L_{2,1} + K_{2,1}(X_{REG} - X_{2,1})$  (Abdol-

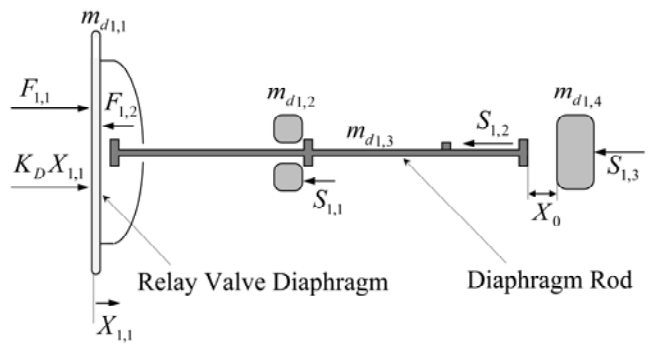
Hamid, 1986). Starting with an initial value for  $P_{eq}$ , Eq. 4.44 can be integrated to determine the value of the equalizing reservoir pressure  $P_{eq}$  as function of time and the position of the locomotive automatic brake valve handle.

#### **4.7. Relay Valve Operation**

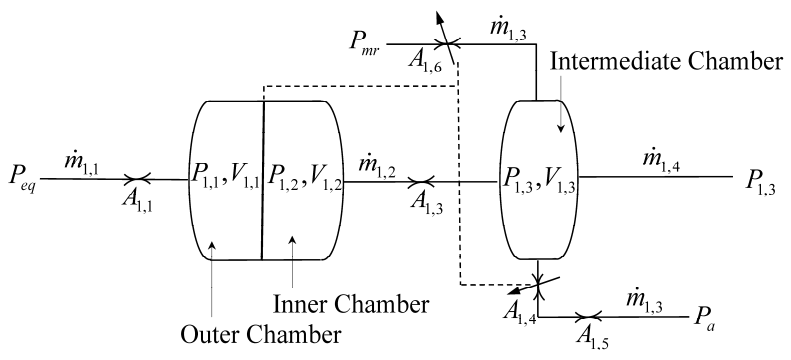
Figure 45a shows a schematic diagram of the relay valve and its components. The diaphragm chamber is divided into two parts; the outer chamber with volume  $V_{1,1}$  and pressure  $P_{1,1}$ , and the inner chamber with volume  $V_{1,2}$  and pressure  $P_{1,2}$ . The displacement of the diaphragm causes the diaphragm rod to move, thereby controlling the relay supply valve  $A_{1,6}$  and the relay exhaust valve  $A_{1,4}$ .



(a) Relay valve scheme



(b) Relay valve free body diagram



(c) 26C relay valve fluid network  
Figure 45. Relay valve

As shown in Fig. 45b, there is always a gap  $X_0$  between the diaphragm rod and one of the two relay valves (supply and exhaust);  $X_0$  is the gap between the diaphragm rod and the supply valve when the diaphragm is in its rest position. The displacement of the diaphragm is measured by the variable  $X_{1,1}$  along the longitudinal axis of the diaphragm rod;  $X_{1,1} = 0$  in the diaphragm rest position. When the diaphragm moves to right, it pushes the rod which reaches the supply valve after a displacement  $X_0$ ; when moving to the left, instead, the diaphragm is free until a displacement of  $X_{1,1} = -X_l$  where it starts to pull the rod and open the exhaust valve. Moving right opens the supply valve  $A_{1,6}$  (fully open when the maximum right displacement, controlled by stops,  $X_{1,1} = X_s$  is reached); and moving left controls the opening of the exhaust valve  $A_{1,4}$  (fully open when the maximum left displacement, controlled by stops,  $X_{1,1} = -X_e$  is reached). Because the gap is always present between the rod and at least one of the valves, only one (or none) of the two valves can be open at the same time. Through the feedback orifice  $A_{1,1}$  of the equalizing reservoir, the air can enter or leave the outer chamber  $V_{1,1}$ , adjusting the value of the pressure  $P_{1,1}$ . This pressure exerts a force  $F_{1,1}$  on the outer side  $A_{1,2}$  of the diaphragm causing it to move. This force is opposed, at the other side of the diaphragm  $A_{1,2}$ , by the force  $F_{1,2}$  exerted by the pressure  $P_{1,2}$  of the inner chamber  $V_{1,2}$ . The other forces acting are those of the springs; the exhaust valve spring force  $S_{1,1}$ , the supply valve spring force  $S_{1,3}$  and the diaphragm rod spring force  $S_{1,2}$ . The effect of the stiffness of the diaphragm can also be considered.

#### 4.7.1. Brake Release and Application

During the *brake Release/Charge mode*, the equalizing reservoir pressure  $P_{eq}$  is increased by the action of the regulating valve, as previously explained. Consequently,  $P_{1,1}$  also increases so that the net force acting on the diaphragm makes it move to the right causing the supply valve to start to open. The air, from the main reservoir with pressure  $P_{mr}$ , flows through the supply valve to the intermediate volume  $V_{1,3}$  (located between the inner chamber  $V_{1,2}$  and the brake pipe cut-off valve). If the air pressure at the brake pipe cut-off valve is large enough to overcome the valve spring preload, the valve opens and the air can flow to the brake pipe, increasing its pressure  $P_{bp}$  causing the brakes to release. The pressure on both sides of the diaphragm ( $P_{1,1}$  of the outer chamber and  $P_{1,2}$  of the inner chamber) increases with almost the same time rate. When the brake pipe cut-off valve opens,  $P_{1,2}$  in the inner chamber drops: this causes the diaphragm rod to move to the right, increasing the opening of the supply valve, and causing more air to flow through this valve, compensating for the pressure drop. Slowly the brake pipe pressure  $P_{bp}$  and the pressure  $P_{1,2}$  of the inner chamber reach the value of  $P_{1,1}$  (very close to the value of  $P_{eq}$ ) causing the diaphragm to move left towards its lap position ( $X_{1,1} = X_0$ ) and the supply valve starts closing.

In the case of brake application, the regulating valve causes the equalizing reservoir pressure  $P_{eq}$  to decrease, and consequently, the value of the pressure  $P_{1,1}$  in the outer chamber decreases. As a result, the net force on the diaphragm reverses its direction and the diaphragm and its rod starts moving to the left opening the exhaust valve. The air flows from the brake pipe

through the exhaust valve opening  $A_{1,4}$  and its orifice  $A_{1,5}$  to the atmosphere. As a result, the brake pipe pressure  $P_{bp}$  drops at a service rate of application causing the brake application. In the steady state case, the pressures  $P_{1,1}$ ,  $P_{1,2}$  and  $P_{bp}$  are approximately equal to the equalizing reservoir pressure  $P_{eq}$ . In case of emergency, the pressure in the brake pipe decreases rapidly (at an emergency rate of application) to the atmospheric pressure. To avoid the situation in which the relay valve goes into the release mode, the vent valve is used to vent the air in the equalizing reservoir  $V_{eq}$  to the atmosphere, causing the pressure  $P_{eq}$  to decrease and, consequently, the pressure  $P_{1,1}$  also decreases.

#### 4.7.2. Mathematical Model

The time rate of change of the outer chamber pressure  $P_{1,1}$  is due to the mass flow rate  $\dot{m}_{1,1}$  from the equalizing reservoir through the feedback orifice  $A_{1,1}$ . Keeping in mind that  $V_{1,1}$  is not constant; the use of Eq. 4.40 leads to

$$\frac{dP_{1,1}}{dt} = \frac{1}{V_{1,1}} \left( R_g \Theta \frac{dm_{1,1}}{dt} - P_{1,1} \frac{dV_{1,1}}{dt} \right) \quad (4.48)$$

Considering the fact that  $V_{1,2}$  is not always constant, the time rate of change of  $P_{1,2}$  in the inner chamber, due to the mass flow rate through the inner chamber orifice  $A_{1,3}$  is

$$\frac{dP_{1,2}}{dt} = \frac{1}{V_{1,2}} \left( R_g \Theta \frac{dm_{1,2}}{dt} - P_{1,2} \frac{dV_{1,2}}{dt} \right) \quad (4.49)$$

The time rate of change of the pressure  $P_{1,3}$  in the intermediate constant volume  $V_{1,3}$  is due to the mass flow rates  $-\dot{m}_{1,2}$  through the inner chamber orifice  $A_{1,3}$  (mass flow from the

inner chamber);  $\dot{m}_{1,3}$  through the supply valve  $A_{1,6}$  or through the exhaust valve  $A_{1,4}$  (plus the exhaust orifice  $A_{1,5}$ ); and  $\dot{m}_{1,4}$  through the brake pipe cut-off valve  $A_{3,3}$  (mass flow from the brake pipe). Therefore, the equation for the pressure  $P_{1,3}$  is

$$\frac{dP_{1,3}}{dt} = \frac{R_g \Theta}{V_{1,3}} \left( \frac{dm_{1,3}}{dt} + \frac{dm_{1,4}}{dt} - \frac{dm_{1,2}}{dt} \right) \quad (4.50)$$

The time rate of the two chamber volumes depend on the diaphragm velocity  $u_{1,1} = dX_{1,1}/dt$  and are defined as

$$\frac{dV_{1,1}}{dt} = A_{1,2} u_{1,1}, \quad \frac{dV_{1,2}}{dt} = -A_{1,2} u_{1,1} \quad (4.51)$$

The mass flow rates that appear in the preceding equations are defined as

$$\left. \begin{aligned} \dot{m}_{1,1} &= 0.6 A_{1,1} P_{1,1} \sqrt{\frac{|r^2 - 1|}{R_g \Theta}} \frac{|r - 1|}{r - 1}, & r &= \frac{P_{eq}}{P_{1,1}} \\ \dot{m}_{1,2} &= 0.6 A_{1,3} P_{1,2} \sqrt{\frac{|r^2 - 1|}{R_g \Theta}} \frac{|r - 1|}{r - 1}, & r &= \frac{P_{1,3}}{P_{1,2}} \\ \dot{m}_{1,3} &= 0.6 A_{1,6} P_{1,3} \sqrt{\frac{|r^2 - 1|}{R_g \Theta}} \frac{|r - 1|}{r - 1}, & r &= \frac{P_{mr}}{P_{1,3}} \quad X_0 \leq X_{1,1} \leq X_S \quad (\text{supply valve open}) \\ \dot{m}_{1,3} &= 0.6 A_{EX} P_{1,3} \sqrt{\frac{|r^2 - 1|}{R_g \Theta}} \frac{|r - 1|}{r - 1}, & r &= \frac{P_a}{P_{1,3}} \quad (\text{otherwise}) \\ \dot{m}_{1,4} &= 0.6 A_{3,3} P_{1,3} \sqrt{\frac{|r^2 - 1|}{R_g \Theta}} \frac{|r - 1|}{r - 1}, & r &= \frac{P_{bp}}{P_{1,3}} \end{aligned} \right\} \quad (4.52)$$

where  $A_{EX} = A_{1,4} A_{1,5} / \sqrt{A_{1,4}^2 + A_{1,5}^2}$  is the equivalent area of the exhaust valve and the orifice. In

order to determine the velocity  $u_{1,1}$ , the equation of motion of the diaphragm must be used. Using

Fig. 45b, one can show that the diaphragm equation of motion can be written as

$$m_{d1} \frac{du_{1,1}}{dt} = F_{1,1} - F_{1,2} - S_{1,1} - S_{1,2} - S_{1,3} - K_D X_{1,1} \quad (4.53)$$

where  $F_{1,1}$  is the force due to the action of pressure  $P_{1,1}$  in the outer chamber  $V_{1,1}$ ;  $F_{1,2}$  is the force generated by pressure  $P_{1,2}$  in the inner chamber  $V_{1,2}$ ;  $S_{1,1}$  is the exhaust spring force;  $S_{1,2}$  is the diaphragm rod spring force;  $S_{1,3}$  is the supply spring force;  $K_D$  is the spring constant of the relay valve diaphragm; and  $m_{d1}$  is the equivalent mass of all the relay valve moving parts. Clearly,  $m_{d1}$  depends on the diaphragm displacement since not all the parts of the relay valve are always in motion, depending on which parts are in contact with the rod. The mass  $m_{d1}$  can be written as

$$\left. \begin{aligned} m_{d1} &= m_{d1,1} + m_{d1,2} + m_{d1,3} & -X_E \leq X_{1,1} \leq -X_I \\ m_{d1} &= m_{d1,1} & -X_I \leq X_{1,1} \leq 0 \\ m_{d1} &= m_{d1,1} + m_{d1,3} & 0 \leq X_{1,1} \leq X_0 \\ m_{d1} &= m_{d1,1} + m_{d1,3} + m_{d1,4} & X_0 \leq X_{1,1} \leq X_S \end{aligned} \right\} \quad (4.54)$$

where  $m_{d1,1}$ ,  $m_{d1,2}$ ,  $m_{d1,3}$  and  $m_{d1,4}$  are the masses of, respectively, the diaphragm, the exhaust valve, the diaphragm rod and the supply valve. In the preceding system of equations, the first equation is used when the diaphragm is moving left, opening the exhaust valve; the second equation is used in the small range in which the diaphragm moves freely; the third equation is used during the gap  $X_0$  that the rod has to travel before reaching the supply valve; and the last equation is used during the opening of the supply valve. The expressions for the forces that appear in Eq. 4.53 are presented in the appendix of the thesis.

### 4.7.3. Simplified Model

In order to develop a more efficient computational relay valve model, several assumptions can be made (Abdol-Hamid, 1986). First, the effect of the diaphragm inertia forces  $m_{d1} (du_{1,1}/dt)$  can be

neglected. Second, the outer chamber pressure  $P_{1,1}$  can be assumed equal to the equalizing reservoir pressure  $P_{eq}$ , that is,  $P_{1,1} \approx P_{eq}$ . Third, the pressure  $P_{1,3}$  in the intermediate chamber can be assumed equal to the inner chamber pressure  $P_{1,2}$ , that is,  $P_{1,3} \approx P_{1,2}$ . Fourth, the intermediate chamber volume  $V_{1,3}$  is small and can be assumed equal to zero ( $V_{1,3} \approx 0$ ). Using the first three assumptions, one can show that the displacement  $X_{1,1}$  takes the following form:

$$X_{1,1} = \begin{cases} X_S & H_0 < D_p \\ B_0(D_p - H_1) + X_0 & H_1 < D_p \leq H_0 \\ X_0 & H_2 < D_p \leq H_1 \\ B_1(D_p - H_3) & H_3 < D_p \leq H_2 \\ 0 & 0 < D_p \leq H_3 \\ B_2 D_p & H_4 < D_p \leq 0 \\ -X_I & H_5 < D_p \leq H_4 \\ B_3(D_p - H_5) - X_I & H_6 < D_p \leq H_5 \\ -X_E & H_6 > D_p \end{cases} \quad (4.55)$$

where

$$\left. \begin{aligned} B_0 &= \frac{A_{1,1}}{K_{1,2} + K_{1,3} + K_D}, & B_1 &= \frac{A_{1,2}}{K_{1,2} + K_D}, & B_2 &= \frac{A_{1,2}}{K_D}, & B_3 &= \frac{A_{1,2}}{K_{1,1} + K_{1,2} + K_D}, \\ H_0 &= \frac{X_S - X_0}{B_0} + H_1, & H_1 &= \frac{L_{1,3}}{A_{1,2}} + H_2, & H_2 &= \frac{X_0}{B_1} + H_3, & H_3 &= \frac{L_{1,2}}{A_{1,2}}, \\ H_4 &= -\frac{X_I}{B_2}, & H_5 &= \frac{L_{1,2} - L_{1,1}}{A_{1,2}} + H_4, & H_6 &= \frac{X_I - X_E}{B_3} + H_5, & D_p &= P_{eq} - P_{1,3} \end{aligned} \right\} \quad (4.56)$$

Note that  $P_{1,3} = P_{bp}$  for  $-X_I \leq X_{1,1} \leq X_0$ . The nine cases presented in Eq. 4.55 correspond, respectively, to the scenarios of the supply valve fully open  $X_S$ , supply valve opening,  $X_0$ , both valve closed, diaphragm rest position, diaphragm free movement, start exhaust valve opening

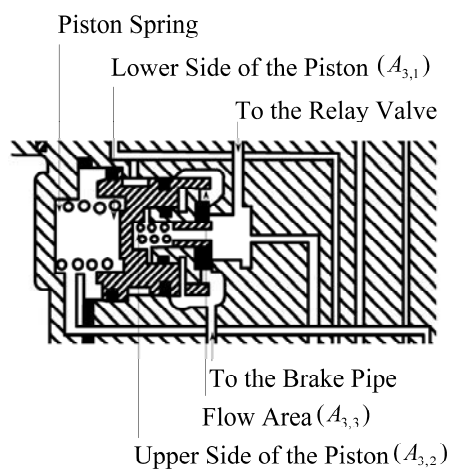
$-X_I$ , and exhaust valve fully open  $-X_E$ . In order to determine  $X_{1,1}$  of Eq. 4.55, one must determine  $P_{1,3}$  which enters in the formulation of  $D_p$ . By using the assumption  $\dot{m}_{1,3} = \dot{m}_{1,4}$ , one can show that (Abdol-Hamid, 1986)

$$P_{1,3} = \sqrt{\frac{P_{bp}^2 A_{3,3}^2 + P^2 A^2}{A_{3,3}^2 + A^2}} \quad (4.57)$$

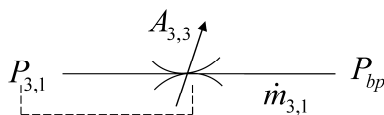
where  $A$  and  $P$  can be either  $A_{1,6}$  and  $P_{mr}$  (for the supply valve) or  $A_{EX}$  and  $P_a$  (for the exhaust valve), respectively.

#### **4.8. Brake Pipe Cut-off Valve Operation**

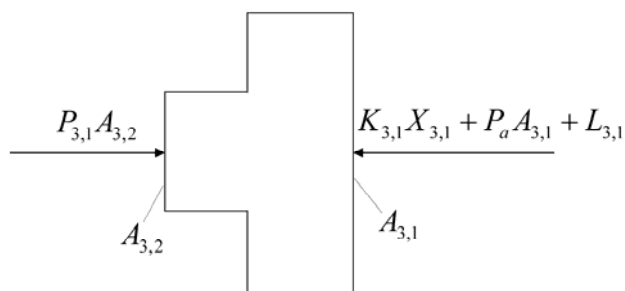
The brake pipe cut-off valve is shown in Fig. 46a. The forces acting on the piston are the forces exerted by the pressure  $P_{3,1}$  ( $P_{3,1} = P_{1,3}$ ) which act on the upper side of the piston  $A_{3,2}$ ; the force exerted by the atmospheric pressure  $P_a$  which acts on the lower side  $A_{3,1}$ ; and the spring force  $S_{3,1} = K_{3,1}X_{3,1}$  (plus preload). The valve opens if  $P_{3,1}$  overcomes the resultant of the pressure  $P_a$  force and the spring preload force. Figure 46b shows how the pressure  $P_{3,1}$  coming from the relay valve through the orifice  $A_{3,3}$ , controls the opening of the valve, allowing or preventing the air flow to the brake pipe.



(a) Brake pipe cut-off valve scheme



(b) Brake pipe cut-off valve fluid network



(c) Brake pipe cut-off valve free body diagram

Figure 46. Brake pipe cut-off valve

In order to calculate the mass flow rate through the brake pipe cut-off valve  $\dot{m}_{3,1}$ , the flow area  $A_{3,3}$  needs to be evaluated. This orifice is controlled by the pressure  $P_{3,1}$  ( $= P_{1,3}$ ) acting on the inner side of the piston  $A_{3,2}$ , which determines the piston and the valve displacement. Brake pipe cut-off piston has a very small mass which can be neglected. Using the valve free body diagram shown in Fig. 46c, the equilibrium equation is

$$P_{3,1}A_{3,2} - (P_a A_{3,1} + K_{3,1}X_{3,1} + L_{3,1}) = 0 \quad (4.58)$$

where  $K_{3,1}$  is the valve spring rate,  $X_{3,1}$  is the piston displacement,  $L_{3,1}$  is the spring preload.

The valve opens when the force due to the pressure  $P_{3,1}$  overcomes the forces generated by the atmospheric pressure  $P_a$  and the spring preload force  $L_{3,1}$ , that is, when  $P_{3,1}A_{3,2} \geq P_a A_{3,1} + L_{3,1}$ . This condition can be rewritten as  $P_{3,1} \geq P_B$ , where  $P_B = (P_a A_{3,1} + L_{3,1})/A_{3,2}$ .

Note that the area  $A_{3,3}$  of the annular ring created by the displacement  $X_{3,1}$  and the diameter  $D_{3,3}$  is  $A_{3,3} = \pi D_{3,3} X_{3,1}$ . In order to calculate this area, one needs to evaluate  $X_{3,1}$  using Eq. 4.58 as

$$\left. \begin{array}{l} X_{3,1} = 0 \\ X_{3,1} = A_{3,2} \frac{P_{3,1} - P_B}{K_{3,1}} \\ X_{3,1} = X_B \end{array} \right\} \begin{array}{l} P_{3,1} \leq P_B \\ P_B \leq P_{3,1} < P_B + \varepsilon \\ P_{3,1} \geq P_B + \varepsilon \end{array} \quad (4.59)$$

In this equation,  $P_B + \varepsilon$  is the value of pressure that makes the piston reach the maximum displacement  $X_B$  (cut-off valve fully open). These two values depend on the dimensions of the brake pipe cut-off valve.

#### 4.9. Integration of Locomotive Valve, Brake Pipe and Train Dynamic Models

The second order train nonlinear dynamic equations can be converted to a set of first order ordinary differential equations that can be integrated using a standard numerical integration method. As shown in this chapter, the first order ordinary differential equations that govern the air flow in the brake pipe can be written in the form  $\mathbf{M}\dot{\mathbf{e}} = \mathbf{Q}$  (see Eq. 4.23). For a given value of the right hand side vector  $\mathbf{Q}$  and a set of initial conditions  $\mathbf{e}_0$ , the air flow in the brake pipe differential equations can be solved numerically with the train differential equations to determine the air pressure and velocity as a function of time. In this section, two different scenarios will be discussed in order to demonstrate the integration of the brake pipe air flow and valve equations with the train nonlinear dynamic equations. The first scenario is a brake release after a train stop; while the second scenario is a brake application while the train is in motion. It should be noted that a complete air brake model must also include a car control unit that will be discussed in Chapter 5.

##### 4.9.1. Brake Release

The steps of the algorithm used in this study for the brake release are summarized as follows:

1. Before the train starts moving, one has the following conditions: the air pressures in the brake pipe and equalizing reservoir are equal to the full service brake pipe pressure, while the air flow velocity in the brake pipe is equal to zero; the brake pipe cut off valve is closed; and the relay valve is in the *intermediate state*, that is,  $P_{1,3} = P_{bp}$ .
2. For a given set of the train car body initial conditions, the train dynamic equations are formulated as a set of first order ordinary differential equations that can be solved using a standard numerical integration method. These equations are solved simultaneously with

the air flow differential equations (Eq. 4.23), the intermediate chamber pressure differential equation (Eq. 4.50), the equalizing reservoir pressure differential equation (Eq. 4.44), and the car control unit equations presented in Chapter 5 for the given initial conditions defined in the previous step.

3. In the case of a brake release, the automatic brake valve handle is moved to the release position causing the supply valve of the regulating valve to open. Depending on the value of  $X_{REG}$  defined in the previous sections (Regulating Valve operation), Eq. 4.44 given by

$$\frac{dP_{eq}}{dt} = \frac{R_g \Theta}{V_{eq}} \left( \frac{dm_{2,1}}{dt} - \frac{dm_{1,1}}{dt} \right)$$

can be numerically solved with the train dynamic equations.

In the case of the simplified relay valve model,  $\dot{m}_{1,1} = 0$ , while  $\dot{m}_{2,1}$  can be determined using Eq. 4.45 which is function of  $A_{REG}$  that depends on  $X_{REG}$  of Eq. 4.46. Therefore, Eq. 4.44 can be solved for the equalizing reservoir pressure  $P_{eq}$ . The current value of the pressure  $P_{eq}$  is monitored in order to check on the relay valve state.

4. As the equalizing reservoir pressure  $P_{eq}$  reaches a certain value, the relay supply valve starts opening. The supply valve area which is a function of  $D_P = P_{eq} - P_{1,3}$  is defined in Eq. 8 ( $X_{1,1}$  that appear in this equation can be determined using Eq. 4.55). The pressure  $P_{1,3}$  of the intermediate chamber starts to increase due to the incoming air flow from the main reservoir. If the simplified relay valve model described in Section 4.7 of this thesis is used, the pressure  $P_{1,3}$  can be determined using the equation

$P_{1,3} = \sqrt{(P_{bp}^2 A_{3,3}^2 + P_{mr}^2 A_{1,6}^2) / (A_{3,3}^2 + A_{1,6}^2)}$ . At the same time, the brake pipe cut-off valve remains closed, and therefore,  $A_{3,3} = 0$ .

5. When the pressure  $P_{1,3}$  becomes larger than the pressure  $P_B$  defined in Section 4.8 by the equation  $P_B = (P_a A_{3,1} + L_{3,1}) / A_{3,2}$ , the brake pipe cut-off valve starts opening, and the air starts to flow to the brake pipe. The area of the brake pipe cut-off valve  $A_{3,3}$  can be determined using Eq. 9 of the appendix. Using the current values of  $P_{1,3}$  and  $A_{3,3}$ , the mass flow rate of Eq. 4.52 is used to determine  $\dot{m}_{1,4}$ , which is used in the brake pipe air flow equations, close to the brake pipe cut-off valve. Note that the procedure used in this algorithm is based on Eq. 4.57 and Eq. 8 of the appendix. An alternate procedure can be developed based on Eq. 10 presented in the appendix.
6. As the air pressure  $P_{bp}$  of the brake pipe increases, the brake shoes start separating from the wheel axles, until the brake release is completed. The process, thus, ends with the relay supply valve closed (with the assumption of no leakage) and the brake pipe cut-off valve fully open. At this configuration,  $P_{1,3} = P_{bp}$ . Note that the value of the pressure  $P_{1,2}$ , which is equal to  $P_{1,3}$  in the simplified model, that determines the closing of the supply valve is controlled by the regulating valve; as  $X_{REG}$  reaches a specified known value, the pressure  $P_{eq}$  of the equalizing reservoir increases and reaches its maximum value, the regulating supply valve closes, and no more air flows into the equalizing reservoir. Recall that the motion of the relay valve diaphragm depends on the pressure  $P_{1,1}$  of the relay valve outer chamber which is connected to the equalizing reservoir which has the

pressure  $P_{eq}$ . As  $P_{1,1}$  reaches its maximum value, the relay supply valve closes; and the air no longer flows from the main reservoir to the intermediate chamber of the relay valve.

7. When the relay supply valve closes,  $A_{1,6} = 0$ , and Eq. 4.57 shows that  $P_{1,3} = P_{bp}$ . This means that the pressure in the intermediate chamber will assume the value of the pressure in the brake pipe.

#### **4.9.2. Brake Application**

The steps of the algorithm in the case of service brake application can be summarized as follows:

1. For a given set of the train car body initial conditions and track geometry, the train nonlinear dynamic equations are formulated as a set of first order ordinary differential equations that can be solved using a standard numerical integration method. These equations are solved simultaneously with the air flow differential equations (Eq. 4.23), the equalizing reservoir pressure differential equation (Eq. 4.44), the intermediate chamber pressure differential equation (Eq. 4.50), and car control unit equations (discussed in Chapter 5) for a given set of initial conditions. The dynamic simulation of the train subject to different forces continues until brakes are applied.
2. Before the brake application, the brake system has the following conditions: the pressure  $P_{bp}$  in the brake pipe is equal to the pressure reached after the recharge; the velocity  $u$  in the brake pipe relative to the train is equal to zero (steady state, with the assumption of no leakage); the brake pipe cut-off valve is fully open, and

$P_{1,3} \approx P_{bp}$ . The pressure  $P_{eq}$  of the equalizing reservoir is assumed to be equal to the pressure  $P_{1,3}$  of the intermediate chamber.

3. When the handle is moved towards the application position, the exhaust valve of the regulating valve is opened. Depending on the value of  $X_{REG}$  defined in Section 4.6, Eq. 4.44 given by  $\frac{dP_{eq}}{dt} = \frac{R_g \Theta}{V_{eq}} \left( \frac{dm_{2,1}}{dt} - \frac{dm_{1,1}}{dt} \right)$  can be solved with the train differential equations to evaluate the equalizing reservoir pressure  $P_{eq}$  using the procedure described in the case of the brake release except for the initial condition and the use of the exhaust valve parameters instead of those of the supply valve. The initial condition for this first order ordinary differential equation is  $P_{eq} = P_{1,3}$ . Note also that in the simplified model  $\dot{m}_{1,1} = 0$ .
4. When the pressure  $P_{eq}$  is sufficiently low, the relay exhaust valve starts opening, letting the air flow from the brake pipe to the intermediate chamber through the brake pipe cut-off valve and then to the atmosphere through the exhaust valve. The exhaust valve area which is function of  $D_p = P_{eq} - P_{1,3}$  is defined in Eq. 16 of the appendix. If the simplified model is used, the pressure  $P_{1,3}$  starts to decrease according to the equation  $P_{1,3} = \sqrt{(P_{bp}^2 A_{3,3}^2 + P_a^2 A_{EX}^2) / (A_{3,3}^2 + A_{EX}^2)}$  (Eq. 4.57), as described in the appendix. During this process, the brake pipe cut-off valve remains fully open, that is,  $A_{3,3} = C_2$  as shown in the appendix by Eq. 9.

5. Using the current values of  $P_{1,3}$  and  $A_{3,3}$ , the mass flow rate of Eq. 4.52 is used to determine  $\dot{m}_{1,4}$  which is used in the brake pipe air flow equations. The pipe pressure reduction activates the brake application mode of the car control units and this can result in brake force application on the car wheels.
6. As the pressure  $P_{1,3}$  continues to decrease, the exhaust valve closes. The brake application process, thus, ends with the relay supply valve closed and with the brake pipe cut-off valve fully open. The value of the pressure  $P_{1,3}$  that determines the closing of the exhaust valve is controlled by the regulating valve in a similar manner as in the case of the brake release; as  $X_{REG}$  reaches a specified known value,  $P_{eq}$  decreases reaching its minimum value, the regulating exhaust valve closes. The minimum value of  $P_{eq}$  corresponds to a minimum value of the pressure  $P_{1,1}$  that controls the relay exhaust valve closing.
7. When the relay exhaust valve closes,  $A_{EX} = 0$ , and Eq. 4.57 shows that  $P_{1,3} = P_{bp}$ . This means that the pressure in the intermediate chamber will assume the value of the pressure in the brake pipe.

Since the right hand side of Eq. 4.57 also depends on the pressure  $P_{1,3}$ , this pressure can be obtained by solving iteratively the nonlinear equation or can be calculated using the values of  $P_{bp}$  and  $A_{EX}$  from the previous time step. The value of  $A_{EX}$  from the previous step is updated with the new value of  $P_{1,3}$  as described in the appendix.

It is important to point out that while in the model developed in this study the above-mentioned steps are valid for both the service and emergency brake application modes, in the emergency mode, the brake pipe air vents to atmosphere not only through the brake pipe cut-off valve but also through the emergency portion of the CCU. Furthermore, it should be mentioned that, in order to include the car control unit model in the cases explained above, the time derivative of the pressures associated with the car control units have to be integrated with the locomotive valve, the brake pipe, and the train dynamic equations. These parameters are introduced and discussed in Chapter 5.

#### **4.10. Concluding Remarks**

The objective of this work is to integrate an air brake model with a nonlinear train dynamic model developed using the trajectory coordinates. To this end, an air brake model that includes three main parts; the automatic brake valve, the brake pipe, and the car control unit; was developed. In this study, these three main valves of the locomotive 26C automatic brake valve; the regulating valve, the relay valve, and the brake cut-off valve; were considered. The general equations governing fluid behavior, including the continuity and the momentum equations, were used to develop the brake pipe air flow model. Using the assumption of one-dimensional flow, one can obtain two first order partial differential equations expressed in terms of the pressure and velocity. Using the finite element method, the two partial differential equations were converted to a system of first order ordinary differential equations with a constant coefficient matrix. The two main scenarios that describe brake release and application were discussed and the computational algorithms for the simulation of these scenarios were presented. In Chapter 5, the car control unit and its operation during the brake release and application are discussed. That

chapter also includes numerical results that demonstrate the use of the proposed formulations and algorithms and their implementation in the computer program **ATTIF** (**A**nalysis of **T**rain/**T**rack **I**nteraction **F**orces) developed to study the train longitudinal forces.

## 5. AIR BRAKE COMPUTER IMPLEMENTATION

As discussed in Chapter 4, the air brake system of a freight train consists of three main units; the locomotive control unit, the brake pipe, and the car control unit (CCU). The locomotive control unit, which is located in the controlling locomotive at the brake pipe head-end, controls the brake pipe pressure through the locomotive automatic brake valve. The brake pipe that connects the locomotive automatic brake valve to the CCUs transmits the brake operation signal as well as the pressurized air to the car control units. A common train brake has one locomotive control unit and one brake pipe. The number of the car control units, however, depends on the number of cars in the train. The CCU consists of different pneumatic and mechanical components that control the brake application or release. These brake modes depend on the brake pipe pressure and the automatic brake valve handle position that is controlled by the train operator.

As discussed in Chapter 4, the goal in this investigation is to integrate the train nonlinear dynamic model developed using the trajectory coordinate formulation (Shabana et al., 2008) with the air brake model. The air brake model developed in this study consists of three units previously mentioned; the automatic brake valve that is assumed to be the 26C valve, the brake pipe that is assumed to be a continuous air transmission line that passes through all train cars, and the CCU that is installed on each car and is connected to the brake pipe by the branch pipe. The 26C automatic brake valve consists of several parts. In this research, three main valves of the automatic brake valve are considered and modeled (See Chapter 4); namely the *regulating*, *relay*, and *brake pipe cut-off* valves. The regulating valve that is directly controlled by the train operator via the automatic brake handle adjusts the pressure inside a reservoir called the equalizing reservoir. The relay valve has several chambers that are used to control the pressure

inside a chamber referred to as the *intermediate chamber*. The brake pipe cut-off valve is the valve through which air flows to or from the brake pipe, and it is the connection between the intermediate chamber and the brake pipe. The brake pipe air flow is modeled using the continuity and the momentum equations with the assumption of one-dimensional isothermal flow (John and Keith, 2006; White, 2008). The resulting two coupled partial differential equations are expressed in terms of the air velocity, pressure and their derivatives with respect to time and with respect to the longitudinal coordinate along the pipe. These equations are discretized using a linear finite element approach in order to obtain a set of first order ordinary differential equations. The unknown dependent variables are selected in such a way that allowed having a constant coefficient matrix. In order to further improve the efficiency of the computational procedure, simplifications are made in the automatic brake valve and the car control unit models. However, the analysis presented in Chapter 4 does not cover the car control unit which is one of main components of a train air brake system.

A CCU, which is installed on each train car, consists of different pneumatic and mechanical components. The CCU model considered in this chapter is assumed to have the basic components; the *control valve*, the *auxiliary reservoir*, the *brake cylinder*, the *brake rigging*, and the *brake shoes* (Railway Technical Web Pages, 2010), as well as a component called the *emergency reservoir* that is only used in the case of emergency brake application. The control valve acts as a pressure sensor that operates based on the local brake pipe pressure (the pressure at the control valve connection point with the brake pipe) and its time rate of change. The control valve function is to connect different CCU parts and to control the air transfer between them. In the model used in this investigation, it is assumed that the control valve has the *triple valve* that

controls the communication between the brake pipe, the auxiliary reservoir, the brake cylinder, and the atmosphere. Furthermore, the emergency portion of the CCU controls the communication between the emergency reservoir and the brake cylinder. The auxiliary reservoir, the most frequently used CCU storage reservoir, supplies the pressurized air required for service brake application. The brake cylinder is the component where the pressurized air can push the cylinder piston to produce an axial force required to apply the brake. The brake rigging is a leverage mechanism that transmits the piston axial force and converts it to a normal force applied to the brake shoes on the car wheels; it is also used to magnify the normal brake shoe force magnitude. The brake shoe is the part that is pressed against the wheel by the normal force to produce the frictional brake retarding force. The magnitude of the normal brake force produced on the brake shoes depends on the automatic brake valve handle position that is controlled by the train operator. In this study, it is assumed that the train operator can apply three main brake operation modes; the *brake release*, *service brake*, and *emergency brake* modes. In the case of the emergency brake mode, both the emergency reservoir and the auxiliary reservoir are connected to the brake cylinder to produce higher brake cylinder pressure. CCU's, in general, have more complicated fluid networks, which can result in other modes such as quick service mode that is not considered here. As it will be shown, the CCU studied in this chapter has the capability of acceptable modeling of various brake scenarios.

While more studies on modeling train air brake can be found in the literature (Bansiter, 1979; Limbert, 1991; Gauthier, 1977; Kreel, 1979; Wetenkamp, 1974, Wright, 1978), this chapter focuses on the CCU operation modes and the interaction between CCU components. The automatic brake valve and brake pipe models were developed in Chapter 4. A mathematical

model is developed for the CCU components, including the auxiliary reservoir, the emergency reservoir, and the brake cylinder. For different operation modes of the brake, the air flow between different CCU sections is modeled. This leads to a set of first order ordinary differential equations that are combined with the automatic brake valve and the brake pipe differential equations in order to define the air brake mathematical model. This model will be integrated with the nonlinear train dynamic model that employs the trajectory coordinates. The air brake/train differential equations are used in dynamic simulation scenarios of trains that have different numbers of cars, initial conditions, track geometry, and brake application modes. The numerical results, obtained using the integrated air brake/train model, are used to study the train longitudinal dynamic motion and forces. For each simulation scenario, the effects of the variations of air brake and train dynamics parameters are investigated. In order to validate the model developed in this study, the obtained numerical results are compared with experimental results published in the literature. The comparison show a good agreement between the results predicted using computer simulation and the experimental results.

### **5.1. Car Control Unit (CCU)**

In addition to the brake pipe and the automatic brake valve, the train air brake system has another essential unit called the *car control unit* (CCU). While a train air brake has generally one brake pipe passing through all the cars and one automatic brake valve, a CCU is installed on each car. The number of the control units in a train air brake system, therefore, depends on the number of the cars in the train. The CCU consists of several mechanical and pneumatic components that are connected to one another. The brake pipe provides the pressurized air and the pneumatic operation signal to the cars, while the brake force is produced using the CCU components. The

CCU components may vary depending on the car type and the purpose for which these cars are used. The components of the CCU studied in this chapter are shown in Fig. 47. Figure 47 only shows a schematic representation of the CCU components while in reality the configuration of the components can be different. For instance, the auxiliary and emergency reservoirs are often welded one within the other, but here, for the sake of better distinction, they are shown separated on either side of the control valve.

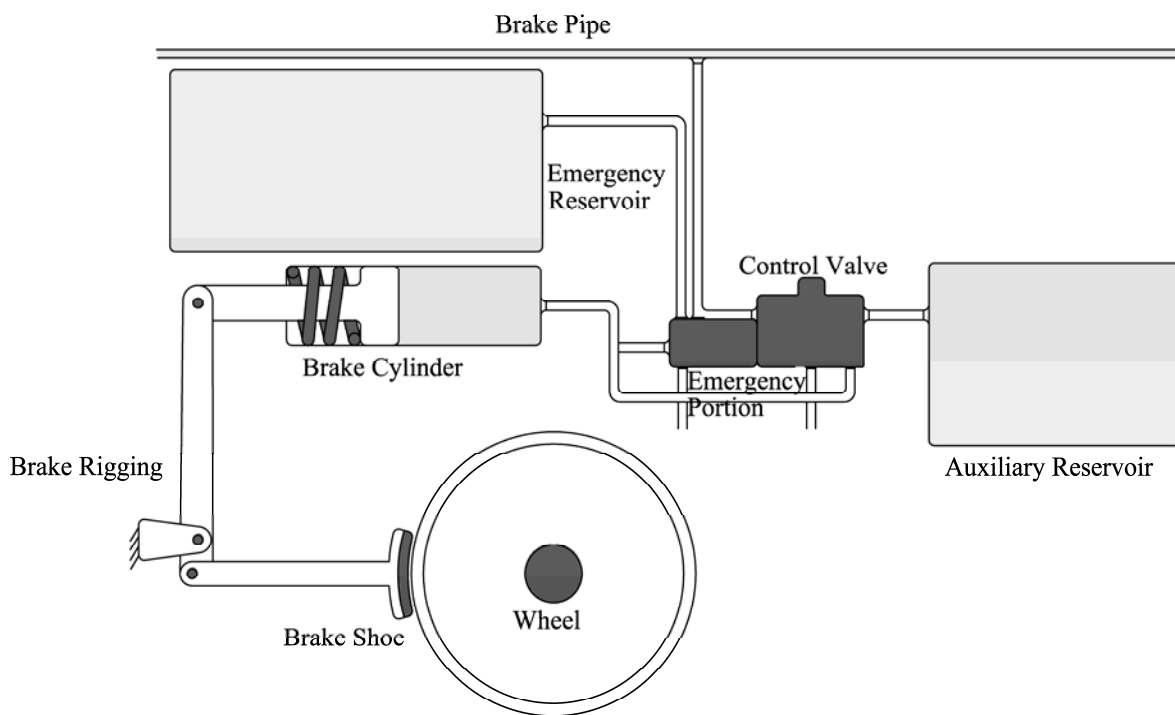


Figure 47. Car control unit components

### 5.1.1. Control Valve

One of the main CCU parts is the control valve. The car control valve is, in fact, a sensor that responds to the changes in the brake pipe pressure. The CCU valve controls the compressed air transfer between the brake pipe, the storage reservoirs (auxiliary and emergency), the brake

cylinder, and the atmosphere. While several control valve designs are used by railroad industry (Kratville, 1997), the triple valve (Sanborn et al., 2007) will be used in this study. The number and the types of reservoirs connected to the control valve depend on the desired valve capabilities of handling different brake operations. As shown in Fig. 47, the triple valve used in this study is connected pneumatically to three CCU components; the auxiliary reservoir, the emergency reservoir, and the brake cylinder.

### **5.1.2. Auxiliary and Emergency Reservoirs**

The auxiliary reservoir is the CCU component that provides the pressurized air required for service brake application. The auxiliary reservoir, in other words, is one of the main CCU compressed air storage components where the air coming from the brake pipe is stored. The compressed air transfers from the brake pipe to the auxiliary reservoir through the CCU control valve during brake release/recharge. Similarly, the emergency reservoir is the other main air storage component that provides additional compressed air for emergency brake application, when occasionally needed.

### **5.1.3. Brake Cylinder**

The brake cylinder is the CCU component that transmits the force required for brake application to the brake rigging and the brake shoes. As shown in Fig. 47, inside the brake cylinder, there is a piston connected to a spring used to return the piston to its release position during the brake recharge/release. In the CCU model developed in this study, the brake cylinder is filled with the pressurized air coming from the auxiliary reservoir during service brake; while during the emergency brake, it is filled from the air of both the emergency and auxiliary reservoirs. This

pressure pushes the piston against the spring producing braking force that is transmitted to the wheels through the brake rigging and the brake shoes.

#### **5.1.4. Brake Rigging**

The brake rigging is a common term used to refer to the mechanical system that consists of rods, levers, and connecting elements. The function of the brake rigging is the magnification of the brake cylinder force and the transmission of this force to the brake shoes. Other names such as *foundation brake gear* or *truck rigging* are also used in railroad industry to refer to different types of brake rigging (Kratville, 1997).

#### **5.1.5. Brake Shoe**

The car brake shoe, usually made of cast iron, sintered iron, or composite materials, produces frictional braking force when pressed against the wheel tread during brake application. During brake recharge/release, the brake shoe normal forces are relieved on the wheels when the air in the brake cylinder is vented.

### **5.2. CCU Operation**

The air transferred from the brake pipe to the CCU reservoirs or from the brake cylinder to the atmosphere has to pass through the car control valve. The function of the control valve is to control airflow between the brake pipe, the brake cylinder(s), the auxiliary and emergency reservoirs, and the atmosphere. In order to control airflow between different parts of the brake system, the control valve functions based on the current air pressure of the brake pipe and its time rate change. The triple valve studied in this research has an internal valve called the *slide valve* as shown in Fig. 47. The slide valve can have three positions; the *brake application*, *brake release*, and *lap* positions, explained below.

### 5.2.1. Brake Application Position

During service brake application, the brake pipe pressure begins to drop starting from the brake pipe cut-off valve that is usually on the controlling locomotive at the head-end of the train. As the brake pipe pressure falls below the auxiliary reservoir pressure, the slide valve of the control valve moves to the left as shown in Fig. 48 (the emergency components of the CCU are not shown since they are not active in this mode). The valve movement prevents the airflow between the brake pipe and CCU and closes the exhaust port of the control valve. The air then flows from the auxiliary reservoir to the car brake cylinder, pushing the piston to the left and producing the brake cylinder force that is magnified and transmitted to the car wheels through the brake rigging levers and shoes.

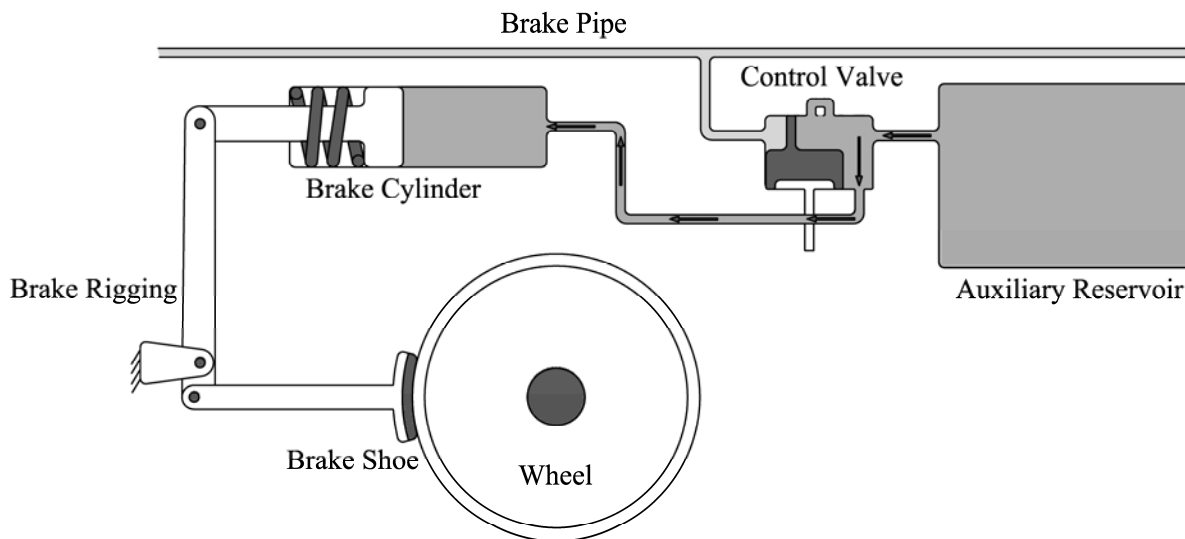


Figure 48. The slide valve in the brake application position

This process also takes place during emergency brake. However, in the case of service brake, there is no air flow from the brake pipe to CCU or the atmosphere, while during the

emergency brake, in addition to the above-mentioned operations, the emergency portion of CCU directly vents the brake pipe air to the atmosphere. In other words, during emergency brake, the emergency portion of CCU contributes to rapidly venting the brake pipe air by opening the CCU emergency vent valve that directly vents the brake pipe air to the atmosphere. In the case of emergency brake, furthermore, the emergency and auxiliary reservoirs are both connected to the brake cylinder, which results in a nominally 20% higher brake cylinder pressure at equalization.

### **5.2.2. Release Position**

When the automatic brake valve handle is in the release position, the brake pipe pressure increases starting at the cut-off valve (usually the head-end controlling locomotive). As the pipe pressure continues to increase, it eventually exceeds the pressure of the CCU auxiliary reservoir, causing the slide valve to move to the right allowing the brake pipe air to flow to the auxiliary reservoir. The airflow to the auxiliary reservoir continues until its pressure becomes the same as the brake pipe pressure. This slide valve movement also disconnects the brake cylinder and the auxiliary reservoir, opening the valve exhaust port to allow the pressurized air inside the cylinder to vent to the atmosphere as shown in Fig. 49. In this case, the compressed cylinder spring pushes back the piston to its release position and in the meantime the brake shoes are relieved from the car wheels. Once all the auxiliary reservoirs are fully recharged, the air transfer to the brake pipe stops (with the assumption of no brake pipe leakage, other than flows to the branch pipes).

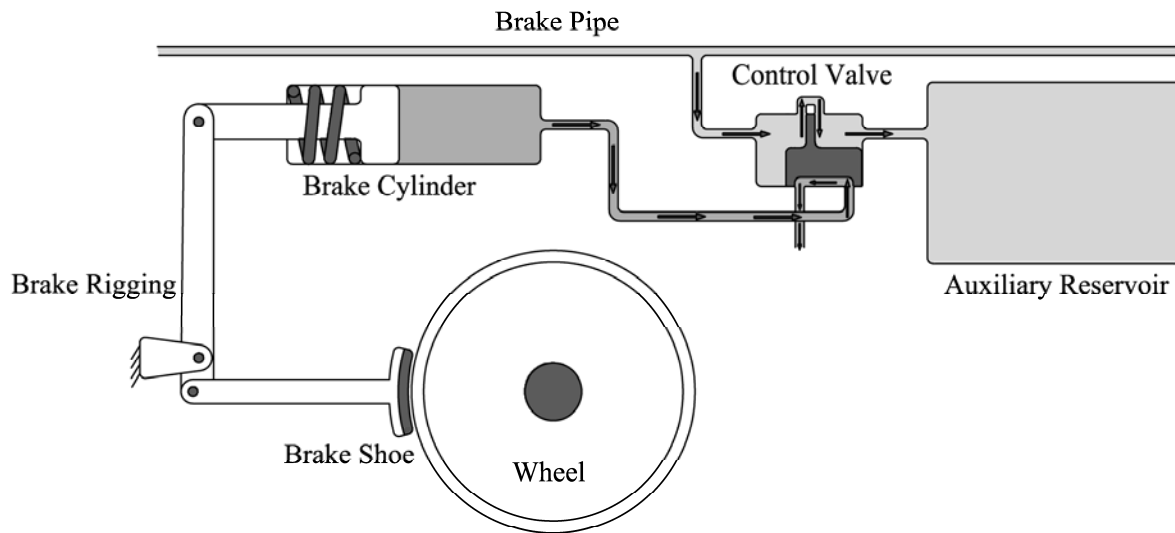


Figure 49. The slide valve in the brake release position

### 5.2.3. Lap Position

The lap position is an intermediate position for the slide valve. When the brake pipe pressure stops falling during service brake application, the lap mode can be activated. Because of the auxiliary reservoir airflow to the brake cylinder, the auxiliary reservoir pressure gradually decreases and eventually it becomes equal to the brake pipe pressure. At this moment, as shown in Fig. 50, the slide valve is moved to an intermediate position such that it closes all the connections between the brake pipe, the auxiliary reservoir, and the brake cylinder. As in the case of the brake application mode, the exhaust port also remains closed. As a consequence, the brake cylinder pressure remains constant, leading to a constant brake force application.

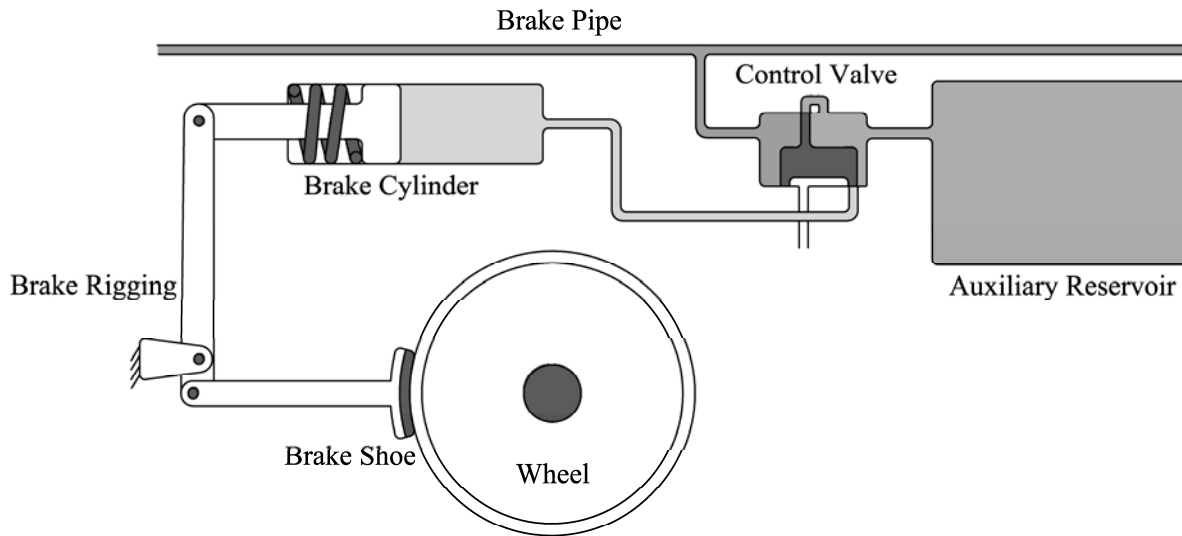


Figure 50. The slide valve in the lap position

### 5.3. CCU Mathematical Model

The CCU mathematical model developed in this section will be integrated with the brake pipe and train models discussed in Chapter 4. Figure 51 shows the CCU parameters of Car  $i$  ( $i$  is the car number in the train starting from the brake pipe head-end). The CCU parameters in different brake modes as well as the brake force are calculated as described below.

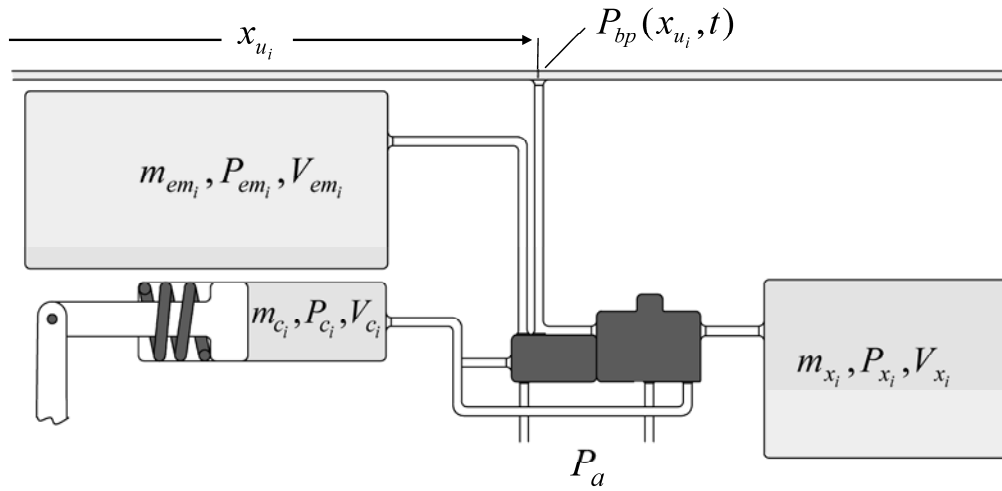


Figure 51. The parameters associated with the control unit of car  $i$

### 5.3.1. Mass Flow Rates

The airflow between the brake pipe, the atmosphere, and the CCU components depends on the local brake pipe pressure and its time rate. All pressures in the formulae that follow will be expressed in absolute pressure. Similar to the method used to calculate the mass flow rate in (Abdol-Hamid, 1986), the *average density approach* will be used in this section (Abdol-Hamid, 1986). In this chapter, the total mass flow rate to component  $e$  is denoted by  $dm_e/dt = \dot{m}_e$ , while the mass flow rate from component  $f$  to component  $e$  as shown in Fig. 52, is denoted by  $\dot{m}_{e-f}$  calculated using the following formula:

$$\dot{m}_{e-f} = \frac{dm_{e-f}}{dt} = -\dot{m}_{f-e} = 0.6A_{e-f}P_e\sqrt{\frac{|r^2-1|}{R_g\Theta}}\frac{|r-1|}{r-1} \quad (5.1)$$

where  $P_e$  is the pressure inside component  $e$ ,  $r$  is the pressure ratio ( $r = P_f/P_e$ ),  $R_g$  and  $\Theta$  are the gas universal constant and gas temperature, respectively, and  $A_{e-f}$  is the equivalent area

of the two areas connecting the two components (i.e.  $A_e$  and  $A_f$ ). With the assumption of a series connection,  $A_{e-f}$  can be calculated as follows (Abdol-Hamid, 1986):

$$A_{e-f} = \frac{1}{\sqrt{\frac{1}{A_e^2} + \frac{1}{A_f^2}}} = \frac{A_e A_f}{\sqrt{A_e^2 + A_f^2}} \quad (5.2)$$

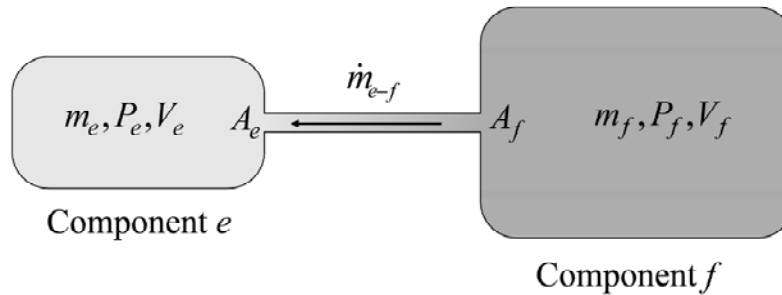


Figure 52. The mass flow rate between components  $e$  and  $f$

While Eq. 5.1 is based on the assumption that the two components, schematically shown in Fig. 52, have constant volumes, this equation is applicable to any CCU part; one only needs to change the subscript that refers to the CCU component. In this chapter, the letters  $bp$ ,  $x$ ,  $c$ ,  $u$ ,  $em$ , and  $a$  denote, respectively, the brake pipe, the auxiliary reservoir, the brake cylinder, the control unit, emergency reservoir, and the atmosphere. The schematic of the airflow between the above-mentioned parts is shown in Fig. 53.

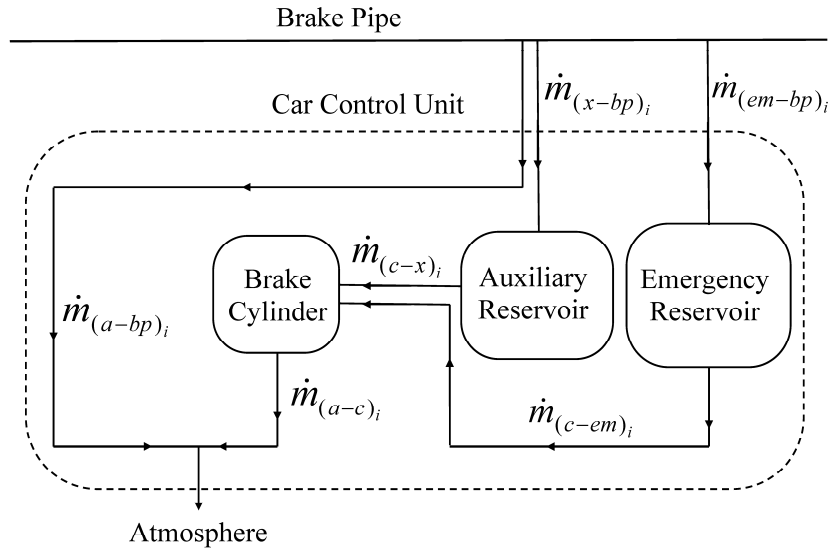


Figure 53. The mass flow rate between the brake pipe, atmosphere, and CCU components

Using Eq. 5.1, the air flow to the auxiliary and emergency reservoirs of Car  $i$  from the brake pipe ( $e = x, em$  and  $f = bp$ ) is obtained from the following equation:

$$\begin{cases} \dot{m}_{(x-bp)_i} = 0.6 A_{(x-bp)_i} P_{x_i} \sqrt{\frac{|r_i^2 - 1|}{R_g \Theta}} \frac{|r_i - 1|}{r_i - 1} & \text{(a)} \\ \dot{m}_{(em-bp)_i} = 0.6 A_{(em-bp)_i} P_{em_i} \sqrt{\frac{|r_i^2 - 1|}{R_g \Theta}} \frac{|r_i - 1|}{r_i - 1} & \text{(b)} \end{cases} \quad (5.3)$$

where  $r_i = P_{bp}(x_{u_i}, t) / P_{e_i}$  ( $e = x, em$ ),  $P_{bp}(x_{u_i}, t)$  is the local brake pipe pressure that is function of the location of the CCU connection point with the pipe  $x_{u_i}$  and time  $t$ ,  $A_{(x-bp)_i}$  and  $A_{(em-bp)_i}$  are the equivalent areas connecting the pertinent components and are calculated from Eq. 5.2. Similarly, the air flow from the auxiliary and emergency reservoirs to the brake cylinder ( $e = c$  and  $f = x, em$ ) can be obtained from the following equation:

$$\left\{ \begin{array}{l} \dot{m}_{(c-x)_i} = 0.6 A_{(c-x)_i} P_{c_i} \sqrt{\frac{|r_i^2 - 1|}{R_g \Theta}} \frac{|r_i - 1|}{r_i - 1} \quad (a) \\ \dot{m}_{(c-em)_i} = 0.6 A_{(c-em)_i} P_{c_i} \sqrt{\frac{|r_i^2 - 1|}{R_g \Theta}} \frac{|r_i - 1|}{r_i - 1} \quad (b) \end{array} \right. \quad (5.4)$$

where  $r_i = P_{f_i} / P_{c_i}$  ( $f = x, em$ ),  $A_{(c-x)_i}$  and  $A_{(c-em)_i}$  are the equivalent of the connecting areas obtained from Eq. 5.2. In addition, the air vented to the atmosphere ( $e = a$ ) from the brake cylinder ( $f = c$ ) or from the brake pipe ( $f = bp$ ) is governed by the following equation:

$$\left\{ \begin{array}{l} \dot{m}_{(a-c)_i} = 0.6 A_{(a-c)_i} P_a \sqrt{\frac{|r_i^2 - 1|}{R_g \Theta}} \frac{|r_i - 1|}{r_i - 1} \quad (a) \\ \dot{m}_{(a-bp)_i} = 0.6 A_{(a-bp)_i} P_a \sqrt{\frac{|r_i^2 - 1|}{R_g \Theta}} \frac{|r_i - 1|}{r_i - 1} \quad (b) \end{array} \right. \quad (5.5)$$

where,  $r_i = P_{f_i} / P_a$  ( $f = bp, c$ ),  $A_{(a-c)_i}$  and  $A_{(a-bp)_i}$  are the equivalent areas of the pertinent components of car  $i$  that can also be calculated from Eq. 5.2.

### 5.3.2. Pressure Rates

In order to calculate the time rate of the pressure inside CCU component  $e$ , the following universal gas law is employed (John and Keith, 2006; White, 2008):

$$P_e V_e = m_e R_g \Theta_e \quad (5.6)$$

where  $P_e$  is the gas pressure (N/m<sup>2</sup>),  $V_e$  is the volume (m<sup>3</sup>),  $m_e$  is the gas mass (Kg),  $R_g$  is the gas constant (J/(Kg °K)), and  $\Theta_e$  is the temperature (°K), which is assumed to be the same as the temperature of the brake pipe air (i.e.  $\Theta_e = \Theta$ ). Assuming that all the processes taking place in the CCU are isothermal ( $\Theta$  is constant), one can differentiate Eq. 5.6 with respect to time to obtain the time rate of the pressure as

$$\frac{dP_e}{dt} = \frac{1}{V_e} \left( R_g \Theta \frac{dm_e}{dt} - P_e \frac{dV_e}{dt} \right) \quad (5.7)$$

In this equation, it is assumed that pressure is evenly distributed inside component  $e$ . Equation 5.7 can be used to determine the time rate of the auxiliary reservoir pressure of car  $i$ . Using the fact that the volumes of the auxiliary and emergency reservoirs are constant, one can write as

$$\left\{ \begin{aligned} \frac{dP_{x_i}}{dt} &= \frac{1}{V_{x_i}} \left( R_g \Theta \frac{dm_{x_i}}{dt} - P_{x_i} \frac{dV_{x_i}}{dt} \right) = \frac{R_g \Theta}{V_{x_i}} \dot{m}_{x_i} & (a) \\ \frac{dP_{em_i}}{dt} &= \frac{1}{V_{em_i}} \left( R_g \Theta \frac{dm_{em_i}}{dt} - P_{em_i} \frac{dV_{em_i}}{dt} \right) = \frac{R_g \Theta}{V_{em_i}} \dot{m}_{em_i} & (b) \end{aligned} \right. \quad (5.8)$$

Similarly, one can use Eq. 5.7 to calculate the time rate of the brake cylinder pressure as

$$\frac{dP_{c_i}}{dt} = \frac{1}{V_{c_i}} \left( R_g \Theta \frac{dm_{c_i}}{dt} - P_{c_i} \frac{dV_{c_i}}{dt} \right) \quad (5.9)$$

Unlike the auxiliary reservoir, the brake cylinder, in general, does not have a constant volume because of the piston movement. However, during the brake shoe force application, one can assume that the cylinder volume remains constant.

### **5.3.3. The Car Brake Parameters in Different Brake Modes**

The CCU parameters discussed in the previous sections, depending on the brake mode, can be function of time, the car location in the train, and other air brake parameters. The variation range of these parameters as well as the relationship between them is presented in Table III.

Table III. The variation range of the parameters associated with car  $i$ 

Parameter	Brake Application Mode	Brake Release Mode
$\dot{m}_{(x-bp)_i}$	0	$\dot{m}_{(x-bp)_i}(P_{bp}(x_{u_i}, t), P_{x_i}) \geq 0$
$\dot{m}_{(bp-a)_i}$	$\begin{cases} 0^* \\ \dot{m}_{(bp-a)_i}(P_{bp}(x_{u_i}, t), P_a) \leq 0^{**} \end{cases}$	0
$\dot{m}_{(c-x)_i}$	$\dot{m}_{(c-x)_i}(P_{c_i}, P_{x_i}) \geq 0$	0
$\dot{m}_{(c-em)_i}$	$\begin{cases} 0^* \\ \dot{m}_{(c-em)_i}(P_{c_i}, P_{em_i}) \geq 0^{**} \end{cases}$	0
$\dot{m}_{(c-a)_i}$	0	$\dot{m}_{(c-a)_i}(P_{c_i}, P_a) \leq 0$
$\dot{P}_{x_i}$	$\dot{P}_{x_i}(\dot{m}_{(c-x)_i}) \leq 0$	$\dot{P}_{x_i}(\dot{m}_{(x-bp)_i}) \geq 0$
$\dot{P}_{c_i}$	$\dot{P}_{c_i}(\dot{m}_{(c-x)_i}) \geq 0$	$\dot{P}_{c_i}(\dot{m}_{(c-a)_i}) \leq 0$
$\dot{P}_{em_i}$	$\begin{cases} 0^* \\ \dot{P}_{em_i}(\dot{m}_{(c-em)_i}) \leq 0^{**} \end{cases}$	$\begin{cases} 0 \\ \dot{P}_{em_i}(\dot{m}_{(bp-em)_i}) \geq 0^\dagger \end{cases}$
$\dot{m}_{x_i}$	$-\dot{m}_{(c-x)_i}(P_{c_i}, P_{x_i}) \leq 0$	$\dot{m}_{(x-bp)_i}(P_{bp}(x_{u_i}, t), P_{x_i}) \geq 0$
$\dot{m}_{c_i}$	$\dot{m}_{(c-x)_i}(P_{c_i}, P_{x_i}) \geq 0$	$\dot{m}_{(c-a)_i}(P_{c_i}, P_a) \leq 0$
$\dot{m}_{em_i}$	$\begin{cases} 0^* \\ -\dot{m}_{(c-em)_i}(P_{c_i}, P_{em_i}) \leq 0^{**} \end{cases}$	$\begin{cases} 0 \\ \dot{m}_{(em-bp)_i}(P_{bp}(x_{u_i}, t), P_{em_i}) \geq 0^\dagger \end{cases}$
$\dot{m}_{bp_i}$	$\begin{cases} 0^* \\ \dot{m}_{(bp-a)_i}(P_{bp}(x_{u_i}, t), P_a) \leq 0^{**} \end{cases}$	$-\dot{m}_{(x-bp)_i}(P_{bp}(x_{u_i}, t), P_{x_i}) \leq 0$

\* For service mode

\*\* For emergency mode

† For release after emergency brake

In this table,  $\dot{m}_{bp_i}$  is the rate of the pipe mass flow through the CCU of car  $i$  to its auxiliary reservoir, to emergency reservoir, or to the atmosphere. In the model developed in this study,  $\dot{m}_{bp_i}$  is the parameter that links the brake pipe FE model to the CCU of car  $i$ . In order to include the effect of  $\dot{m}_{bp_i}$  in the FE model, the element where the car control valve is connected to the brake pipe is determined. Then,  $\dot{m}_{bp_i}$  is distributed between the two nodes of the element and is considered as the element leakage in the equations presented in Chapter 4.

#### 5.3.4. Brake Force

In order to determine the brake force, the brake cylinder piston axial force has to be calculated. In general, in order to obtain the piston displacement  $u_{p_i}$  and the brake cylinder pressure, a set of two coupled differential equations needs to be solved; the piston equation of motion and the time rate of the cylinder pressure equation. These two equations are

$$\left. \begin{aligned} m_{p_i} \frac{d^2 u_{p_i}(t)}{dt^2} &= (P_{c_i}(t) - P_a) S_{p_i} - K_{c_i} u_{p_i}(t) - f_{f_i} - F_{p_i} h(u_{p_i}(t) - u_{con_i}) \\ \frac{dP_{c_i}(t)}{dt} &= \frac{1}{V_{0_i} + S_{c_i} u_{p_i}(t)} \left( R_g \Theta \frac{dm_{c_i}(t)}{dt} - P_{c_i}(t) S_{c_i} \frac{du_{p_i}(t)}{dt} \right) \end{aligned} \right\} \quad (5.10)$$

where  $m_{p_i}$  is the piston mass,  $S_{p_i}$  is the piston cross-section area,  $K_{c_i}$  is the stiffness constant of the cylinder spring,  $f_{f_i}$  is the friction force,  $F_{p_i}$  is the axial force of the piston,  $u_{con_i}$  is the piston displacement when the brake shoes contact the wheels,  $h(u_{p_i})$  is the Heaviside step function,  $V_{0_i}$  is the initial volume of the brake cylinder,  $S_{c_i}$  is the cross-section area of the cylinder that is assumed to be approximately equal to that of the piston (i.e.  $S_{c_i} \cong S_{p_i}$ ), and  $\dot{m}_{c_i}(t)$  is the cylinder mass flow rate that is obtained as presented in Table III, depending on the brake mode.

After the brake shoes contact the wheels, one can assume that  $d^2u_{p_i}(t)/dt^2 \cong du_{p_i}(t)/dt \approx 0$ , and  $u_{p_i}(t) \cong u_{con_i}$ ,  $u_{p_i}(t) > u_{con_i}$  which leads to  $h(u_{p_i}(t) - u_{con_i}) = 1$ .

Using these assumptions, the piston axial force can be calculated as

$$F_{p_i}(t) = (P_{c_i}(t) - P_a)S_{p_i} - K_{c_i}u_{con_i} - f_{f_i} \quad (5.11)$$

Furthermore, with the assumption of small piston acceleration and velocity, when  $u_{p_i}(t) \leq u_{con_i}$ , one can obtain the spring displacement using the following equation:

$$u_{p_i}(t) = ((P_{c_i}(t) - P_a)S_{p_i} - f_{f_i})/K_{c_i} \quad (5.12)$$

It should be noted that an ideal brake rigging transfers the entire normal force to the wheels without any loss. In reality, however, this is not the case. In other words, some fraction of the force is used to move the brake rigging components and to overcome the friction in its joints and connections. In order to take into account such an energy loss without considering the complicated equations of motion, joint constraints, etc of the brake rigging, a rigging efficiency can be used when the brake force is calculated.

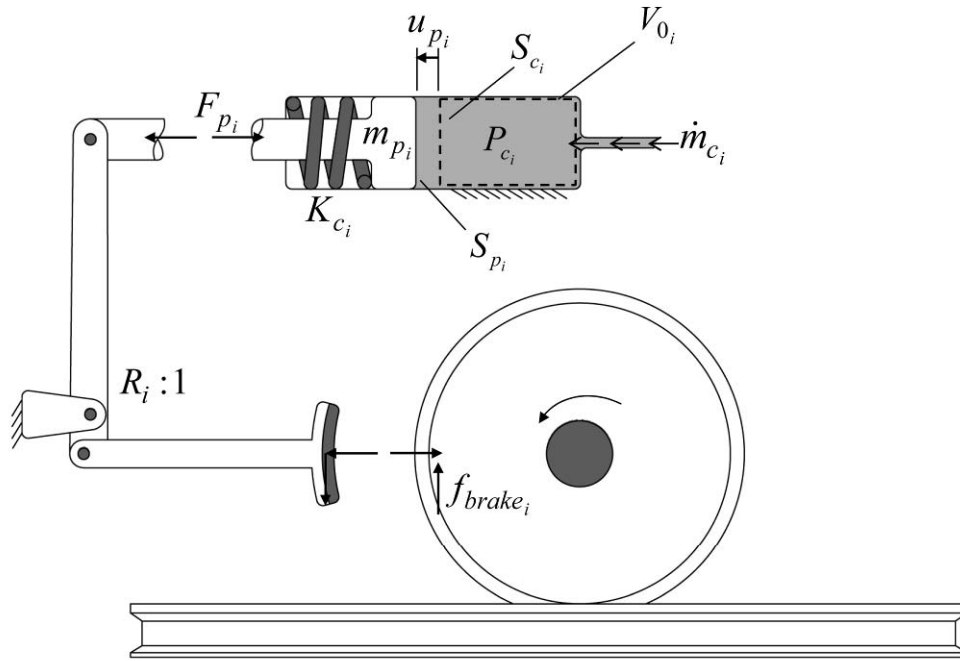


Figure 54. The brake force applied on a car wheel

Figure 54 shows the schematic of the brake force applied on one car wheel. Because of the rod and lever arrangement of the brake rigging, the brake force is often distributed among several car wheels, which are not shown in Fig. 54. If it is assumed that each car has one brake cylinder and the normal force resulting from the brake cylinder pressure is equally distributed to all brake shoes, the frictional tangential or retarding brake force for each shoe can be calculated as follows (Sanborn et al., 2007):

$$f_{brake_i}(t) = \eta_i \frac{\mu_i}{N_{s_i}} R_i F_{p_i}(t) = \eta_i \frac{\mu_i}{N_{s_i}} R_i \left\{ (P_{c_i}(t) - P_a) S_{p_i} - K_{c_i} u_{con-i} - f_{f_i} \right\} \quad (5.13)$$

where  $\eta_i$  is the rigging efficiency (which is often considered as a function of the brake cylinder pressure),  $\mu_i$  is the friction coefficient between the wheel tread and the brake shoe,  $R_i$  is the brake rigging leverage ratio, and  $N_{s_i}$  is the total number of the brake shoes of the car. The brake

shoe retarding friction force obtained from Eq. 5.13 enters into the formulation of the generalized forces acting on the car.

#### 5.4. Integration of the Air Brake and Train Dynamics

In this investigation, the train nonlinear dynamic equations are developed using the trajectory coordinates in order to allow for a systematic reduction of the car degrees of freedom when the train longitudinal dynamics is considered. Two coordinate systems are defined for each body; the centroidal body coordinate system  $X^{ir}Y^{ir}Z^{ir}$ , and the body/track coordinate system ( $X^{ti}Y^{ti}Z^{ti}$ ) shown in Fig. 55.

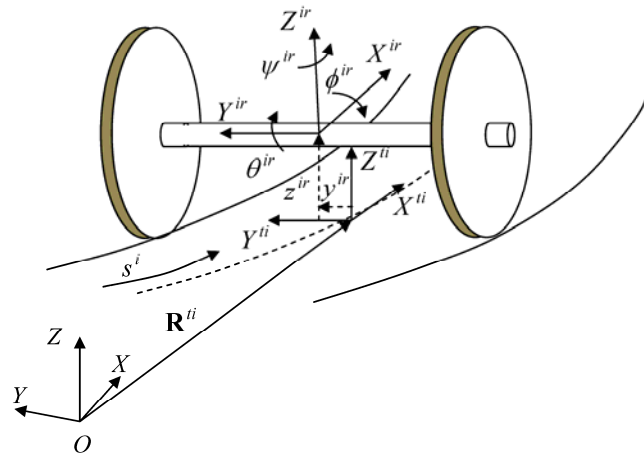


Figure 55. Trajectory coordinates

The orientation and the location of the origin of the body/track frame is a function of the distance travelled  $s_i$ . As shown in Fig. 55, the six trajectory coordinates for car  $i$  are

$$\mathbf{p}^i = [s^i \quad y^{ir} \quad z^{ir} \quad \psi^{ir} \quad \phi^{ir} \quad \theta^{ir}]^T \quad (5.14)$$

The Newton-Euler equations of body  $i$  can be written as

$$\begin{bmatrix} m^i \mathbf{I} & \mathbf{0} \\ \mathbf{0} & \bar{\mathbf{I}}_{\theta\theta}^i \end{bmatrix} \begin{bmatrix} \ddot{\mathbf{R}}^i \\ \ddot{\boldsymbol{\alpha}}^i \end{bmatrix} = \begin{bmatrix} \mathbf{F}_e^i \\ \bar{\mathbf{M}}_e^i - \bar{\boldsymbol{\omega}}^i \times (\bar{\mathbf{I}}_{\theta\theta}^i \bar{\boldsymbol{\omega}}^i) \end{bmatrix} \quad (5.15)$$

where  $m^i$  is the body mass,  $\ddot{\mathbf{R}}^i$  is the body global acceleration,  $\mathbf{F}_e^i$  is the applied external force defined in the global frame; while  $\bar{\mathbf{I}}_{\theta\theta}^i$  is the body inertia tensor,  $\ddot{\boldsymbol{\alpha}}^i$  is the body angular acceleration,  $\bar{\boldsymbol{\omega}}^i$  is the angular velocity, and  $\bar{\mathbf{M}}_e^i$  is the external moment, all defined in the body coordinate system. The left hand side of Eq. 5.15 can be expressed in terms of the trajectory accelerations as described in the literature (Shabana et al., 2008). The dynamic equations of motion expressed in terms of the trajectory coordinates can then be converted to a set of first order ordinary differential equations that can be solved simultaneously with the air brake model equations. Figure 56 shows a schematic diagram that explains the integration of the automatic brake valve, air brake pipe, CCU, and train dynamic models. Therefore, the following sets of equations are solved simultaneously:

$$\left. \begin{aligned}
 \mathbf{B}_{TD_{n \times n}} \dot{\mathbf{y}}_{TD_{n \times 1}} &= \mathbf{Q}_{brake_{n \times 1}} + \mathbf{Q}_{TD_{n \times 1}} \\
 \mathbf{M}_{pb_{m \times m}} \dot{\mathbf{p}}_{b_{m \times 1}} &= \mathbf{Q}_{L_{b_{m \times 1}}} + \mathbf{Q}_{P_{b_{m \times 1}}} \\
 \mathbf{M}_{qb_{m \times m}} \dot{\mathbf{q}}_{b_{m \times 1}} &= \mathbf{Q}_{q_{b_{m \times 1}}}, \dot{P}_{eq} = Q_{eq}, \dot{P}_{13} = Q_{13} \\
 \dot{\mathbf{p}}_{x_{N \times 1}} &= \mathbf{Q}_{x_{N \times 1}}, \dot{\mathbf{p}}_{c_{N \times 1}} = \mathbf{Q}_{c_{N \times 1}}, \dot{\mathbf{p}}_{em_{N \times 1}} = \mathbf{Q}_{em_{N \times 1}}
 \end{aligned} \right\} \quad (5.16)$$

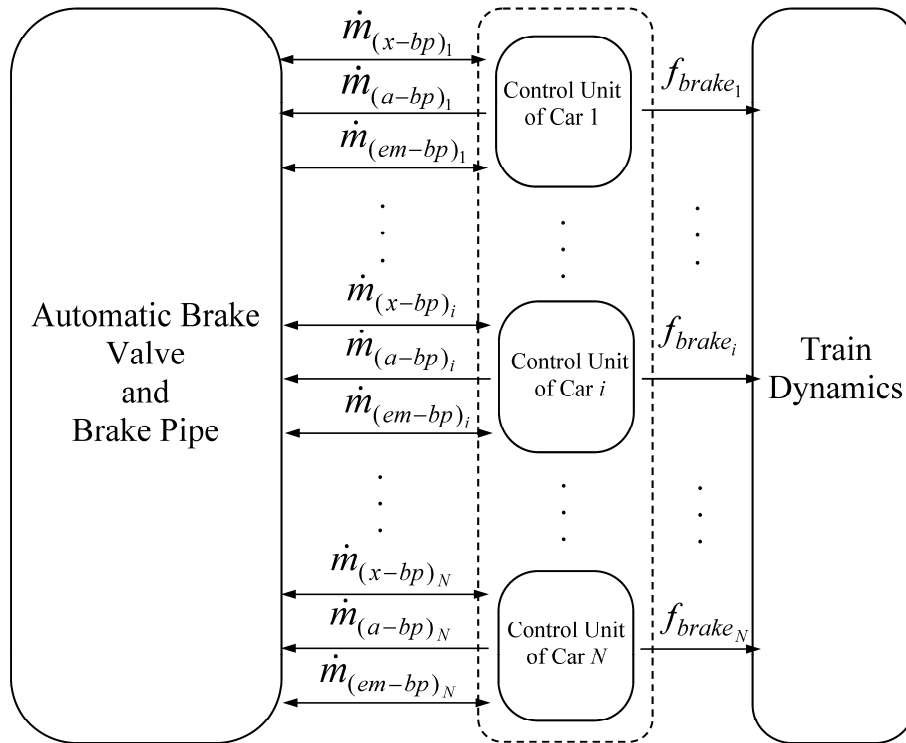


Figure 56. The relationship between the different models developed in this research

The first set of equations in Eq. 5.16 has  $n$  scalar equations that govern the train dynamics. In these equations,  $n$  is the number of equations,  $\mathbf{B}_{TD_{n \times n}}$  is the coefficient matrix that appears in the state space formulation of the equations of motion,  $\mathbf{y}_{TD_{n \times 1}}$  is the state vector,  $\mathbf{Q}_{brake_{n \times 1}}$  contains the brake forces, and  $\mathbf{Q}_{TD_{n \times 1}}$  contains other forces and moments acting on the car body. The second set of equations in Eq. 5.16 has the automatic brake valve and the brake pipe equations. In these equations,  $\mathbf{p}_{bp_{m \times 1}}$  and  $\mathbf{q}_{bp_{m \times 1}}$  are the FE brake pipe model variables,  $m$  is

the number of elements,  $\mathbf{Q}_{L_{m \times 1}}$  is the vector that contains the terms resulting from the leakage to the car control units,  $\mathbf{Q}_{p_{m \times 1}}$  contains other terms associated with the finite element discretization of the continuity equation,  $\dot{P}_{eq}$  and  $\dot{P}_{13}$  are, respectively, the time rate of the pressure inside the equalizing reservoir and the intermediate chamber of the 26C automatic brake valve. The third set of equations in Eq. 5.16 has the CCU equations developed in this chapter. In these equations,  $\mathbf{p}_{x_{N \times 1}}$ ,  $\mathbf{p}_{c_{N \times 1}}$ , and  $\mathbf{p}_{em_{N \times 1}}$  are the CCU pressures,  $N$  is the number of cars,  $\mathbf{Q}_{x_{N \times 1}}$ ,  $\mathbf{Q}_{c_{N \times 1}}$ , and  $\mathbf{Q}_{em_{N \times 1}}$  are the vectors containing the mass flow rates of Eqs. 5.8 and 5.9. The release and brake applications scenarios presented in Chapter 4 can now be repeated in order to highlight the CCU operation.

#### **5.4.1. Brake Release**

When the train is at rest, the steps of the algorithm used for the brake release mode are as follows:

1. Before the train starts moving, the slide valves are in the brake application position and the pressures inside the auxiliary reservoirs and the brake cylinders are equal to the full service brake cylinder pressure. The pressures inside the brake pipe, the equalizing reservoir, and the intermediate chamber are also assumed to be equal to the full service brake pressure.
2. The train dynamic equations are formulated as a set of first order ordinary differential equations (first set of Eq. 5.16). These equations are solved simultaneously with other sets of equations in Eq. 5.16 for given initial conditions

of the train car body, automatic brake valve, brake pipe, and car control units, as defined in step 1.

3. In the case of brake release, the automatic brake valve handle is positioned in the release mode. As a result, the pressure  $P_{13}$  increases and becomes large enough to open the brake pipe cut-off valve, allowing airflow to the brake pipe as discussed in Chapter 4. The brake pipe FE equations will show that the pressure at each node begins to increase, while the CCU parameters (i.e.  $\dot{\mathbf{p}}_{x_{N \times 1}}$  and  $\dot{\mathbf{p}}_{c_{N \times 1}}$ ) remain unchanged.
4. Linear interpolation is used to obtain the brake pipe pressure at the connection point with the CCU. At each time step, the interpolated value is compared with the auxiliary reservoir pressure of each car. The simulation continues until the brake pipe pressure becomes greater than the auxiliary reservoir pressure of one of the car control units. At this point, the CCU slide valve on that unit moves to the brake release position.
5. The mass flow rates from the brake pipe to the auxiliary reservoirs and from the brake cylinders to the atmosphere are, respectively, calculated using Eqs. 5.3 and 5.5. The calculated mass flow rate from the brake pipe is also used in the finite element equations as the brake pipe leakage ( $\mathbf{Q}_{L_{m \times 1}}$  in Eq. 5.16). This mass flow rate is also used to determine the time rate of the auxiliary reservoir pressure using Eq. 5.8 while the brake cylinder mass flow rate is used to calculate the time rate of its pressure using the second equation of Eq. 5.10.

6. The pressure time rates are integrated using standard integration method with the train dynamic and other air brake equations presented in Eq. 5.16, at each time step.
7. Steps 5 and 6 are repeated until the brake pipe pressure and auxiliary reservoir pressures all become equal to the intermediate chamber pressure. At the same time, the brake cylinder pressures decrease. The brake forces that are, in this mode, the maximum applicable frictional force (note that the wheels are at rest) are calculated using Eq. 5.13.
8. Once all the brake cylinder pressures reduce to the atmospheric pressure, the shoes are separated from the wheels and the friction forces are completely removed from the train equations ( $Q_{brake_{n \times 1}} = 0$  in the first equation of Eq. 5.16) and the train is ready to move. When, the automatic brake valve is in this brake release mode, its relay supply valve closes (with the assumption of no brake pipe leakage) and its intermediate chamber pressure will assume the brake pipe pressure.

#### **5.4.2. Brake Application**

When the train is in motion, the steps of the algorithm used for the service brake mode are as follows:

1. Before brake application, the equalizing reservoir pressure, the intermediate chamber pressure, and the pressure in the brake pipe are equal. Moreover, the CCU slide valves are in the brake release position, and the CCU auxiliary

reservoir pressures are equal to the brake pipe pressure while the brake cylinder pressures are equal to the atmospheric pressure.

2. The train dynamic equations are formulated as a set of first order ordinary differential equations and are solved simultaneously with the air brake equations for given initial conditions of the train car body, automatic brake valve, brake pipe, and control units, as defined in step 1.
3. In the case of brake application, the automatic brake valve handle is moved to the application position. As a result,  $P_{13}$  begins to decrease and the brake pipe cut-off valve opens. At this point, the brake pipe pressure begins to decrease while the CCU parameters (i.e.  $\dot{\mathbf{p}}_{x_{N \times 1}}$  and  $\dot{\mathbf{p}}_{c_{N \times 1}}$ ) remain the same.
4. Using linear interpolation, the brake pipe pressure at the connection point with the CCU is determined and compared with the corresponding auxiliary reservoir pressures. As the local brake pipe pressure falls below the CCU auxiliary reservoir pressure, the CCU slide valve moves to the brake application position. Such a movement disconnects the brake pipe from the CCU while it opens the connection between the brake cylinder and the auxiliary reservoir.
5. The rate of the mass flow from the auxiliary reservoir to the brake cylinder of the car is calculated using Eq. 5.4. The time rate of the auxiliary reservoir and the brake cylinder pressures can then be obtained using Eq. 5.8 and the second equation of Eq. 5.10, respectively. Unlike the brake release mode, in the case of brake application, there is no leakage from the brake pipe to the control units ( $\mathbf{Q}_{L_{m \times 1}} = \mathbf{0}$  in Eq. 5.16).

6. The brake forces that are determined from Eq. 5.13 are entered to the train dynamic equations ( $Q_{brake_{n \times 1}}$  in Eq. 5.16). The air brake and train dynamic differential equations are solved using standard integration method.
7. Steps 5 and 6 are repeated until the pressure becomes equal throughout the brake pipe while the air inside the auxiliary reservoirs and the brake cylinders equalize at the full service brake pressure. When the automatic brake valve is in the brake application mode, its relay exhaust valve closes and the intermediate chamber pressure assumes the pipe pressure.

It should be noted that during emergency brake, the leakage resulting from venting the brake pipe air, which is calculated using Eq. 5.5b, should be added to the finite element equations ( $Q_{L_{m \times 1}}$  in Eq. 5.16).

### **5.5. Numerical Results**

In all the simulations presented in this section, it is assumed that the cars of the trains have identical control units and all are connected to the brake pipe. It is further assumed that there is no brake pipe leakage in the first and second example. As a result, the pressure throughout the brake pipe, the auxiliary and emergency reservoir pressures in these examples are initially equal to the nominal brake pipe operating pressure (620.5 kPa gage or 90 psig), while the initial value of these pressures in the third example where the brake pipe leakage is present depend on the car/element location along the brake pipe. Nonetheless, the initial brake cylinder pressures in all the examples are assumed to be the same as the atmospheric pressure. Other decelerating forces such as air resistance, bearing and flange friction forces, curving drag forces, or track gradient forces, and the locomotive dynamic brake are not considered in this investigation. In the

simulations presented in this section, it is assumed that each car is fully loaded and has a mass of 129727.42 kg (286000 lb) and is free to move along the track while all other degrees of freedom are constrained (1-DOF for each car). In addition to the cars, locomotives are included in the models but no CCU or locomotive brake is considered for them. The number of locomotives in each example depends on the number of the cars while each locomotive has a mass of 166921.99 kg (368 000 lb). The coefficient of friction force against the air flow inside the brake pipe is assumed to be  $f_w = a(Re)^b$ , where  $Re$  is the Reynolds number,  $a$ , and  $b$  are the coefficients that depend on the flow regime (Abdol-Hamid, 1986) as given in Table IV. The locomotive automatic brake valve, the brake pipe, and the CCU properties that are used in the simulations presented in this section are shown in Tables V and VI (Abdol-Hamid, 1986; Sanborn et al., 2007).

Table IV. Friction coefficient for different flow regimes

Flow regime	Coefficient	$a$	$b$
Laminar		64.00	-1.00
Transient		0.000375	0.58
Turbulent		0.154	-0.1403

Table V. Brake pipe and automatic brake valve properties

Parameter description	Value
Air temperature	300 °K
Air viscosity	$1.95 \times 10^{-5}$ Pa.s
Atmospheric pressure	101.325 kPa (14.7 psia)
Brake pipe diameter (1¼" Schedule 80 extra heavy pipe)	3.246 cm (1.278 inches)
Operating pressure	620.5 kPa gage (90 psig)
Main reservoir pressure	951.48 kPa gage (138 psig)
Equalizing reservoir volume	3605.15 cm <sup>3</sup>
Feedback orifice area of the relay valve	1.072 cm <sup>2</sup>
Area of the relay valve diaphragm	83.613 cm <sup>2</sup>
Supply valve flow area of the relay valve	2.700 cm <sup>2</sup>
Exhaust valve flow area of the relay valve	4.382 cm <sup>2</sup>
Cross-sectional area of the relay valve exhaust orifice	0.317 cm <sup>2</sup>
Spring constant of the relay valve diaphragm	5.779 N/m
Exhaust valve spring constant of the relay valve	1.734 N/m
Spring constant of the relay valve diaphragm rod	3.597 N/m
Supply valve spring constant of the relay valve	1.769 N/m
Exhaust valve spring preload force of the relay valve	28.78 N
Spring preload force of the relay valve diaphragm rod	28.157 N
Supply valve spring preload force of the relay valve	16.458 N
Brake pipe cut-off valve flow area	0.810 cm <sup>2</sup>
Spring pre-load of the brake pipe cut-off valve	153.9 N

Table VI. Car control unit properties

Parameter description	Value
Number of brake cylinders per car	1
Number of brake shoes per car	8
Brake rigging leverage ratio	10:1
Brake rigging efficiency at full service brake	0.65
Brake shoe/wheel friction coefficient	0.35
Brake cylinder spring stiffness	14593 N/m
Brake cylinder maximum swept volume	10296.3 cm <sup>3</sup>
Brake piston effective frontal area	506.7 cm <sup>2</sup>
Brake cylinder and auxiliary reservoir equivalent connecting area	0.0236 cm <sup>2</sup>
Brake cylinder and emergency reservoir equivalent connecting area	0.0400 cm <sup>2</sup>
Brake cylinder and atmosphere equivalent connecting area	0.0446 cm <sup>2</sup>
Brake cylinder piping volume	4839.3 cm <sup>3</sup>
Auxiliary reservoir to brake valve piping volume plus quick service volume in pipe bracket	4439.1 cm <sup>3</sup>
Emergency reservoir to brake valve piping volume	3186.6 cm <sup>3</sup>
Auxiliary reservoir volume	40967.66 cm <sup>3</sup>
Auxiliary reservoir and brake pipe equivalent connecting area	0.0201 cm <sup>2</sup>
Emergency reservoir volume	57354.72 cm <sup>3</sup>

### 5.5.1. Brake Application in a 4-Car Model

As a first example, a 4-car model with one locomotive all moving with initial forward velocity of 24.6 m/s (55.0 mph) on an S-curve track is considered. The brake pipe length is 58.0 m (190.29 ft) and is modeled using 15 linear finite elements. The simulation starts when the train operator moves the brake handle in order to reduce the train speed on the curved section of the track. The operator applies a full service brake and the simulation continues until the train velocity reduces to 8.05 m/s (18.0 mph). The simulation results of this model are presented in Figs. 57-62. Figure 57 shows the train mass center acceleration as a function of time, while the velocity of car 1 is shown in Fig. 58. The brake force applied on the wheels of car 1 is shown in Fig. 59.

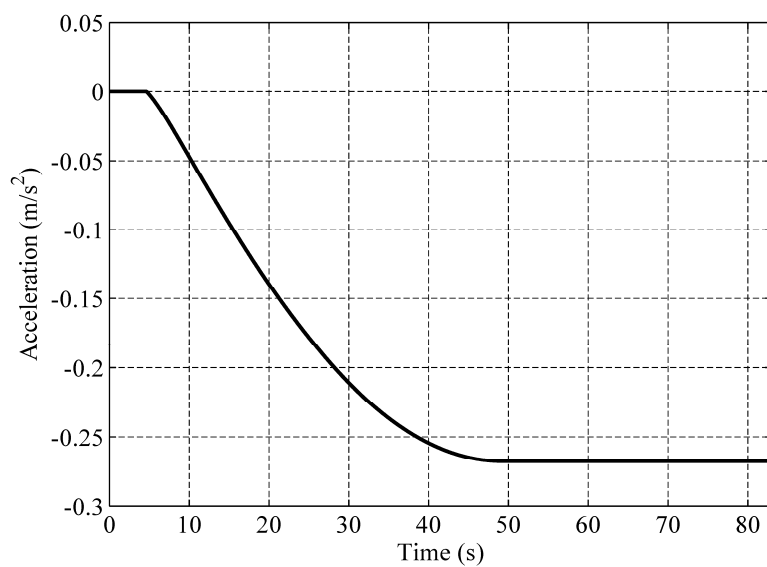


Figure 57. Train mass center acceleration

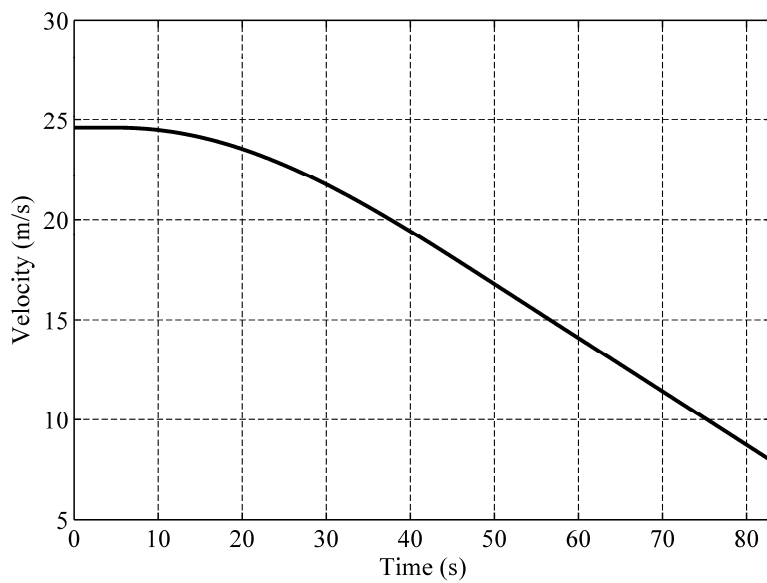


Figure 58. Velocity of car 1

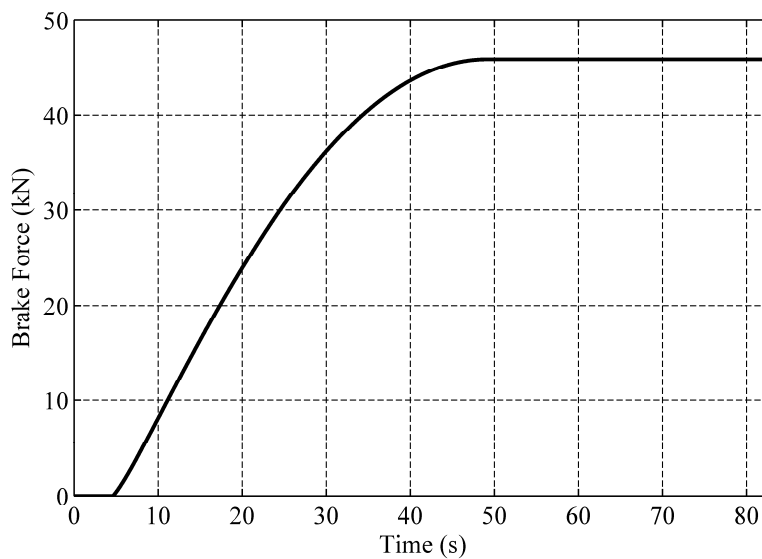


Figure 59. The brake force of car 1

The difference between the pressures on the two sides of the relay valve diaphragm is also plotted in Fig. 60. Figure 61 shows the pressure inside the equalizing reservoir and at the two ends of the brake pipe. Since the brake pipe is not very long, there is no significant time delay between the brake pipe head end and its rear end in response to the brake application. In long trains, however, there can be a considerable time delay depending on the brake pipe length. In Fig. 62, the pressure variations inside the CCU auxiliary reservoir and the brake cylinder of car 4 are shown.

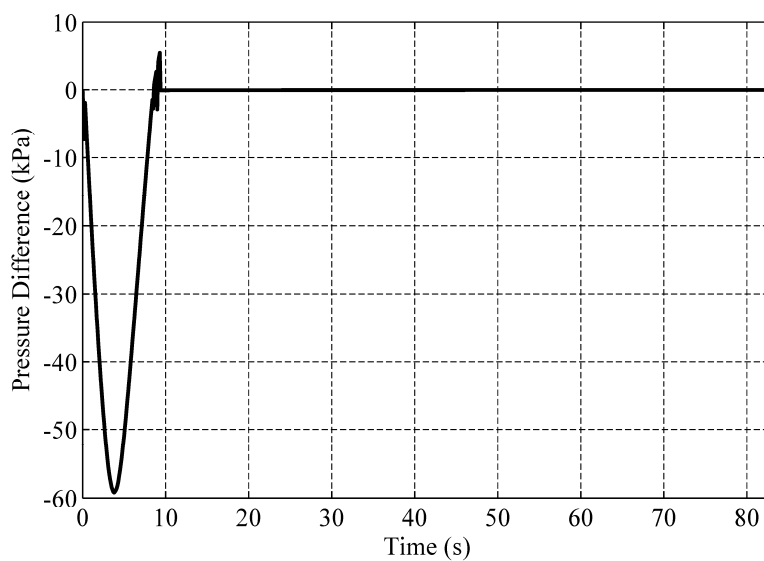


Figure 60. Pressure difference between the two sides of the relay valve diaphragm

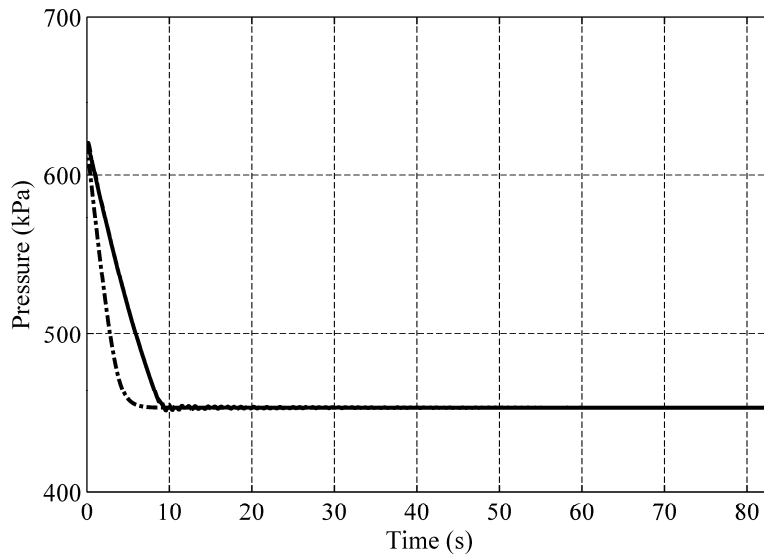


Figure 61. Pressure (gage) inside the equalizing reservoir and the brake pipe  
 ( ——— Head-end pressure, ..... Rear-end pressure,  
 - . - . Equalizing reservoir pressure)

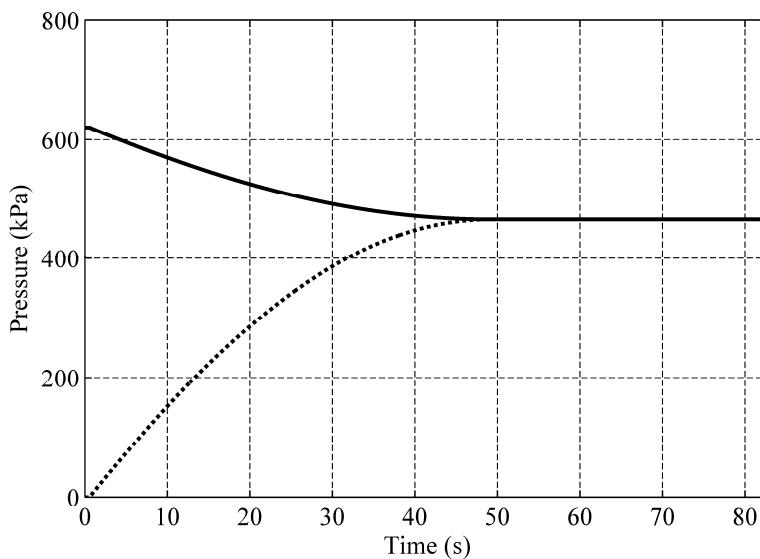


Figure 62. Auxiliary reservoir and brake cylinder pressures (gage) of car 4  
 (———— Auxiliary reservoir pressure of car 4, ..... Brake cylinder pressure of car 4)

### 5.5.2. Brake Application and Recharge in a 75-Car Model

In this section, a 75-car model for a train with 3 locomotives travelling on a tangent track is considered. It is assumed that all the cars and the locomotives have initial forward velocity of 29.1 m/s (65.0 mph), and the brake pipe length is 1059.5 m (3476.05 ft), which is modeled using 150 finite elements. At the beginning of the simulation, the train operator starts to apply a full service brake and after 60.0 seconds the brake handle is moved to the release mode. The results of this simulation are presented in Figs. 63-67. Figure 64 shows the pressures of the control unit components of cars 1 and 75 as functions of time. As shown in Fig. 64, after the operator releases the brake, it takes approximately 79.0 seconds for the auxiliary reservoir of car 1 to be fully recharged.

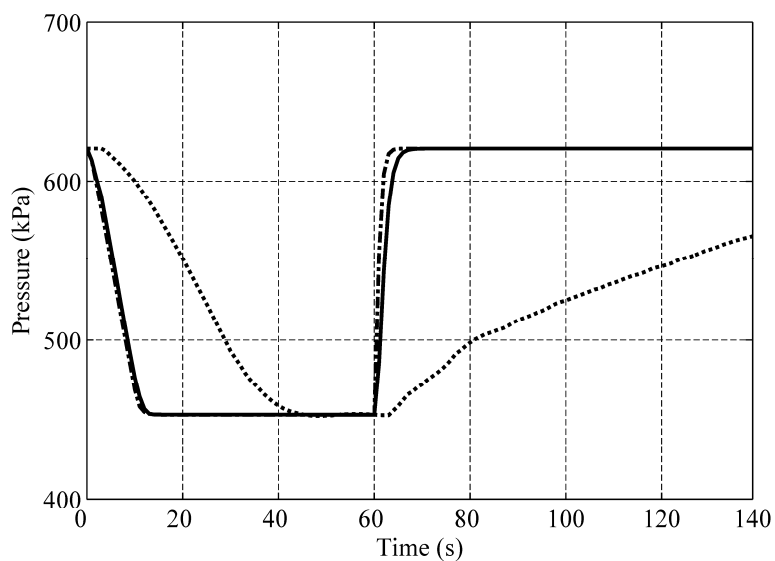


Figure 63. Pressure (gage) inside the equalizing reservoir and the brake pipe  
 (—— Head-end pressure, ..... Rear-end pressure, - . - . Equalizing  
 reservoir pressure)

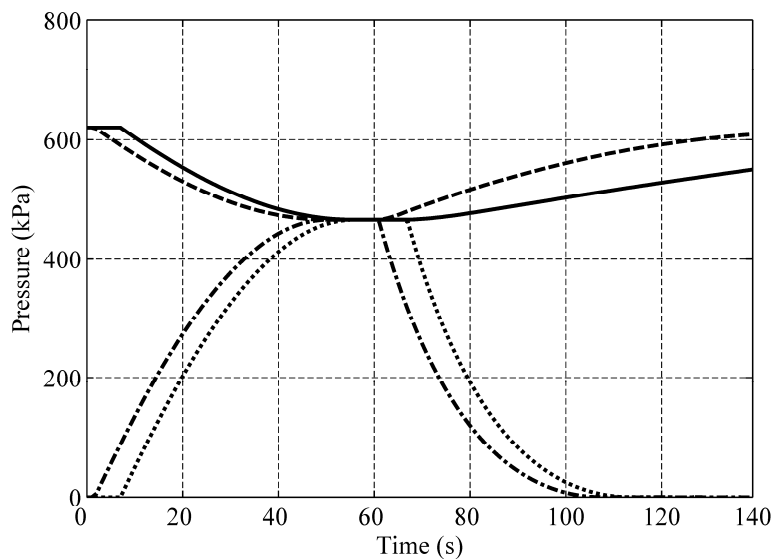


Figure 64. Auxiliary reservoir and brake cylinder pressures (gage) of cars 1 and 75  
 (--- Auxiliary reservoir pressure of car 1, - . - . Brake cylinder pressure of car 1,  
 —— Auxiliary reservoir pressure of car 75, ..... Brake cylinder pressure of car 75)

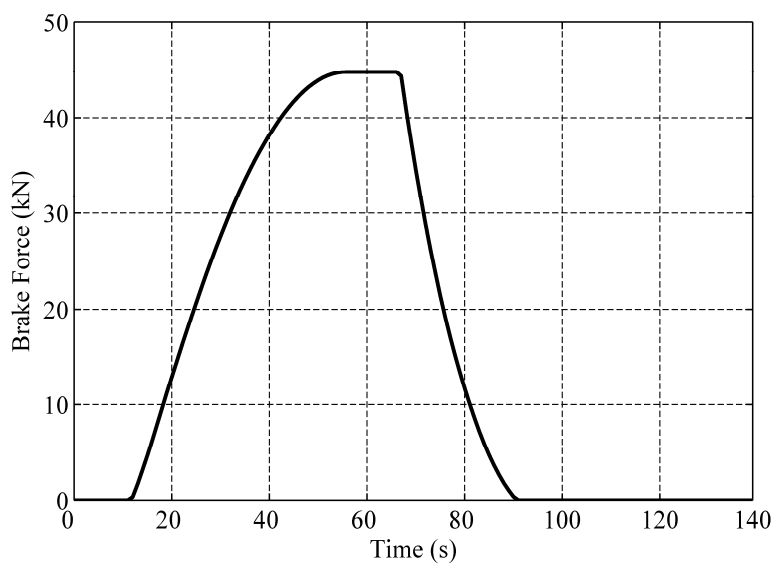


Figure 65. The brake force of car 75

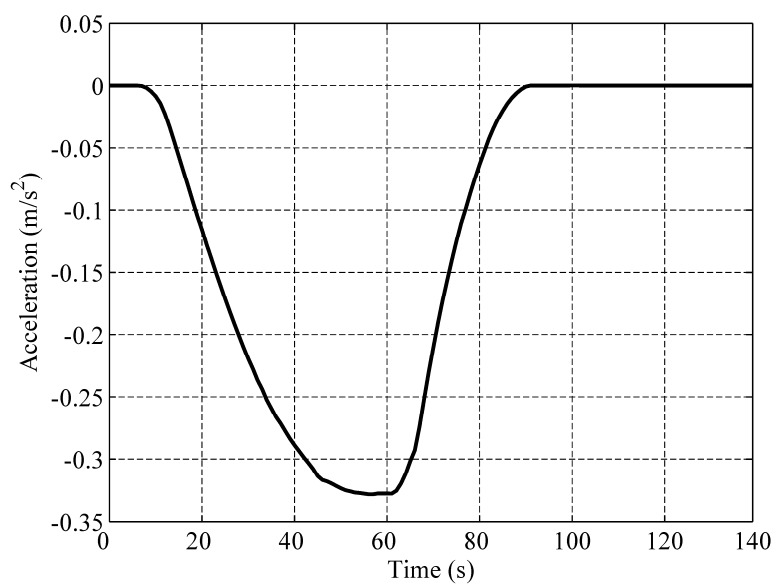


Figure 66. Train mass center acceleration

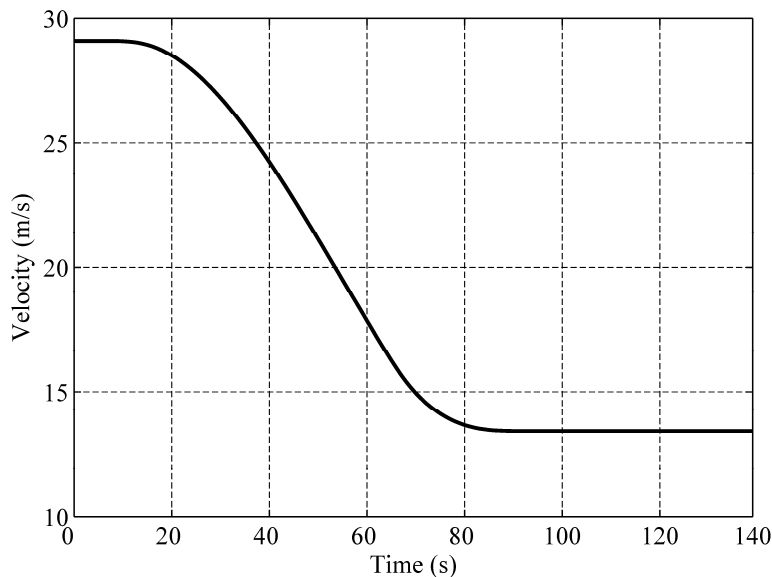


Figure 67. Train mass center velocity

### 5.5.3. Service and Emergency Brake in a 100-Car Model

In this example, a long train with 100 cars and 4 locomotives travelling on a tangent track is considered. The brake pipe, which has length of 1418.5 m (4653.87 ft), is modeled using 200 finite elements. Although more finite elements can be used, the use of 200 finite elements was found to be sufficient to achieve the required accuracy with less computational time as compared to the models that employ more finite elements. In this example, it is assumed that the train cars and locomotives have initial forward velocities of 31.29 m/s (70.0 mph). Unlike the two previous examples, it is assumed that the brake pipe has a leakage of 0.0283 m<sup>3</sup>/s (60 cfm). As a result, the initial brake pipe pressure, and the initial auxiliary and emergency reservoir pressures of the cars depend on the car/element location along the brake pipe. The simulation starts when the operator initially moves the brake handle to apply a full service brake. Then, in order to achieve

higher deceleration, after 50 seconds the operator applies the emergency brake and the simulation continues until the train stops.

Figure 68 shows the train mass center acceleration due to brake application. It is observed that the emergency brake application causes the mass center acceleration to reach the maximum value more rapidly. This is because of the fact that in a full service mode, as the auxiliary reservoir and the brake cylinder pressures approach the equalization pressure, the air flow rate between the two decreases. This leads to slower increase of the acceleration. However, once the emergency mode is activated, the emergency reservoir that still has its original pressure is connected to the brake cylinder, which results in a rapid increase in the brake cylinder pressure. Furthermore, such a connection leads to a higher brake cylinder pressure and as a result a higher acceleration than those of a full service brake (e.g. previous 75-car example) as observed in Fig. 68.

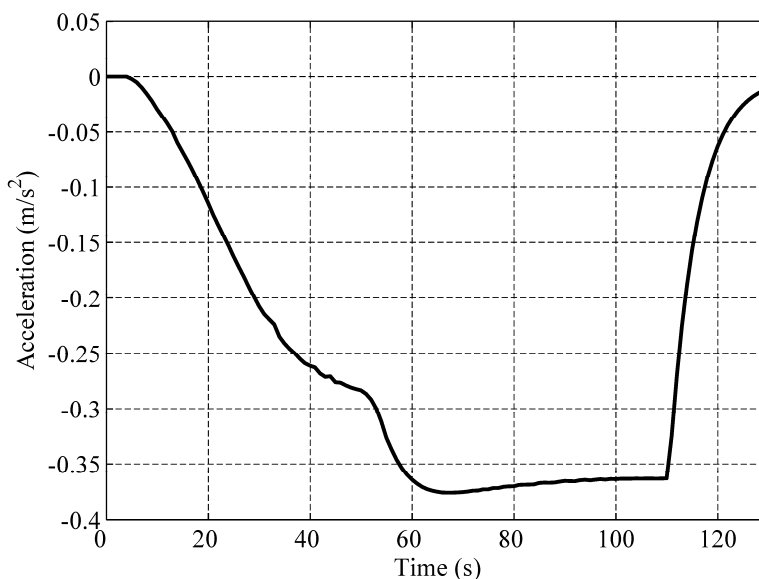


Figure 68. Train mass center acceleration

Figure 69 shows that after the emergency mode activation, the equalizing reservoir pressure rapidly reduces to the atmospheric pressure. It is observed that the pressure at the CCU locations of cars 25 and 75 also decreases much more rapidly after the emergency brake application due to the local brake pipe venting. The pressures of the CCU components of cars 1 and 100 are shown in Fig. 70. It is observed that the auxiliary reservoir, brake cylinder, and emergency reservoir of the car 1 eventually equalize at 541 kPa gage (78.5 psig). It can be observed that approximately at  $t = 97$  s, the brake cylinder of the last car has its highest pressure. After this instant, the brake force reaches its maximum, and as a result, the acceleration stops increasing (Fig. 68). As shown in Fig. 71, car 1 travels 2254.2 m (7395.67 ft) after brake application before it stops.

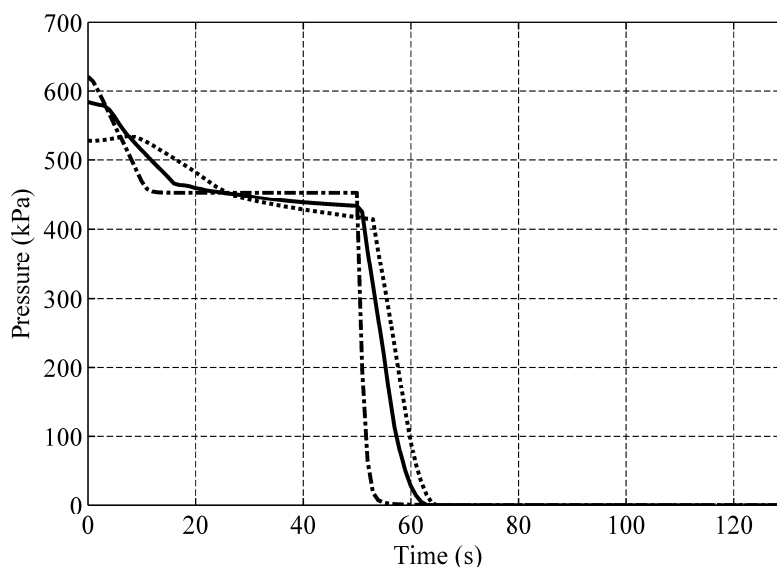


Figure 69. Pressure (gage) inside the equalizing reservoir and the brake pipe  
 (—— Pipe pressure at the control unit location of car 25, ..... Pipe pressure at the  
 control unit location of car 75, - . - . Equalizing reservoir pressure)

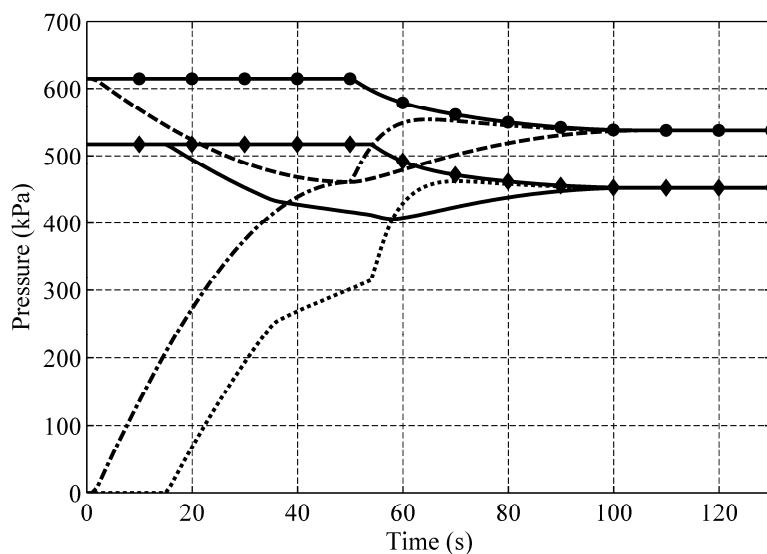


Figure 70. Auxiliary reservoir and brake cylinder pressures (gage) of cars 1 and 100  
 (--- Auxiliary reservoir pressure of car 1, -.-.- Brake cylinder pressure of car 1,  
 ●-●-● Emergency reservoir pressure of car 1, — Auxiliary reservoir pressure of car  
 100, ..... Brake cylinder pressure of car 100, ◆-◆-◆ Emergency reservoir pressure of car  
 100)

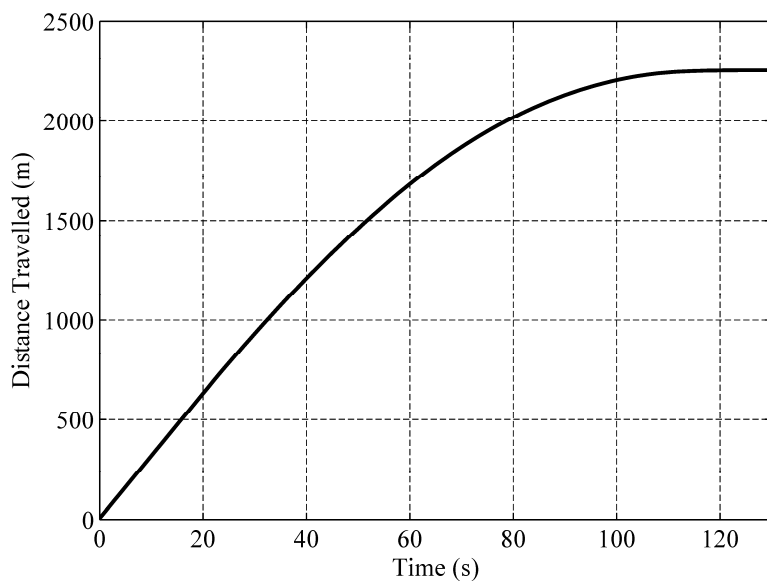


Figure 71. Distance travelled by car 1

## **5.6. Validation**

In order to validate the air brake dynamic model developed in this study, the results obtained using numerical simulations are compared with the experimental and analytical results.

### **5.6.1. Comparison with Experimental Results**

A brake pipe and a 26C automatic brake valve with the same properties of those used in experiments reported in the literature are used. It is assumed that the pipe has effective length of 304.8 m (1000 ft) and there is no brake pipe leakage or leakage to the car control units (Abdol-Hamid, 1986). Furthermore, in order to be consistent with the experiment, only the air brake model is considered here and the train dynamic model is ignored. That is, the simulations in this section are carried out with the cars stationary, using a nominal brake pipe operating pressure of 413.7 kPa (60 psig). The air brake is modeled using 200 linear finite elements. The brake application and recharge modes are simulated, and the brake pipe pressure variations are determined.

First, at the beginning of the simulation, the automatic brake valve handle is positioned in the brake application sector, which results in 158.6 kPa (23 psi) reduction in the equalizing reservoir pressure. Consequently, the brake pipe pressure reduces from the operating pressure to the equalizing reservoir pressure. The results of the simulation are presented in Figs. 72-74, and these results are compared with the experimental results reported in the literature (Abdol-Hamid, 1986).

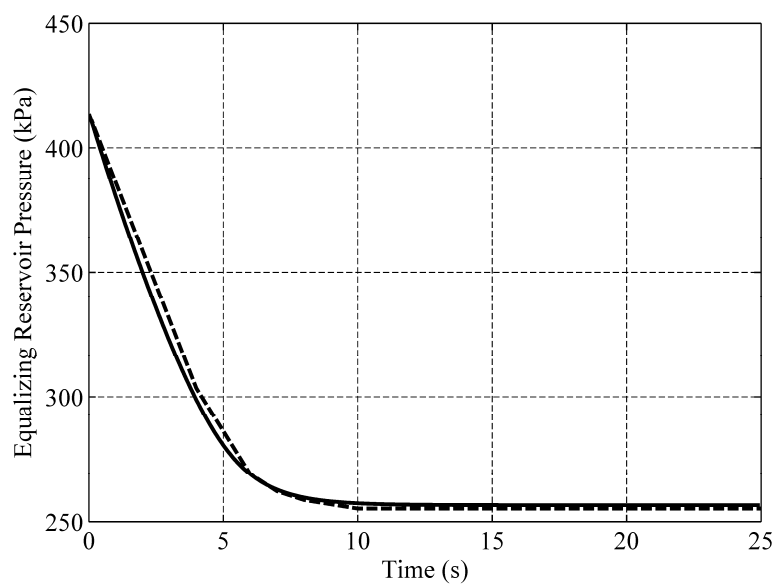


Figure 72. Equalizing reservoir pressure (gage) comparison  
( - - - - Experimental results, ——— Present model results)

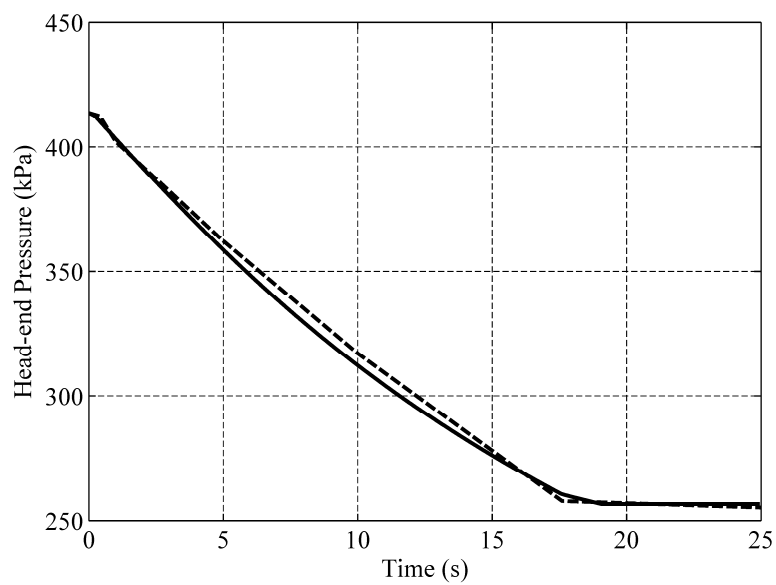


Figure 73. Head-end pressure (gage) comparison  
( - - - - Experimental results, ——— Present model results)

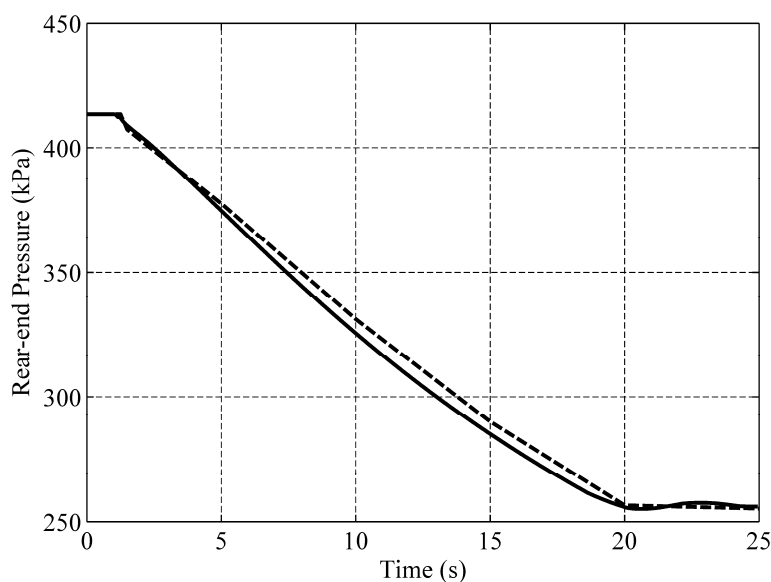


Figure 74. Rear-end pressure (gage) comparison  
 (--- Experimental results, — Present model results)

Second, the recharge mode is simulated. It is assumed that initially the equalizing reservoir pressure and pressure throughout the brake pipe are all equal to 255.1 kPa (37 psig). At the beginning of the simulation, the automatic brake handle is positioned in the recharge mode, which results in an increase in the brake pipe pressure until the brake pipe is completely charged. The results of the simulations and the experimental results are shown in Figs. 75-77. The comparison presented in Figs. 72-77 show a good agreement between the simulation and experimental results.

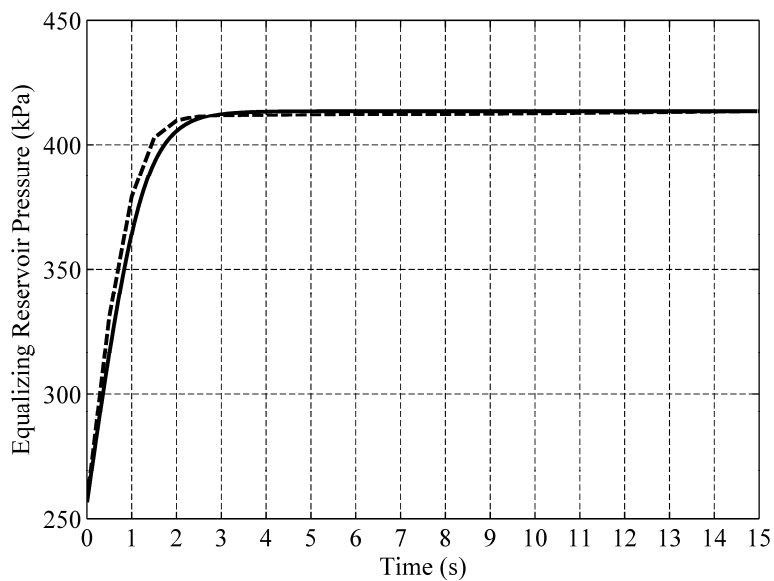


Figure 75. Equalizing reservoir pressure (gage) comparison  
 ( - - - - Experimental results, ——— Present model results)

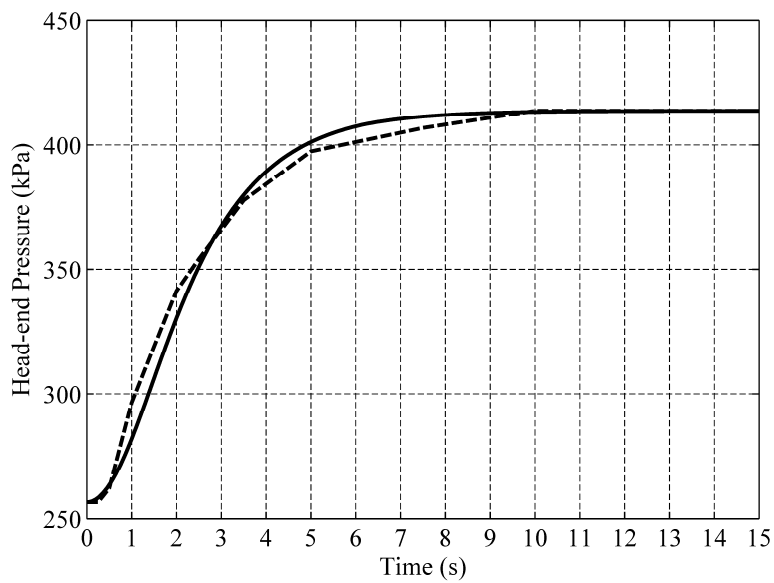


Figure 76. Head-end pressure (gage) comparison  
 ( - - - - Experimental results, ——— Present model results)

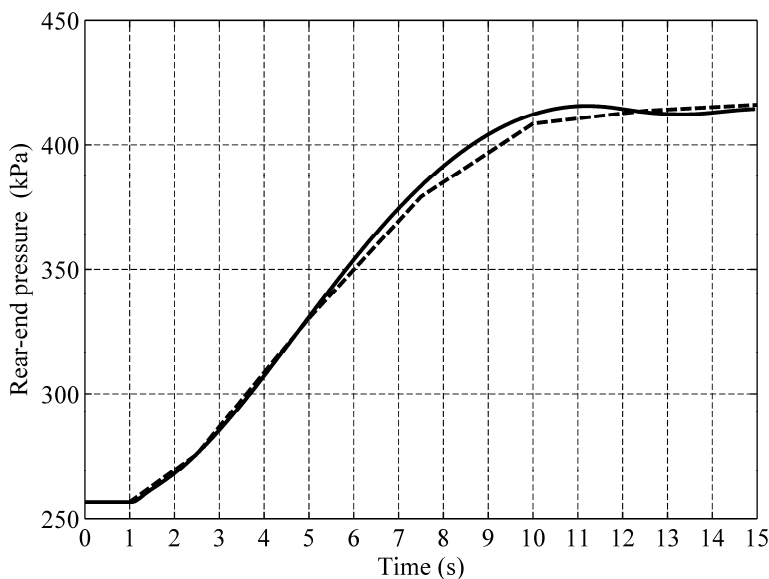


Figure 77. Rear-end pressure (gage) comparison  
 (--- Experimental results, — Present model results)

### 5.6.2. Analytical Validation of Airbrake Dry Charge

In this section, the mass transferred to the brake pipe and the CCU reservoirs during a dry charge, which is simulated using the model developed in this investigation is calculated and compared with the analytical result obtained using the universal gas law. A stationary train with 100 cars and 4 locomotives is considered with a brake pipe length of 1418.5 m (4653.87 ft), while its brake pipe is modeled using 200 elements. It is assumed that initially, the pressure throughout the brake pipe and the CCU components are the atmospheric pressure and there is no brake pipe leakage. As the simulation starts, the automatic brake valve handle is positioned in the recharge mode until all auxiliary and emergency reservoirs are completely charged to 620.5 kPa gage (90 psig). It is assumed that the airbrake system properties are the same as the ones used in the previous examples as given in Tables V and VI. The results show that it takes approximately 1420 seconds for the air brake to be completely charged (Fig. 78). The simulation stops when all

the CCU auxiliary and emergency reservoirs are fully charged. Figure 79 shows the mass transfer rate at the head-end of the brake pipe obtained using the present model.

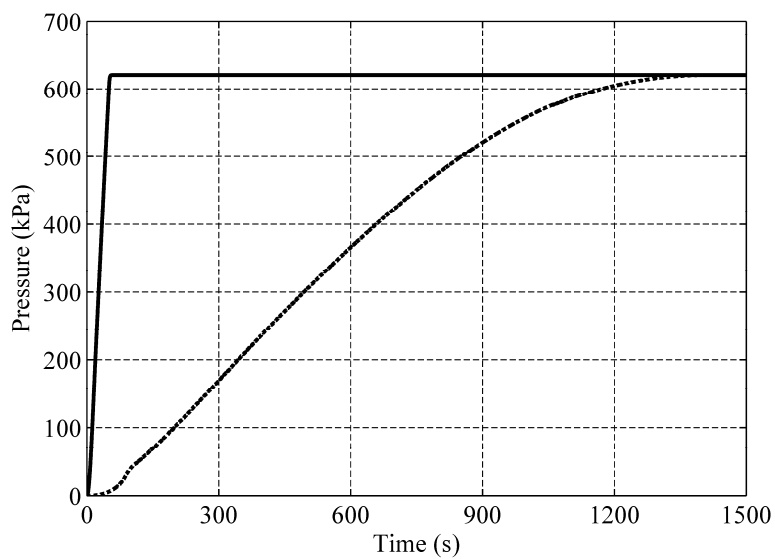


Figure 78. Pressure (gage) at the brake pipe ends during dry charge (— Head-end pressure, - - - Rear-end pressure)

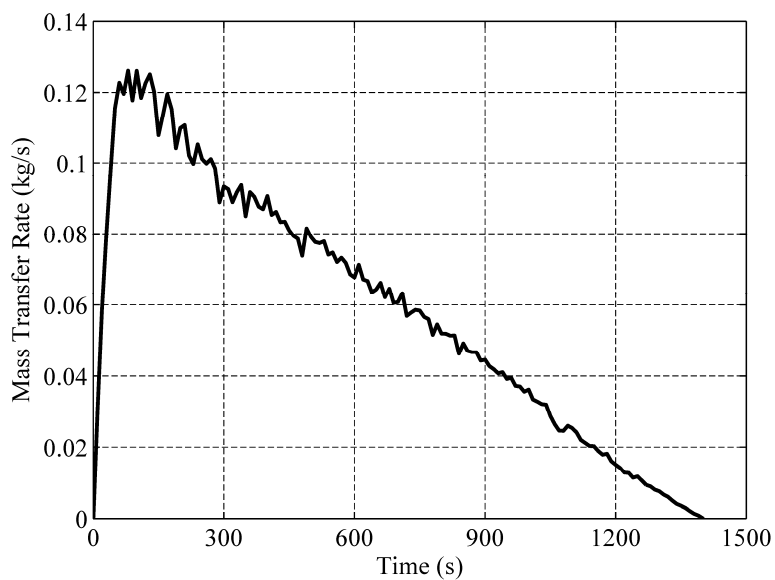


Figure 79. Mass transfer rate during dry charge

The total mass transferred to the brake pipe can be obtained as follows:

$$\Delta m_{air} = \int_0^{t_e} \dot{m}_{head-end} dt \quad (5.17)$$

where  $t_e$  is the simulation time and  $\Delta m_{air}$  is the total mass transferred to the pipe. Using numerical integration, one obtains  $\Delta m_{air} = 83.26$  kg for  $t_e = 1420.1$  s.

On the other hand, the total transferred mass can be simply calculated using the universal gas law

$$\Delta m = \Delta P \frac{V_{total}}{R\theta} \quad (5.18)$$

where  $\Delta P = 620.5$  kPa is the difference between the pressures at the end and the beginning of the dry charge process, and  $V_{total} = 11.768$  m<sup>3</sup> is the total volume of the brake pipe and the CCU components (including auxiliary and emergency reservoirs, branch pipes, etc) of all the cars. Using the preceding equation, one obtains  $\Delta m = 84.84$  Kg. By comparing the results of Eqs. 5.17 and 5.18, one can show that the error is approximately 1.86%.

### **5.7. Concluding Remarks**

In this study, a train air brake model was developed and integrated with a nonlinear train dynamic model based on the trajectory coordinates. The air brake model considered in this investigation includes three parts; the 26C locomotive automatic brake valve that controls air transfer to or from the brake pipe based on the brake valve handle position, the brake pipe that transmits the brake signal coming from the locomotive valve as well as the pressurized air to the control units, and the car control units that are installed on each car and apply the frictional brake force on the car wheels using their mechanical and pneumatic components. For the 26C

automatic brake valve, the models of the regulating, relay, and brake pipe cut-off valves were developed. Furthermore, a linear finite element model was developed for the brake pipe air flow. For the car control unit, it was assumed that the triple valve was used as the control valve. This control valve is connected to the branch pipe, the CCU auxiliary reservoir, emergency reservoir, and brake cylinder of the car. The triple valve operation that is function of the brake pipe pressure was discussed and the relationship between the CCU parameters for each operation mode was presented. A mathematical model for the CCU was developed and the car brake force was calculated in terms of the CCU parameters. Computer simulations that include trains with different brake pipe lengths, tracks, and initial forward velocities were considered and the train dynamic response to the air brake operation as well as the variations of the air brake parameters in the cases of the service, emergency, and recharge modes were investigated. Experimental results reported in the literature as well as simple analytical models were used to validate the computer simulations results.

## 6. SUMMARY AND CONCLUSIONS

This thesis addressed three important topics associated with the wheel/rail contact analysis and the train longitudinal dynamics. These topics are the effect of the choice of the contact frame on the contact parameters, the development of a multipoint wheel/contact search algorithm, and the integration of an air brake model with efficient train longitudinal force algorithms. The results and conclusions of this study are summarized in this chapter.

In wheel/rail creep force formulations, the rolling direction is used with the normal to the contact surfaces to construct the contact frame in which the tangential creep forces are defined. When Hertz theory is used, an assumption is made that the rolling direction is the same as the direction of one of the axes of the contact ellipse. The rolling direction, however, depends on the motion of the wheel with respect to the rail; while the directions of the axes of the contact ellipse depend only on the geometry of the wheel and rail surfaces and they are determined using the principal directions. This investigation aimed at studying this fundamental problem and comparing the results obtained using three different contact frames. These frames are the rolling direction (RD) frame, the contact ellipse (CE) frame and the longitudinal tangent (LT) frame. The RD frame is rarely used in the railroad vehicle simulations and can lead to problems in traction and braking scenarios and also in the case of velocity discontinuities due to impact between the vehicle components. While none of the axes of the contact ellipse define in general the rolling direction, the CE frame is the one used in many investigations on railroad vehicle systems. Some authors have also employed the LT frame which is independent of Hertz theory and does not involve any motion variables such as the angular velocities. The results obtained using the three contact frames were compared and it was shown that the results obtained using

the CE and LT contact frames were in a very good agreement. However, there are simulation scenarios in which the rolling direction as defined by the angular velocity vector can significantly differ from the axes of the contact ellipse. The numerical results obtained in this study shows that while there can be differences in the creepage results of different contact frame models, the contact forces obtained using all these models, in the case of realistic scenarios, are in a good agreement despite the significant orientation difference between different frames. Such a good agreement for the force results can be attributed to the dominant effect of the spin creepage in the lateral force calculations. However, in some extreme cases, there can be differences between the results obtained using different contact frames, in particular the results of the RD model can significantly differ from the results of the CE and LT models.

Furthermore, in this thesis, a multipoint contact search algorithm was developed. The developed algorithm imposes no limitation on the method used to find the first point of contact or on the number of contact points. The algorithm is capable of finding the contact points with a good precision because of the use of an iterative Newton-Raphson algorithm. The developed algorithm successfully finds multiple wheel/rail contact points. This was demonstrated by two examples in this thesis. A comparison between the results obtained using the constraint and elastic contact methods in the case of multipoint contact scenario was made and the differences between these methods in predicting the contact force distributions were discussed. It was demonstrated by an example that the change of the contact method used for predicting the first contact point in the case of multipoint contact scenarios could considerably affect the normal force distribution among the contact points.

Ultimately, in this thesis, a train air brake model was developed and integrated with a nonlinear train dynamic model based on the trajectory coordinates. The air brake model considered in this investigation includes three parts; the 26C locomotive automatic brake valve that controls air transfer to or from the brake pipe based on the brake valve handle position, the brake pipe that transmits the brake signal coming from the locomotive valve as well as the pressurized air to the control units, and the car control units that are installed on each car and apply the frictional brake force on the car wheels using their mechanical and pneumatic components. For the 26C automatic brake valve, the models of the regulating, relay, and brake pipe cut-off valves were developed. Furthermore, a linear finite element model was developed for the brake pipe air flow. For the car control unit, it was assumed that the triple valve was used as the control valve. This control valve is connected to the branch pipe, the CCU auxiliary reservoir, emergency reservoir, and brake cylinder of the car. The triple valve operation that is function of the brake pipe pressure was discussed and the relationship between the CCU parameters for each operation mode was presented. A mathematical model for the CCU was developed and the car brake force was calculated in terms of the CCU parameters. Computer simulations including trains with different brake pipe lengths, tracks, and initial forward velocities were considered and the train dynamic response to the air brake operation as well as the variations of the air brake parameters in the cases of the service, emergency, and recharge modes were investigated. Experimental results reported in the literature as well as simple analytical models were used to validate the computer simulations results.

## REFERENCES

1. Abdol-Hamid, K.S.: Analysis and Simulation of the Pneumatic Braking System of Freight Trains, Ph.D. Dissertation, Department of Mechanical Engineering, University of New Hampshire, Durham, New Hampshire, 1986.
2. American Association of Railroads, Manual of Standards and Recommended Practices-Section M, RP-548, Association of American Railroads, 2002a.
3. American Association of Railroads, Manual of Standards and Recommended Practices-Section M, RP-5132, Association of American Railroads, 2002b.
4. American Association of Railroads, Train Make-up Manual, Report R-802, Association of American Railroads Technical Center, 1992.
5. Andrews, H. I.: Railway Traction, Elsevier Science Publishers, 1986.
6. Ayasse, J.B., Chollet, H., and Maupu, J.L.: Paramètres caractéristiques du contact roue-rail. INRETS report, No. 225, ISBN 0768-9756, 2000.
7. Balon, L.V., and Aizinbud, K.S.: Improving the wear resistance of electromagnetic rail brake parts, Soviet Journal of Friction and Wear, 10: 134-136, 1989.
8. Bansiter, W.N.: A Dynamic Model of Pneumatic Control Valve System, Master Thesis, University of New Hampshire, Durham, New Hampshire, 1979.
9. Berzeri, M., Sany, J. R., and Shabana, A. A.: Curved Track Modeling Using the Absolute Nodal Coordinate Formulation. Technical Report # MBS00-4-UIC, Department of Mechanical Engineering, University of Illinois at Chicago, Chicago, 2000.
10. Bharath, S., Nakra, B.C., and Gupta, K.N.: Distributed mathematical model for pressure transient analysis in railway pneumatic brake system, International Journal of Mechanical Sciences, 32: 133-145, 1990.
11. Dukkupati, R.V, and Amyot, J.R: Computer-Aided Simulation in Railway Dynamics, Marcel-Dekker, New York, 1988.
12. Escalona, J.L., Gonzalez, M., Zaazaa, K.E., and Shabana, A.A., 2003: A technique for validating a multibody wheel/rail contact algorithm, Proceedings of the ASME 2003 Design Engineering Technical Conferences and Computers and Information in Engineering Conference, Chicago, Illinois, USA, September 2-6, 2003.
13. Funk, J. E., and Robe, T. R.: Transients in pneumatic transmission lines subjected to large pressure changes, International Journal of Mechanical Sciences, 12: 245-257, 1970.

14. Garg, V. K., and Dukkipati, R. V.: Dynamics of Railway Vehicle Systems, Academic Press, 1984.
15. Gauthier, R.G.: An Analysis and Simulation of a Pneumatic Control Valve System Master Thesis, University of New Hampshire, Durham, New Hampshire, 1977.
16. Goldsmith, W.: Impact: The Theory and Physical Behavior of Colliding Solids, Edward Arnold Ltd, London, 1960.
17. Gugliotta, A., and Soma, A.: Comparison of ADAMS Rail results with European benchmark data, 11th European ADAMS Users' Conference, Frankfurt, 1996.
18. Guilloux, J. P.: Original method of braking wagons in marshalling yards: the Faiveley rail brake, French Railway Review, 2: 239-242, 1984.
19. Hertz, H.: Über die berührung fester elastische Körper und über die Harte, *Verhandlungen des Vereins zur Beförderung des Gewerbefleisses*, Leipzig, 1882.
20. Ho., A. K.: A Study of the Effect of Leakage for Scaled-down Brake Pipe Model, Master's Thesis, Concordia University, Montreal, Canada, 1981.
21. Hoffman, M.: Dynamics of European Two-Axle Freight Wagons, Ph.D. Dissertation, Technical University of Denmark, Kongens Lyngby, Denmark, 2006.
22. John, J. E., and Keith, T. G.: Gas Dynamics, Third Edition, Pearson Education, Inc, 2006.
23. Johnson, K.L.: Contact Mechanics, Cambridge University Press, 1985.
24. Kalker, J.J.: On the Rolling Contact of Two Elastic Bodies in the Presence of Dry Friction, Ph.D. thesis, Delf University of Technology, Delf, Netherland, 1967.
25. Kalker, J.J.: Three-dimensional Elastic Bodies in Rolling Contact, Kluwer, Dordrecht, 1990.
26. Kratville, W. W. (Editor): The Car and Locomotive Cyclopedia, Simmons-Boardman Books, Inc, 1997.
27. Kreel, J.W.: A Dynamic Model and Computer Simulation of a Pneumatic Control Valve System, Master Thesis, University of New Hampshire, Durham., New Hampshire, 1979.
28. Kreyszig, E.: Differential Geometry, Dover, Mineola, NY, 1991.
29. Limbert, D.: AAR undesired emergency brake study complete - Association of American Railroads Vehicle Track Systems Newsletter, Railway Age, 1990.
30. Malvezzi, M., Meli, E., Falomi, S., and Rindi, A.: Determination of wheel-rail contact points with semi-analytic methods, Multibody System Dynamics, 20: 327-358, 2008.

31. Nasr, A., and Mohammadi, S.: The effects of train brake delay time on in-train forces, Proceedings of the Institution of Mechanical Engineers, Part F: Journal of Rail and Rapid Transit, 224: 523-534, 2010.
32. Obara, T., Kumagai, N, and Takiguchi, T: Development of hybrid rail brake, Proceedings of the Institution of Mechanical Engineers, Part F: Journal of Rail and Rapid Transit, 209: 61-65, 1995.
33. Pascal, J.P., and Sauvage, G.: New method for reducing the multi-contact wheel/rail problem to one equivalent rigid contact patch, Proceedings of 12th IAVSD Symposium, 26–30 August, Lyon, 1991.
34. Pascal, J.P., and ZaaZaa, K.E.: A study of the effect of m and n coefficients of the Hertzian contact theory on railroad vehicle dynamics, Proceedings of the ASME 2007 International Design Engineering Technical Conference & Computers and Information in Engineering Conference IDETC/CIE, September 4-7, Las Vegas Nevada, USA, 2007.
35. Piotrowski, J., and Chollet, H.: Wheel–rail contact models for vehicle system dynamics including multi-point contact, Vehicle System Dynamics, 43: 455-483, 2005.
36. Pombo, J.C., and Ambrósio, J.A.C.: Application of a wheel–rail contact model to railway dynamics in small radius curved tracks, Multibody System Dynamics, 19: 91–114, 2008.
37. Railway Technical Web Pages: Air Brakes. <http://www.railway-technical.com/air-brakes.shtml>, site last updated on July 16, information obtained on August 18, 2010.
38. Sakamoto, Y., Kashiwagi, T., Tanaka, M., Hasegawa, H., Sasakawa, T., and Fujii, N.: Rail brake system using a linear induction motor for dynamic braking, IEEJ Transactions on Industry Applications, 129: 342-349, 2009.
39. Sanborn, G., Heineman, J., and Shabana, A.A.: A low computational cost nonlinear formulation for multibody railroad vehicle systems, Proceedings of the 2007 ASME Design Engineering Technical Conferences, Paper # DETC2007-34522, Las Vegas, Nevada, September 4–7, 2007a.
40. Sanborn, G., Heineman, J., and Shabana, A.A.: Implementation of low computational cost nonlinear formulation for multibody railroad vehicle systems, Proceedings of the 2007 ASME Design Engineering Technical Conferences, Paper # DETC2007-34525, Las Vegas, Nevada, September 4–7, 2007b.
41. Shabana, A.A.: Computational Continuum Mechanics, Cambridge University Press, 2008.
42. Shabana, A. A.: Computational Dynamics, Third Edition, John Wiley and Sons, 2010.

43. Shabana, A.A., Berzeri, M., and Sany, J.R.: Numerical procedure for the simulation of wheel/rail contact dynamics, ASME Journal of Dynamic Systems, Measurement, and Control, 123: 168-178, 2001.
44. Shabana, A.A., Tobaa, M., Sugiyama, H., and Zaazaa, K.E.: On the computer formulations of the wheel/rail contact, Nonlinear Dynamics, 40, 169-193, 2005.
45. Shabana, A. A., Zaazaa, K. E., and Sugiyama, H.: Railroad Vehicle Dynamics: A Computational Approach, Francis & Taylor/RC, 2008.
46. Shute, B.W., Wright, B.C., Taft, C.K. and Banister, W.N.: The effect of leakage distribution on brake pipe gradient and brake pipe flow rate, ASME Paper, No. 79-WA/RT-16, 1979.
47. Sugiyama, H., Tanii, Y., and Suda, Y.: Analysis of wheel/rail contact geometry in turnout section, Proceedings of the ASME 2009 International Mechanical Engineering Congress & Exposition IMECE2009, November 13-19, Lake Buena Vista, Florida, USA, 2009.
48. Wei, W., and Lin, Y.: Simulation of a freight train brake system with '120' valves, Proc. IMechE Part F: J. Rail and Rapid Transit, 223: 85-92, 2009.
49. Wetenkamp, H. R.: Management of Train Operation and Train Handling, Air Brake Association, 1974.
50. White, F.M.: Fluid Mechanics, Sixth Edition, McGraw Hill Book Company, 2008.
51. Wright, B.W.: A Dynamic Analysis of Distributed Pneumatic Control System, Master Thesis, University of New Hampshire, Durham, New Hampshire, 1978.

## APPENDIX

### 1. Calculations of the Regulating Valve Areas

The regulating valve equations presented in this Chapter 4 are expressed in terms of areas that will be evaluated in this section of the appendix. As discussed in Chapter 4, the regulating valve areas  $A_{2,3}$  and  $A_{2,2}$  are functions of the valve displacement; denoted as  $X_{2,1}$ . Assume that there are only two variable surface areas created by the relative movement of the valve with respect to its seat. One of these areas is perpendicular to the valve movement direction  $X$ , called  $A_x$ ; while the other is tangent to the valve movement, called  $A_r$ . For  $A_x$ , one has:

$$A_x = \pi \left( r_0^2 - r^2(X_{2,1}) \right) \quad (1)$$

where  $r_0$  is the radius of the valve seat, and  $r(X_{2,1})$  is the inner radius of the annular orifice which varies with the valve displacement. The radius  $r(X_{2,1})$  can be defined as

$$r(X_{2,1}) = \frac{r_0(l - X_{2,1})}{l} \quad (2)$$

If  $\alpha = 45^\circ$ , then  $l = r_0$ , and  $r(X_{2,1})$  is given in this special case by  $r(X_{2,1}) = r_0 - X_{2,1}$ ;

and the area in this special case reduces to  $A_x = A_0 - \pi(r_0 - X_{2,1})^2$ . For  $A_r$ , one has

$$A_r = \pi D_l X_{2,1} \quad (3)$$

where  $D_l$  is the diameter of the inner area of the valve seat. Assuming that  $A_x$  and  $A_r$  are in series, the equivalent area  $A_{EQV}$  can be defined as

$$A_{EQV} = \frac{A_x A_r}{\sqrt{A_x^2 + A_r^2}} \quad (4)$$

$A_{EQV}$  can be  $A_{2,2}$  for the exhaust valve and  $A_{2,3}$  for the supply valve.

## 2. Relay Valve Diaphragm Forces

In this section of the appendix, the expressions for the forces that appear in Eq. 4.53 are developed. As discussed in Section 4.7, during the movement of the diaphragm not all the force components are active. The forces  $F_{1,1} = P_{1,1}A_{1,2}$  and  $F_{1,2} = P_{1,2}A_{1,2}$  are always present, while the force  $S_{1,2}$  takes the following values in the specified ranges:

$$S_{1,2} = \begin{cases} L_{1,2} + K_{1,2}X_{1,1} & 0 \leq X_{1,1} \leq X_S \\ L_{1,2} + K_{1,2}(X_{1,1} + X_I) & -X_E \leq X_{1,1} \leq -X_I \\ 0 & \text{otherwise} \end{cases} \quad (5)$$

When the supply valve is open,  $S_{1,1} = 0$ , and

$$S_{1,3} = L_{1,3} + K_{1,3}(X_{1,1} - X_0) \quad X_0 \leq X_{1,1} \leq X_S \quad (6)$$

When the exhaust valve is open,  $S_{1,3} = 0$ , and

$$S_{1,1} = -L_{1,1} + K_{1,1}(X_{1,1} + X_I) \quad -X_E \leq X_{1,1} \leq -X_I \quad (7)$$

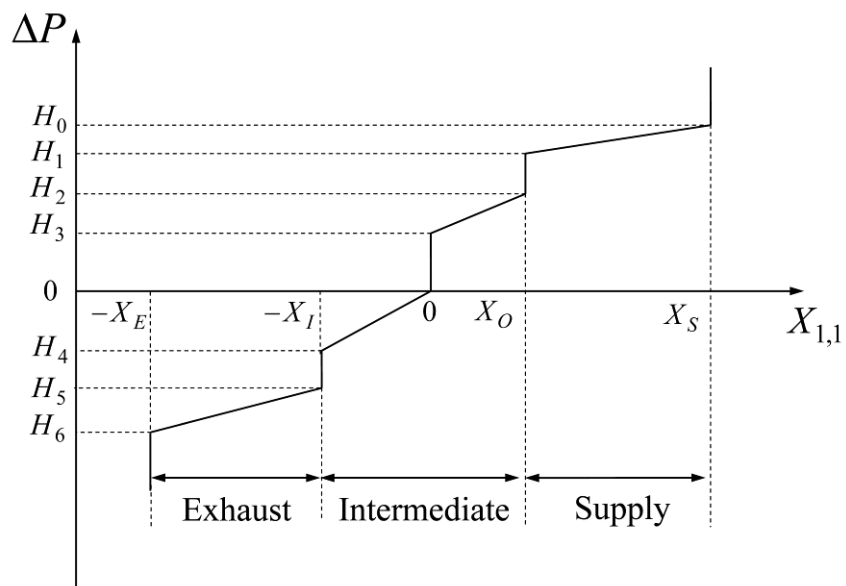
where  $K_{1,1}$ ,  $K_{1,2}$ ,  $K_{1,3}$  are the spring constants; and  $L_{1,1}$ ,  $L_{1,2}$ ,  $L_{1,3}$  are the spring preloads.

For the relay valve, there are two variable areas, the supply  $A_{1,6}$  and the exhaust  $A_{1,4}$ , that depend on the displacement  $X_{1,1}$ . Note that  $A_{1,6} = 0$  when  $X_{1,1} < X_0$ , and  $A_{1,6} = \pi D_{1,6}(X_{1,1} - X_0)$  for  $X_0 < X_{1,1} < X_S$ . On the other hand,  $A_{1,4} = 0$  when  $X_{1,1} > -X_I$  and  $A_{1,4} = -\pi D_{1,4}(X_{1,1} + X_I)$

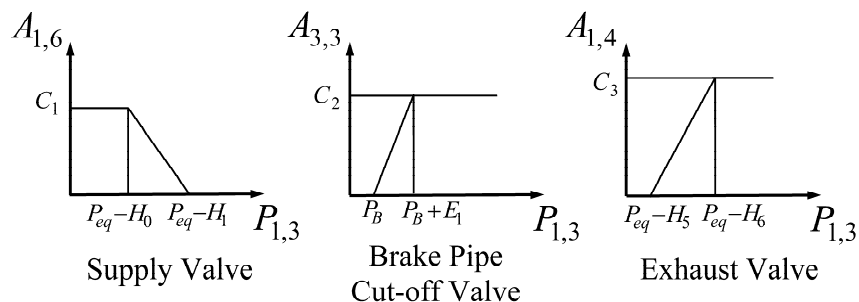
for  $-X_E < X_{1,1} < -X_I$ . Recall that the supply valve is open only when the displacement is greater than  $X_0$ , while the exhaust valve is open when it is less than  $-X_I$ .

### 3. Relay Valve States

The relay valve has different modes of operations defined mainly by the difference between the equalizing reservoir pressure  $P_{eq}$  and the intermediate chamber pressure  $P_{1,3}$ . The three possible modes of operation are the *supply state*, the *intermediate state*, and the *exhaust state*. Figure 80a shows the relationship between the relay valve states and the difference between the two pressures acting on the diaphragm surfaces, while Fig. 80b shows the configuration of the relay supply valve, the brake pipe cut-off valve and the relay exhaust valve as function of the value assumed by pressure  $P_{1,3}$ . By examining these figures, one can better understand the three modes of operation of the relay valve which are summarized in the remainder of this appendix.



(a) Relay valve states

(b) Supply, brake pipe cut-off, and exhaust valves configurations  
Figure 80. Valve states and configurations, Appendix

### 3.1. Supply State

The opening of the supply valve can be activated during any of the brake pipe modes (application, release/recharge, emergency). In order for the relay valve to maintain the pre-selected pressure value against the brake pipe leakage, the lapping position is considered as part

of the supply state, for any of the above mentioned modes. The values of the pressure  $P$  and the area  $A$  used in Eq. 4.57 are  $P = P_{mr}$ , and  $A = A_{1,6}$ . As previously mentioned,  $A_{1,6}$  is a function of the valve displacement  $X_{1,1}$ , which is again a function of the pressure  $P_{1,3}$ . As shown in the previous section,  $A_{1,6}$  can be determined using the following equation:

$$A_{1,6} = \pi D_{1,6} (X_{1,1} - X_0) \quad (8)$$

Note that  $X_{1,1}$  can be determined using Eq. 4.55. Also the brake pipe cut-off valve area  $A_{3,3}$  (depending on the valve displacement  $X_{3,1}$ ) is function of  $P_{1,3}$  (which is equal to  $P_{3,1}$ ). Equation 4.59 also leads to

$$A_{3,3} = \begin{cases} 0 \text{ (closed),} & P_{1,3} \leq P_B, X_{3,1} = 0 \\ \pi D_{3,3} A_{3,2} \frac{P_{3,1} - P_B}{K_{3,1}}, & P_B \leq P_{1,3} < P_B + \varepsilon, X_{3,1} = A_{3,2} \frac{P_{3,1} - P_B}{K_{3,1}} \\ \pi D_{3,3} X_B = C_2, & P_{1,3} \geq P_B + \varepsilon, X_{3,1} = X_B \end{cases} \quad (9)$$

Substituting the obtained values for  $P$  and  $A$ , Eq. 4.57 can in general be written in the following form:

$$f = \sum_{n=0}^4 \beta_n (P_{1,3})^n = 0 \quad (10)$$

This nonlinear equation can be solved iteratively using a Newton-Raphson algorithm to determine the pressure  $P_{1,3}$ . It is important to point out that  $f$  is not a well behaved function because of the nonlinearity of the coefficients  $\beta_0, \beta_1, \beta_2, \beta_3$ , and  $\beta_4$ ; these coefficients are nonlinear functions of  $P_{1,3}$  and  $P_{eq}$ , and have different values in different regions (Abdol-Hamid, 1986).

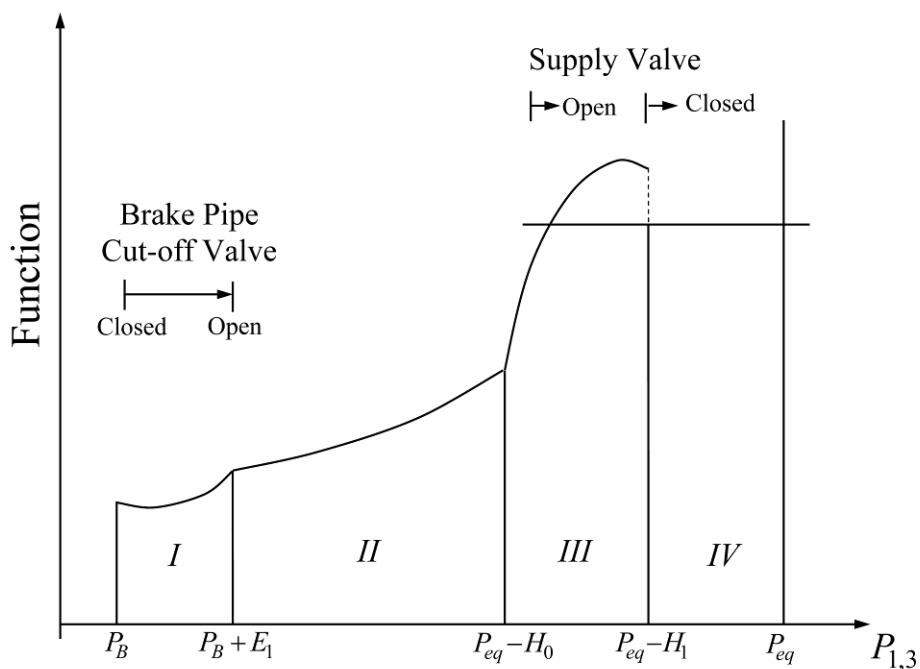


Figure 81. Supply state regions, Appendix

Figure 81 can be used to better understand the different regions and the problems associated with the nonlinearity of Eq. 10. By increasing the pressure  $P_{1,3}$ , first the supply valve fully opens, while the brake pipe cut-off starts opening. This defines Region I. When  $P_{1,3}$  reaches the threshold value, the cut-off valve is held fully open, defining Region II. In Region III,  $P_{1,3}$  is high enough to overcome all the other forces in the relay valve, and as a consequence, the supply valve starts closing. Region IV begins when the supply valve is completely closed. Before providing more details about these regions, the following variables are introduced:

$$\left. \begin{aligned} \alpha_1 &= -\pi D_{1,6} B_0, & \alpha_2 &= \pi D_{3,3} B_0 (P_{eq} - H_1), \\ \alpha_3 &= \pi D_{3,3} \frac{A_{3,2}}{K_{3,1}}, & \alpha_4 &= -\pi D_{3,3} \frac{A_{3,1}}{K_{3,1}} P_B \end{aligned} \right\} \quad (11)$$

For *Region I*, one has  $P_B \leq P_{1,3} < P_B + \varepsilon$  (the brake pipe cut-off valve moves), and  $H_0 \leq D_p$  (supply valve is fully open). The values of  $A$ ,  $A_{3,3}$  and  $\beta_i$  to be used in Eq. 10 are as follows:

$$\left. \begin{aligned} A &= A_{1,6} = C_1, & A_{3,3} &= \pi D_{3,3} A_{3,2} \frac{P_{3,1} - P_B}{K_{3,1}} = \alpha_3 P_{3,1} + \alpha_4, & \beta_0 &= -\alpha_4^2 P_{bp}^2 - C_1^2 P_{mr}^2, \\ \beta_1 &= -2\alpha_3 \alpha_4 P_{bp}, & \beta_2 &= C_1^2 + \alpha_4^2 - \alpha_3 P_{bp}^2, & \beta_3 &= 2\alpha_3 \alpha_4, & \beta_4 &= \alpha_3^2 \end{aligned} \right\} \quad (12)$$

For *Region II*, one has  $P_{1,3} \geq P_B + \varepsilon$  (brake pipe cut-off valve fully open), and  $H_0 \leq D_p$  (supply valve fully open). The values of  $A$ ,  $A_{3,3}$  and  $\beta_i$  to be used in Eq. 10 are as follows:

$$\left. \begin{aligned} A &= A_{1,6} = C_1, & A_{3,3} &= C_2 = \pi D_{3,3} X_B, \\ \beta_0 &= -C_1^2 P_{mr}^2 - C_2^2 P_{bp}^2, & \beta_2 &= C_1^2 + C_2^2, & \beta_1 &= \beta_3 = \beta_4 = 0 \end{aligned} \right\} \quad (13)$$

For *Region III*, one has,  $P_{1,3} \geq P_B + \varepsilon$  (brake pipe cut-off valve fully open), and  $H_1 < D_p < H_0$  (supply valve moves). The values of  $A$ ,  $A_{3,3}$  and  $\beta_i$  to be used in Eq. 10 are as follows:

$$\left. \begin{aligned} A = A_{1,6} &= \pi D_{1,6} B_0 (D_p - H_1) = \alpha_1 P_{1,3} + \alpha_2, & A_{3,3} &= C_2, \\ \beta_0 &= -\alpha_2^2 P_{mr}^2 - C_2^2 P_{bp}^2, & \beta_1 &= -2\alpha_1 \alpha_2 P_{mr}^2, & \beta_2 &= C_2^2 + \alpha_2^2 - \alpha_1^2 P_{mr}^2, \\ \beta_3 &= 2\alpha_1 \alpha_2, & \beta_4 &= \alpha_1^2 \end{aligned} \right\} \quad (14)$$

For *Region IV*,  $P_{1,3} \geq P_B + \varepsilon$  (brake pipe cut-off valve fully open), and  $D_p \leq H_1$  (supply valve closed). Furthermore, the exhaust valve is closed, and therefore, the function  $f$  is equal to zero.

*Region V*, represents another scenario, which is not shown in Fig. 81. In this region, the system may operate such that both the supply and the brake pipe cut-off valves are moving. This happens if  $P_B + \varepsilon$  is high, or if  $H_0$  is low; with values that depend on the valve construction, design and on the spring preloads. In this region,  $P_B \leq P_{1,3} < P_B + \varepsilon$ , and  $H_1 < D_p < H_0$ . The values of  $A$ ,  $A_{3,3}$  and  $\beta_i$  to be used in Eq. 10 are as follows:

$$\left. \begin{aligned} A = A_{1,6} &= \alpha_1 P_{1,3} + \alpha_2, & A_{3,3} &= \alpha_3 P_{3,1} + \alpha_4, & \beta_0 &= -\alpha_2^2 P_{mr}^2 - \alpha_4^2 P_{bp}^2, \\ \beta_1 &= -2\alpha_1 \alpha_2 P_{mr}^2 - 2\alpha_3 \alpha_4 P_{bp}^2, & \beta_2 &= \alpha_2^2 + \alpha_4^2 - \alpha_1^2 P_{mr}^2 - \alpha_3^2 P_{bp}^2, \\ \beta_3 &= 2\alpha_1 \alpha_2 + 2\alpha_3 \alpha_4, & \beta_4 &= \alpha_1^2 + \alpha_3^2 \end{aligned} \right\} \quad (15)$$

By using the appropriate parameters for each region, Eq. 10 can be solved numerically to determine the pressure  $P_{1,3}$ .

### 3.2. Intermediate State

This state can be activated during any of the brake pipe modes (application, release/recharge) and may include the lapping position provided that there is no leakage in the entire air brake system. During this state, both the supply and the exhaust valve are completely closed, that is,

$A_{1,6} = A_{1,4} = A = 0$ . It follows that  $P_{1,3} = P_{bp}$ .

### 3.3. Exhaust State

This state can only be activated during the brake application mode. As previously shown, the equivalent exhaust area is  $A_{EX} = A_{1,4}A_{1,5}/\sqrt{A_{1,4}^2 + A_{1,5}^2}$ , where  $A_{1,4}$  is a function of  $P_{1,3}$ . This functional relationship is clear from the following equation:

$$A_{1,4} = \begin{cases} 0 & \text{(closed)} & D_p \geq H_5, X_{1,1} \geq -X_I \\ -\pi D_{1,4} (X_{1,1} + X_I) & & H_6 < D_p < H_5, -X_E < X_{1,1} < -X_I \\ \pi D_{1,4} (X_E - X_I) = C_3 & & D_p \leq H_6, X_{1,1} = -X_E \end{cases} \quad (16)$$

During this state the brake pipe cut-off valve is always fully open. Due to the fact that  $A_{1,5}$  is very small as compared with the brake pipe cut-off area,  $P_{1,3}$  is very close to the value of  $P_{bp}$ ; instead of solving Eq. 4.57 iteratively using the values presented in the preceding equation, one may use the values from the previous time step to calculate  $P_{1,3}$ , that is,

$$P_{1,3}^j = \left( \sqrt{(P_{bp}^2 C_2^2 + P_a^2 A_{EX}^2)} / (C_2^2 + A_{EX}^2) \right)^{j-1},$$

where subscript  $j$  refers to the current time step, while subscript  $(j-1)$  refers to the previous time step.

## VITA

**NAME:** Ali Afshari

**EDUCATION:** Ph.D., Department of Mechanical & Industrial Engineering,  
University of Illinois at Chicago, Chicago IL, 2011  
M.Sc., Department of Mechanical Engineering,  
Sharif University of Technology, Iran, 2006  
B.Sc., Department of Mechanical Engineering,  
Iran University of Science and Technology, Iran, 2004

**TEACHING EXPERIENCE:** Teaching Assistant of Thermodynamics Course,  
University of Illinois at Chicago, Chicago IL, Fall 2007  
Teaching Assistant of Railroad Vehicle Dynamics Course,  
University of Illinois at Chicago, Chicago IL, Spring 2010

**PROFESSIONAL MEMBERSHIP:** American Society of Mechanical Engineers (ASME)

**REVIEWING:** ASME 2011 International Design Engineering Technical  
Conferences (IDETC) and Computers and Information in Engineering  
Conference (CIE), Washington DC, USA  
ASME 2009 International Design Engineering Technical  
Conferences (IDETC) and Computers and Information in Engineering  
Conference (CIE), San Diego CA, USA

**PAPERS & PUBLICATIONS:** Afshari, A., and Shabana, A.A., "Directions of the tangential creep forces in railroad vehicle dynamics", *Journal of Computational and Nonlinear Dynamics*, 2010, Vol. 5  
Afshari, A., and Shabana, A.A., "On the choice of the contact frame in railroad vehicle dynamics", Presented in *Proceedings of the ASME International Design Engineering Technical Conferences & Computers and Information in Engineering Conference IDETC/CIE 2009*, August 30th–September 2nd, San Diego USA

Afshari, A., and Meghdari, A., "New Jacobian matrix and equations of motion for a 6 d.o.f cable-driven robot", *International Journal of Advanced Robotic Systems*, 2008, Vol. 4, No. 1

Afshari, A., and Rajaai, S.M., "Finite element simulation investigating the role of the helmet in reducing head injuries", *International Journal of Simulation Modeling*, 2008, Vol. 7, No. 1

Afshari, A., and Meghdari, A., "New form of Jacobian matrix and equations of motion for a 6 d.o.f cable-driven parallel robot using constraint variables", Presented in *17th International DAAAM Symposium Intelligent Manufacturing & Automation; Focus on Mechatronics and Robotics*, 8-11th November 2006, Vienna, Austria

**AWARDS &  
HONORS:**

Selected by ASME IDETC/CIE 2009 Committee among four students presenting Top Papers in Student Competition

Awarded the Medal of International DAAAM Symposium for the Best Paper Presentation and selected as the Youngest Researcher among the researchers of DAAAM 17th symposium in 2006 in Vienna, Austria

Awarded by Iran University of Science and Technology as Top Student in 2003